**The Dissertation Committee for Lele Peng Certifies that this is the approved version of the following dissertation:**

# Rational Synthesis and Structural Engineering of Two-Dimensional Inorganic Nanosheets for Electrochemical Energy Storage

**Committee:**

Guihua Yu, Supervisor

Arumugam Manthiram

Charles Mullins

Gyeong Hwang

# Rational Synthesis and Structural Engineering of Two-Dimensional Inorganic Nanosheets for Electrochemical Energy Storage

**by**

**Lele Peng, B.S.**

**Dissertation**

Presented to the Faculty of the Graduate School of

The University of Texas at Austin

in Partial Fulfillment

of the Requirements

for the Degree of

**Doctor of Philosophy**

**The University of Texas at Austin**

**May 2017**

## Acknowledgements

I would like to express the sincerest appreciation to my supervisor Prof. Guihua Yu for his inspiring guidance and continuous support during my years at the University of Texas at Austin. Prof. Yu invited me to the electrochemical energy storage field and provided all kinds of suggestions to help me develop my own area of interest and philosophy. Prof. Yu also gave me numerous advice in adapting the life and study at Austin. Without his valuable guidance and advice, I could not have developed my research work successfully. I also want to express my gratitude to all my committee members, Prof. Manthiram, Prof. Mullins and Prof. Hwang. They all agreed to serve as my committee without hesitation and gave me useful feedback on my dissertation.

In addition, I am also very grateful to many people who have provided assistance in my PhD research. Dr. Yu Zhao, a former postdoc in our group and now a professor at Soochow University, taught me plenty of experimental skills in materials synthesis, materials characterizations, and electrochemical tests. I also learned graphic drawing skills from him, which make me confident in designing graphic works in my future research. I have so many wonderful colleagues in *Yu Research Group*, like Yue Zhu, Zhiwei Fang, Pan Xiong, Dahong Chen, Chunshuang Yan, Hongsen Li, Ye Shi, Yu Ding, Changkun Zhang, Yangen Zhou, Leyuan Zhang, Fei Zhao, Xingyi Zhou, Borui Liu, Umair Khakoo, Yaqun Wang. They are good friends and good collaborators. I want to thank them for their kind help in my PhD research at UT. I would also like to express my thanks to Dr. Jun Lu, Dr. Yifei Yuan, Dr. Lu Ma and Dr. Xiangyi Luo at Argonne National Lab. We have good collaborations on several significant projects. Hope we can have more wonderful collaboration in the near future. I want to thank Mr. Yujun (Terry) Xie at Yale University, who helped me conduct the FIB cutting of our 2D nanomaterials

and the HRTEM characterizations. Many thanks should be delivered to Dr. Wei Jiang, Dr. Sheng-Heng Chung, Dr. Xiang Li, Dr. Yutao Li, Dr. Bingkun Guo, Dr. Todd Davidson, and Dr. Meryl Stoller. They helped me significantly in material characterization and gave me a lot of advice. I also appreciate the kind help from some scientists in Texas Materials Institute, Dr. Hugo Celio, Dr. Karalee Jarvis, and Dr. Shouliang Zhang. Moreover, I would like to thank the financial support by the Welch Foundation Grant F-1861 and ACS Petroleum Research Fund (55884-DNI10).

Last but not least, I am deeply indebted to my family for providing boundless love and unconditional support. I owe them many thanks. I would like to thank them for their love and support.

# Rational Synthesis and Structural Engineering of Two-Dimensional Inorganic Nanosheets for Electrochemical Energy Storage

Lele Peng, PhD

The University of Texas at Austin, 2017

Supervisor: Guihua Yu

Lithium-ion batteries have dominated the portable electronics industry and solid-state electrochemical R&D for the past two decades due to the relatively high energy density. However, the limited lithium resources and their non-uniform distribution are becoming big concerns. Therefore, exploring high-performance, safe rechargeable batteries based on abundant resources is urgent. Sodium-ion batteries are of great interest as a potentially low-cost and safe alternative to the prevailing lithium-ion battery technology owing to the high abundance of sodium in earth crust, even distribution in nature and its favorable redox potential (only ~0.3 V above that of lithium). Figures of merit for future SIBs call for a breakthrough in energy (>200 Wh $kg^{-1}$) and power density (>2000 W $kg^{-1}$) as well as the cycle life (>4000 cycles) by designing new electrode structures, materials engineering and identifying new chemistries, to satisfy the requirements of many potential applications ranging from ubiquitous portable electronics to grid energy storage.

Two-dimensional (2D) inorganic nanosheets offer exciting opportunities for fundamental studies and many technological applications due to their unique and fascinating physical and chemical properties. Preparation of 2D materials via exfoliation/delamination from intrinsically layered materials has been greatly limited by

the categories of materials with such suitably layered host crystals. It is critically challenging to obtain 2D nanocrystals from the materials of non-layered structures. This dissertation focuses on the rational synthesis and structural engineering of 2D inorganic nanosheets for high-performance electrochemical energy storage. Several 2D energy materials, such as $MnO_2$, $LiFePO_4$, $VOPO_4$ nanosheets, for electrochemical energy storage are presented. The synthesis and characterizations of these 2D energy materials are discussed in details. Their electrochemical characteristics for $H^+$, $Li^+$ and $Na^+$ storage and the corresponding energy storage mechanisms are also investigated for each case.

2D energy materials have proven effective in constructing kinetically favorable ion channels, but the irreversible restacking of the individual 2D nanosheets during materials processing or device fabrication may lead to the decrease of active sites for ion storage and the sluggish ion transport. To address this issue, two possible strategies are developed in this dissertation to improve the ion transport in 2D nanomaterials. One possible strategy is to increase the interlayer spacing to facilitate ion transport by creating a lower energy barrier for ion transport through the interlayer space. A general interlayer-engineering strategy to improve the sodium-ion transport in $VOPO_4$ nanosheets via organic molecules intercalation is presented in Chapter 5. Another strategy is to make porous/holey materials to facilitate the ion transport. Chapter 6 summarizes the porosity engineering of 2D transition metal oxide nanosheets for improved rate capability and cycling stability for both lithium and sodium-ion storage.

Rational synthesis and structural engineering of 2D inorganic nanosheets has allowed us to make progress on (i) understanding the materials chemistry of 2D energy materials for electrochemical energy storage, (ii) developing promising strategies to address the key problems in 2D nanomaterials for energy-related applications, and (iii) fabricating high-performance lithium- and sodium-ion batteries for the next generation.

# Table of Contents

# List of Tables

# List of Figures

# Chapter 1: Introduction

Electrochemical energy storage (EES) devices, including alkali ion batteries and electrochemical capacitors (ECs), have recently gained growing attention due to the rapid development of electric vehicles and smart devices.[1, 2] Lithium-ion batteries (LIBs) are able to deliver high energy densities (~380 Wh $kg^{-1}$ for $LiCoO_2$-graphite cell), but not good in power densities; while ECs deliver high powder densities, but their inferior energy densities (10~14 Wh/kg) always cannot meet the increasing energy demands of the practical devices (**Figure 1.1**).[3] Among those EES devices, LIBs have dominated the portable electronics industry and solid-state electrochemical R&D for the past two decades due to the relatively high energy density. However, the limited lithium resources and their non-uniform distribution are becoming big concerns. [4, 5] Therefore, exploring high-performance, safe rechargeable batteries based on abundant resources is urgent.

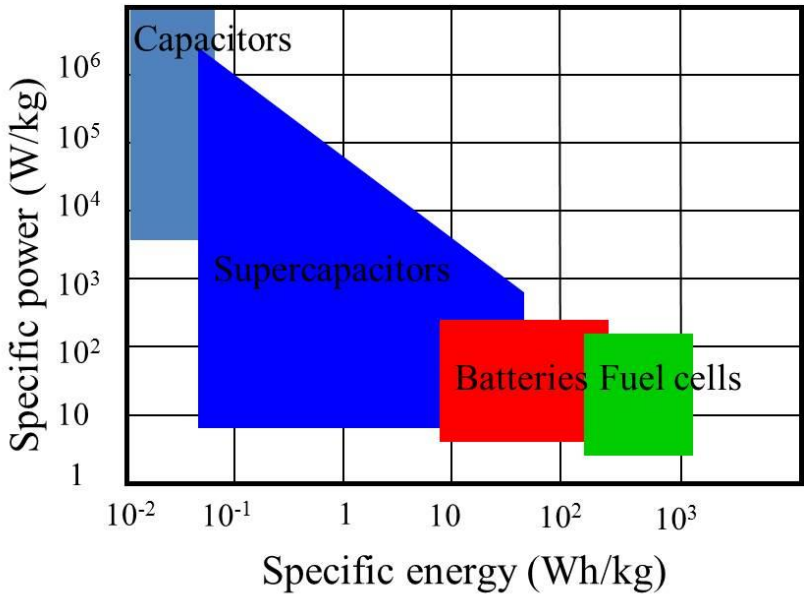


**Figure 1.1. Ragone plot of different energy storage devices.**

Sodium-ion batteries (SIBs) are of great interest as a potentially low-cost and safe alternative to the prevailing lithium-ion battery technology owing to the high abundance of sodium in earth crust, even distribution in nature and its favorable redox potential (only ~0.3 V above that of lithium).[6-8] LIBs and SIBs share identical working principles: during discharge and charge processes lithium or sodium-ions are shuttled through a liquid lithium or sodium-ion electrolyte between the electrodes. A typical working mechanism is illustrated in **Figure 1.2**. During discharge, ions are extracted from the negative electrode (anode), and inserted into the positive electrode (cathode), i.e., ions carry the current from the negative to the positive electrode through the liquid electrolyte and polymeric separator. The opposite process occurs during charging. From the thermodynamic point of view, during the discharge, the negative free energy of the redox couple drives the reaction to proceed forward (downhill on the energy diagram), and the released chemical energy is thus delivered to the device powered by the battery.[9]

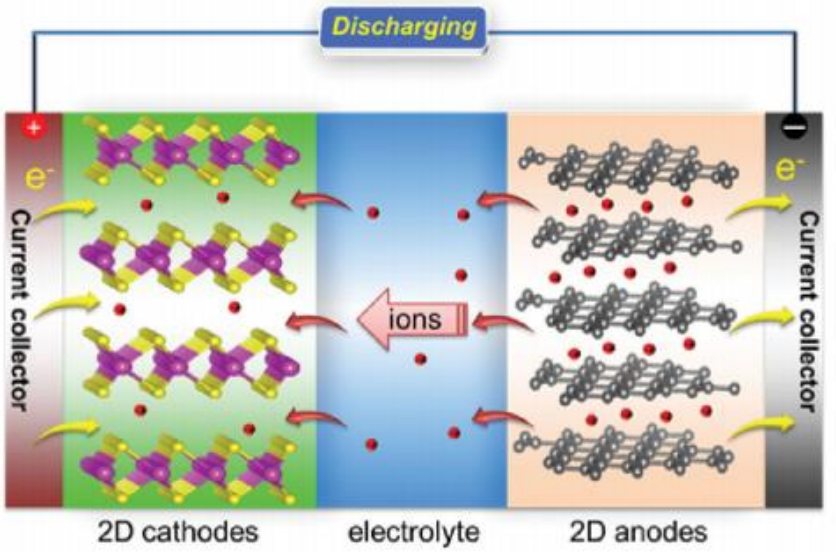


**Figure 1.2. Schematic of the mechanism of ion insertion into a lithium (sodium) ion battery.**

Recently, resounding success of graphene in energy storage technologies especially LIBs and ECs has sparked a flurry of research interest in exploring its analogues, including a huge diversity of 2D inorganic compounds such as graphene, transition metal oxides (TMO),[10] transition metal chalcogenides (TMD),[11] metal phosphates,[12] MXene,[13] *etc.* as promising electrode materials for electrochemical energy storage devices, including EC, LIBs and SIBs (**Figure 1.3**).[14] With successive thinning of the layers to approach nanoscale dimension, the inherent charge transport and storage property of 2D nanosheets can be very different from the bulk counterparts. Because of their high surface-to-volume ratio, a complete exposed lateral surface enables a full utilization of every available site for charge transport and storage. In addition, the charge transport process depends on the electrode interfaces, which can be elucidated in the following equation:[15]

$$\tau = \lambda^2 / D$$

where $\tau$, $\lambda$, and $D$ represent the diffusion time, charge diffusion length, and charge diffusion coefficient, respectively. According to the equation, the charge diffusion path to reach different depths of the bulk materials is significantly reduced after slicing the bulk materials into ultrathin 2D morphology, promoting a much faster electrochemical interaction at the active site. Beyond nanostructuring strategy, engineering of crystal orientation could be efficient to improve the ion transport in the electrode materials by carving a relatively low energy barrier facet for charge diffusion.[16] In these regards, tuning the crystal orientation and morphology of the material with unique 2D structures constitutes an interesting route to understand their transport and storage characteristics, and further fabricate the high-performance LIBs and SIBs.

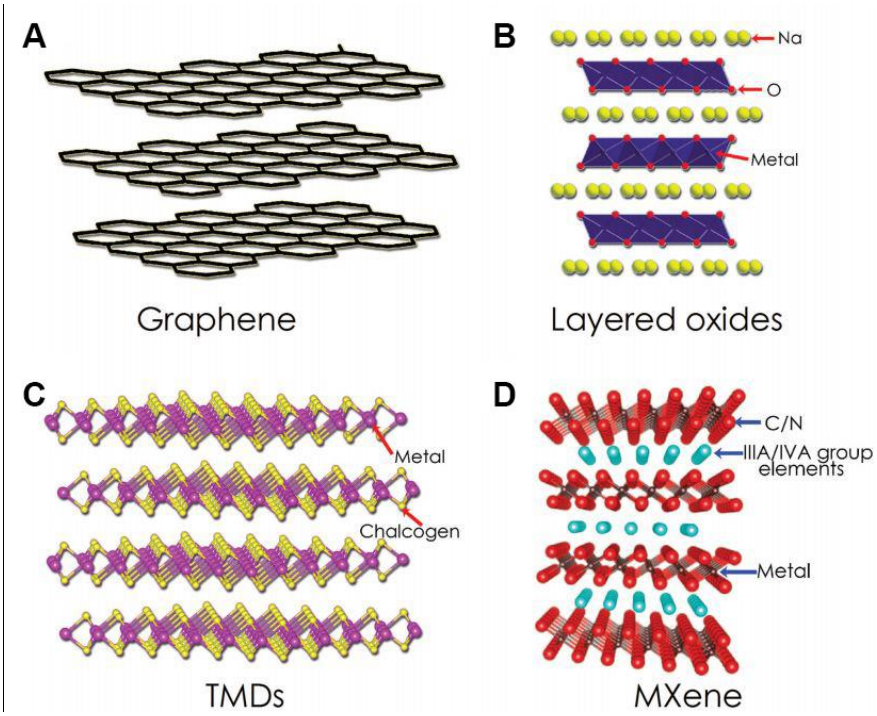


**Figure 1.3. Representative types of 2D nanomaterials for SIBs.** (A) graphene, (B) layered transition metal oxides (TMOs), (C) layered transition metal dichalcogenides (TMDs), and (D) 2D MXene nanosheets.

The facile and large-scale synthesis of 2D nanosheets is the critical step to the understanding of charge transport and storage properties. 2D nanosheets are typically produced by mechanically and chemically exfoliating the intrinsically layered structures, in which the interaction between layers of the parent layered structures has to be weakened before they can be further delaminated into single- or few-layered structure.[17, 18] Mechanically exfoliated 2D materials are excellent candidates for fundamental studies due to non-contaminated basal planes, but the low material yield limits the large-scale production. An alternative approach for the large-scale production of 2D nanomaterials is liquid-phase exfoliation. Some liquid-phase exfoliation methods rely on intercalation chemistry where foreign species (solvent molecules, chemically or electrochemically induced intercalants) are inserted into the van der Waals gap of each layer. The insertion

of guest species increases the interlayer spacing, weakens the adhesion between layers and facilitates the exfoliation into 2D nanosheets. To initiate the intercalation and exfoliation of 2D materials, sonication and centrifugation techniques are conventionally employed. Liquid-phase exfoliation can only occur effectively if the net energetic cost is very small, i.e. the enthalpy of mixing is minimized when the surface energies of flake and solvent match. It is critically challenging to synthesize 2D nanomaterials with well-defined morphology and composition from the materials of non-layered structures. Advances in nanotechnologies have made some progress on bottom-up wet chemistry methods to yield 2D nanomaterials. To date, research reports have revealed the possibility to grow 2D nanomaterials via surfactant-assisted self-assembly,[19] oriented attachment,[20] and topochemical conversion from a lamellar intermediate.[21] The Wulff construction theory is regarded as a useful guidance for these bottom-up synthesis of 2D nanomaterials. Energy minimization arguments are used to show that certain crystal planes are preferred over others, giving the crystal its shape, i.e. the preferred crystal facets of the final products will have the minimized surface Gibbs free energy (**Figure 1.4**).

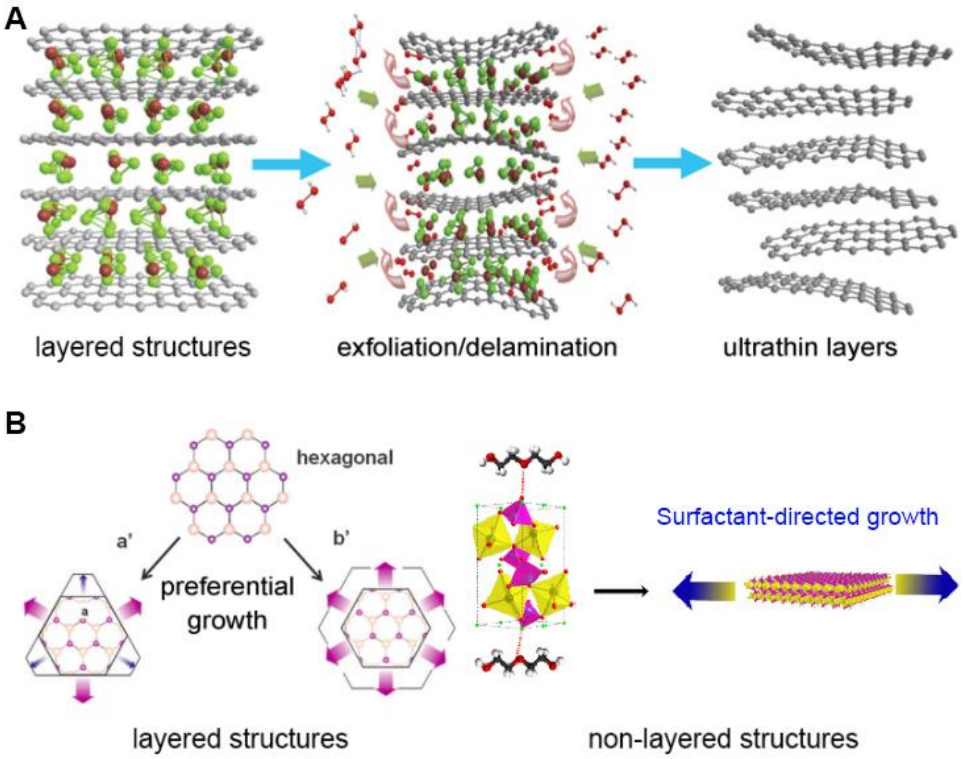


**Figure 1.4. Typical methods for 2D nanomaterials synthesis.** (A) top-down synthesis, (B) bottom-up synthesis.

Meanwhile, a general concern about 2D energy materials has been raised recently. While materials with 2D open framework have proven effective in constructing kinetically favorable ion channels, the irreversible restacking of the individual 2D nanosheets during materials processing or device fabrication may lead to the decrease of active surface sites for ion storage and the sluggish sodium-ion transport.[22-24] Many efforts have been devoted to alleviate the restacking problems of 2D nanosheets and to open up the unavailable surfaces. For instance, intercalation of various compounds, such as carbonaceous nanomaterials,[25] oxides[26] and polymers, into 2D nanosheets has been reported to open up the interlayer space for improved charge storage, although it involves complicated synthesis processes. Hierarchical structures via a solvothermal process or

surfactant-directed synthesis have been shown useful for energy storage,[27, 28] but they have inferior energy densities because of the relatively low tap densities of the resulting structures. Therefore, designing novel 2D nanostructures through structural engineering to minimize the restacking problem still remains a challenge for more efficient energy storage.

# Chapter 2: General experimental procedures

## 2.1 MATERIALS SYNTHESIS

The synthesis of 2D nanomaterials in this dissertation can be generally summarized in two methods: top-down and bottom-up methods. Top-down exfoliation process involves the exfoliation/delamination of the bulky layered structures in exotic liquid phases; while the bottom-up synthesis involves the confined growth of nanomaterials under specific surfactants or capping agents, such as surfactant-directing growth via hydro/solvothermal reaction. Top-down exfoliation can only be applied to process 2D nanomaterials with intrinsically layered structures. While bottom-up synthesis is suitable for the growth of both intrinsically layered structures and non-layered structures. For 2D nanomaterials with layered structures, their anisotropic growths are mainly attributed to the surface energy differences between the edges and planar facets. For the intrinsic non-layered structures, controlling the facet growth via surfactants would be a promising method to obtain 2D nanosheets.

The detailed synthesis and fabrication procedures of the 2D nanomaterials studied in this dissertation are described in the respective chapters.

## 2.2 MATERIALS CHARACTERIZATION

The general physical and chemical properties of the materials employed in the experiments were characterized by the following techniques. The specific characterization procedures will be described in the respective chapters.

### 2.2.1 Scanning electron microscopy (SEM)

Morphologies and microstructures of the as-prepared samples were characterized with a scanning electron microscope (SEM) (Hitachi s-5500) equipped with a scanning transmission electron microscope (STEM). Dried powders were directly used for SEM

characterizations. The STEM tests were conducted on a copper grid with deposition of 2D nanomaterial dispersion in ethanol.

### 2.2.2 Transmission electron microscopy (TEM)

Morphologies and microstructures of the as-prepared samples were characterized with a high-resolution transmission electron microscope (TEM) (2010F, JEOL).

### 2.2.3 Energy dispersive X-ray spectroscopy (EDS/EDX)

EDS/EDX is used to identify the elemental composition and the element distribution of the studied materials. Both SEMs and TEM described in sections 2.2.1 and 2.2.2 are equipped with energy dispersive X-ray spectrometers (EDS/EDX).

### 2.2.4 Raman spectroscopy

Raman spectroscopy of the 2D nanomaterials with different chemical states was conducted with a Raman microscope (Renishaw in Via Raman microscope) with a 532-nm laser and a 2400 lines $mm^{-1}$ grating stage at a 50X objective lens.

### 2.2.5 Fourier transform infrared spectroscopy (FTIR)

Fourier transform infrared (FTIR) spectroscopy data were obtained with KBr pellets with a PerkinElmer IR spectrometer.

## 2.3 ELECTROCHEMICAL CHARACTERIZATION

### 2.3.1 Electrode preparation

Electrodes were fabricated by coating the active material slurry onto the metal foil current collector, followed by evaporation of the N-methyl-2-pyrrolidone (NMP; Aldrich) solvent in the oven at 120 °C overnight. Al foil and Cu foil were used as current collectors for cathode and anode, respectively. The electrode slurry was made of active

materials mixed with superP carbon and polyvinylidene fluoride (PVDF), as carbon additive and binders respectively.

### 2.3.2 Cell assembly

The as-fabricated electrodes were assembled in the CR2032-type coin cells with separator (Celgard 2500), lithium anode (Aldrich), and stainless steel spacers and springs. All cells were assembled in an argon-filled glove box. The electrolyte used for lithium-ion batteries was prepared by dissolving 1.0 M $LiPF_6$ salt (Acros Organics) in a 1:1 volume ratio of ethylene carbonate (EC; BASF) and diethyl carbonate (DEC; BASF) or in a 1:1 volume ratio of ethylene carbonate (EC; BASF) and dimethyl carbonate (DMC; BASF). The electrolyte for sodium-ion batteries was 1 M $NaClO_4$ in propylene carbonate (PC) with 2% fluoroethylene carbonate (FEC).

### 2.3.3 Electrochemical impedance spectroscopy (EIS)

Electrochemical impedance spectroscopy (EIS) data were recorded by the Biologic VMP3 electrochemical test station with the impedance analyzer in the frequency range of 1 MHz to 10 mHz with an applied voltage of 5 mV.

### 2.3.4 Cyclic voltammograms (CV)

Cyclic voltammetry (CV) data were collected on Biologic VMP3 electrochemical test station between specific voltage ranges at an adjustable scan rate (mV $s^{-1}$).

### 2.3.5 Charge/discharge profiles and cyclability test

Charge/discharge profiles and cyclability data were collected with a programmable battery cycler (Arbin Instruments) and LAND electrochemical test station.

# Chapter 3: Top-down synthesis of ultrathin 2D nanosheets for electrochemical capacitors and alkali-ion batteries*

## 3.1 INTRODUCTION

As the rapid growth of portable consumer electronics, such as flexible displays, mobile phones and notebook computers, the development of flexible energy storage devices in all-solid-state has also been greatly promoted.[29-32] Flexible thin-film ECs in all-solid-state are regarded as promising flexible energy storage devices because they possess the synergic advantages of high performance, flexibility, thinness, and transparency.[33-36] Compared with electrical double-layer capacitors (EDLC), pseudocapacitors exhibit much higher energy density which is comparable to that of LIBs.[37-40] Pursuing 2D graphene-like materials with pseudocapacitive characteristics represents a promising direction to accomplish the flexible ultrathin-film pseudocapacitor in all-solid-state with higher energy density, and potentially excellent mechanical flexibility.[41, 42]

The key parameters for the promising 2D pseudocapacitive materials are not only the 2D ultrathin nature but also high specific capacitances and high redox potential that can lead to higher energy density ($E \sim CV^2$). However, the development of such 2D pseudocapacitive materials is still at its early stage, especially for flexible supercapacitors with high power and energy densities. For example, transition metal oxide nanosheets,

* L. Peng, X. Peng, B. Liu, C. Wu, Y. Xie, G. Yu, "Ultrathin Two-Dimensional $MnO_2$/Graphene Hybrid Nanostructures for High-Performance, Flexible Planar Supercapacitors" *Nano Lett.*, **2013**, *13*, 2151.
C. Wu, X. Lu, L. Peng, K. Xu, X. Peng, J. Huang, G. Yu, Y. Xie, "Two-Dimensional Vanadyl Phosphate Ultrathin Nanosheets for High Energy Density And Flexible Pseudocapacitors" *Nat. Commun.*, **2013**, *4*, 2431.
Y. Zhu,† L. Peng,† D. Chen, G. Yu, "Intercalation Pseudocapacitance in Ultrathin $VOPO_4$ Nanosheets: Toward High-Rate Alkali-Ion-Based Electrochemical Energy Storage" *Nano Lett.*, **2016**, *16*, 742.
H. Li,† L.Peng,† Y. Zhu, D. Chen, X. Zhang, G. Yu, "An Advanced High-Energy Sodium-ion Full Battery Based on Nanostructured $Na_2Ti_3O_7$/$VOPO_4$ Layered Materials" *Energy Environ. Sci.*, **2016**, *9*, 3399.
L. Peng co-carried out the experiments, co-analyzed the results, and co-wrote the paper. G. Yu supervised the project. All participated in the preparation of the project.

such as $Ni(OH)_2$ and $Co_3O_4$ nanosheets, delivers high capacitances for supercapacitor applications, while the reversible redox Faradaic reactions occurred on their surfaces only exhibit the potential windows of ~0.5 and 0.4 V, respectively,[43] both of which are still much lower than the limited electrochemical window of the aqueous solution (1.23 V).[44] Therefore, the discovery of new 2D graphene-like pseudocapacitive materials with enhanced electrochemical performance is much needed for constructing flexible thin-film based supercapacitors with higher power and energy densities, vital for satisfying the practical applications.

Vanadyl phosphate ($VOPO_4$) have long been recognized as promising cathode materials for electrochemical energy storage, such as pseudocapacitors, lithium-, and sodium-ion batteries, due to the rich redox reactions, high theoretical capacity, high redox reaction potential as well as unique structural features. $VOPO_4$ exhibits a flat voltage plateau at ~3.7 V vs $Li/Li^+$ and ~3.5 V vs $Na/Na^+$ for $V^{4+}/V^{5+}$ redox couple, respectively, and a large theoretical capacity of 166 mAh $g^{-1}$.[45,70] Due to the enhanced inionicity of (V–O) bonds when $(PO_4)^{3-}$ anion is introduced, $V^{4+}/V^{5+}$ redox couple of $VOPO_4$ possesses the higher potential than that for simple vanadium oxide.[46] Layered $VOPO_4$ has a high redox potential of ~1.0 V versus normal hydrogen electrode (NHE), and thus it is promising to establish the pseudocapacitors with improved energy density.[47, 48] Layered $VOPO_4$ can be feasible to be exfoliated into ultrathin $VOPO_4$ nanosheets while maintaining the integrity of the in-plane structure due to the presence of weak hydrogen bonds in $VOPO_4 \cdot 2H_2O$. With the synergic advantages of high redox potential and the layered structure, the exfoliated $VOPO_4$ ultrathin nanosheets could be a promising new 2D graphene-like material with greatly enhanced electrochemical properties. $MnO_2$ is considered one of the most promising pseudocapacitive materials for high-performance supercapacitors given its high theoretical specific capacitance, low cost, environmental

benignity, and natural abundance. $MnO_2$ materials have various phases which have shown promising applications in electrochemical energy storage, including supercapacitors and batteries. Among them, birnessite $\delta$-$MnO_2$ has a layered structure with small molecules and ions intercalated in the interlayer positions, such as $H_2O$, $Li^{+,}$ and $Na^+$. Layered $\delta$-$MnO_2$ structures can be easily exfoliated into nanosheets with thin thickness and good electrochemical activity, which represents a promising material platform to fabricate flexible supercapacitors with high power and energy density.

In this chapter, we report a facile liquid-phase exfoliation method to synthesize the ultrathin nanosheets, $MnO_2$ and $VOPO_4$ nanosheets demonstrated as examples, as electrodes for flexible pseudocapacitors with high performance and high flexibility. The ultrathin $VOPO_4$ nanosheets with an average thickness of ~4 nm and $MnO_2$ nanosheets with ~1 nm thickness can be obtained through ultrasonication in 2-propanol and distilled water, respectively. To fully explore the electrochemical performance of $VOPO_4$ nanosheets and $MnO_2$ nanosheets, graphene-based hybrid thin films were fabricated through a layer-by-layer assembly route to achieve high planar conductivity, high flexibility, and superior electrochemical performance. The flexible supercapacitors based on the $VOPO_4$/graphene and $MnO_2$/graphene hybrid thin films demonstrated large specific capacitances, high energy densities, and power densities as well as superior flexibilities. The greatly improved electrochemical performance can be attributed to the following features of the graphene-based hybrid thin films. Firstly, the planar structures based on the nanosheets integrated on graphene sheets can introduce more electrochemically active surfaces for absorption/desorption of the electrolyte ions and bring extra interface at the hybridized interlayer areas to facilitate charge transport during charging/discharging processes, offering good rate capability and cycling stability. Secondly, the integrated nanosheets serving as active centers for the pseudocapacitive

reactions contribute to the great enhancement of the specific capacitance. Thirdly, the nanosheets integrated on graphene can potentially tailor the distance between each sheet of densely stacked graphene and open up the interlayer space to allow for more electrolyte ions to penetrate efficiently into the hybrid thin film. The as-reported ultrathin 2D nanosheets represent a promising material platform to realize highly flexible energy storage devices as the power back-ups for stretchable/flexible electronic device.

## 3.2 EXPERIMENTAL DETAILS

### 3.2.1 Synthesis of the bulk layered compounds

Graphene was obtained from the chemical reduction of graphene oxides. Graphene oxide was synthesized in a modified Hummer's method.[49] In brief, 9:1 mixture of concentrated $H_2SO_4$/$H_3PO_4$ (360:40 mL) was added to a mixture of graphite flakes (3.0 g) and $KMnO_4$ (18.0 g), producing a slight exotherm to 35~40 °C. The reaction was then heated to 50 °C and stirred for 12 h. The reaction was cooled to room temperature and poured onto ice (400 mL) with 30% $H_2O_2$ (3 mL). The dispersion was centrifuged at the speed of 2000 rpm for 30 mins, and the supernatant was decanted away. The remaining solid material was then washed in succession with 200 mL of water, 200 mL of 30% HCl, and 200 mL of ethanol; after each wash, the mixture was centrifuged at the speed of 2000 rpm for 30 mins. When the successive washing was done, the precipitate was dried at 60 °C in a vacuum oven. Graphene was reduced using hydrazine in a reported method. Hydrazine monohydrate (1 μL for 3mg of GO, 98%, Aldrich) was subsequently added to the suspension. Additional stirring in an oil bath held at 80 °C for 12 h yielded a black precipitation of reduced graphene oxide powder. After cooling to room temperature, the powder was filtered through a fritted glass filter (medium pore size), followed by suction-

drying under house vacuum for 12 h. The resulting black material was dried under vacuum using a mechanical pump.

The bulk $MnO_2$ materials were synthesized in a reported method.[50] Typically, 20 mL of a mixed aqueous solution of 0.6 M tetramethylammonium hydroxide (TMA·OH) and 3 wt % $H_2O_2$ was added to 10 mL of 0.3 M $MnCl_2 \cdot 4H_2O$ aqueous solution within 15s. The solution became dark brown immediately as the mixed aqueous solution added, showing the evidence that $Mn^{2+}$ was oxidized to $Mn^{4+}$. This whole mixed aqueous solution was vigorously stirred overnight in the ambient atmosphere at room temperature. After this mild oxidation process, the precipitate was washed with water and methanol and centrifuged at a very low speed of 2000 rpm for 20 mins, after which the precipitate was dried in a vacuum oven at 60 °C.

Bulk $VOPO_4 \cdot 2H_2O$ was obtained according to a simple method reported in the previous literature.[51] The mixture, including $V_2O_5$ (4.8 g), $H_3PO_4$ (85% 26.6 ml) and $H_2O$ (115.4 ml), was refluxed at 110 °C for 16 h. Thereafter, the system was allowed to cool down to room temperature. The yellow precipitate was finally collected by filtration and washed several times with water and acetone. The resulting sample was dried in vacuum at 60 °C for 3 h.

### 3.2.2 Synthesis of ultrathin $MnO_2$ and $VOPO_4$ nanosheets

The layered structures could be exfoliated by solution and organic solvent. In our case, the layered H-type birnessite $MnO_2$ can be exfoliated by water solution. Experimentally, 10 mg bulk $\delta$-$MnO_2$ was added into 20 mL water for ultrasonic treatment. After ultrasonic treatment for 10h, the dispersion was centrifuged at the speed of 1000 rpm, removing the un-exfoliated residues from the dispersions. As is well-known, the hydrazine reduced graphene is not easily exfoliated by water. Thus in our

work, we adopted DMF to disperse graphene nanosheet. Similar to the process of exfoliating bulk $\delta$-$MnO_2$, 1 mg graphene was dispersed in 20 mL DMF solvent. After ultrasonic treatment for 10h, the dispersion was centrifuged at the speed of 1000 rpm, removing the un-exfoliated graphites from the dispersions.

Bulk $VOPO_4 \cdot 2H_2O$ (30 mg) was dispersed in a sealed glass bottle with 25 ml 2-propanol and then the dispersion was ultrasonicated in iced water for 15 min forming the $VOPO_4$ ultrathin nanosheets. The resultant yellow suspension was collected by vacuum filtration with a 0.22 μm pore size cellulose membrane, forming a homogeneous thin film, which can be easily transferred to arbitrary substrates by pressing another side of the cellulose membrane.

### 3.2.3 Assembly of the nanosheets/graphene hybrid thin film

The graphene used in our experiments was synthesized according to the procedure used in previous studies. The $VOPO_4$/graphene hybrid film was assembled by a layer-by-layer strategy. Specifically, the $VOPO_4$ and graphene dispersion were vacuum filtered in turns over a cellulose membrane with 0.22 μm pore size to form a homogeneous thin film. The thickness of the hybrid thin film can be tuned by changing the filtrated amount of the $VOPO_4$ and graphene dispersion.

### 3.2.4 Preparation of gel electrolyte

Four grams of PVA powder was put into 40 ml distilled water with stirring at 95 °C (ref. 35). When the PVA powder was completely dissolved, 8.5 g LiCl was added to the solution under vigorous stirring. After the LiCl/PVA turned to into a transparent and clear gel, it was cooled down to room temperature. At last, the LiCl gel electrolyte was prepared.

## 3.3 RESULTS AND DISCUSSION

### 3.3.1 Layer-by-layer design of thin film electrodes for high-performance supercapacitors

The electrode configuration in this chapter to fabricate the high-performance flexible supercapacitor is the planar structure obtained by the layer-by-layer assembly of pseudocapacitive 2D nanomaterials (such as $MnO_2$ and $VOPO_4$ nanosheets) with electrical conductive graphene nanosheets. Take the $MnO_2$ nanosheets as an example, **Figure 3.1** shows the design of hybrid 2D $\delta$-$MnO_2$/graphene structures based planar supercapacitors. The planar structures of $\delta$-$MnO_2$/graphene hybrid nanosheets can introduce more electrochemically active surfaces for absorption/desorption of the electrolyte ions and introduce extra interface at the hybridized interlayer areas to facilitate charge transport during charge/ discharge processes, offering good rate capability and cycling stability. In addition, the integrated $\delta$-$MnO_2$ nanosheets serving as active centers for the pseudocapacitive reactions contribute to the great enhancement of the specific capacitance. Meanwhile, the $\delta$-$MnO_2$ integrated on graphene can potentially tailor the distance between each sheet of densely stacked graphene and open up the interlayer space to allow for more electrolyte ions to penetrate efficiently into the hybridized film. Consequently, the hybrid 2D nanostructure design enhances the electrochemical performance of as-fabricated planar supercapacitors. Moreover, the pseudocapacitive $\delta$-$MnO_2$ nanosheet introduces high redox capacitance (theoretically $\sim$1300 F $g^{-1}$ for $MnO_2$) and greatly improves the electrochemical performance even at a relative low mass loading with an ultrathin layer.[52] Experimentally, the planar structure of the designed $\delta$-$MnO_2$/graphene hybrid is obtained by chemically integrating $\delta$-$MnO_2$ nanosheets on graphene due to the strong electrostatic interaction in the solution treatment process. The

charge behavior has evidenced that the water-exfoliated $\delta$-$MnO_2$ nanosheet is electronegative and DMF-exfoliated graphene is electropositive.

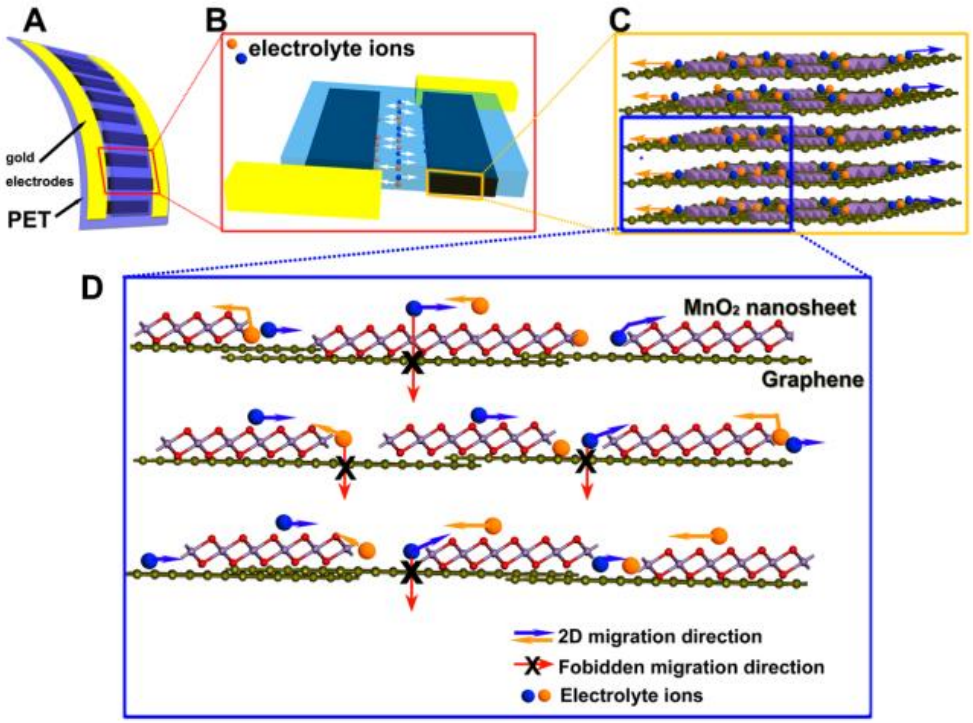


**Figure 3.1. Design of hybrid 2D $\delta$-$MnO_2$/graphene structures based planar supercapacitors.** (A) Schematic illustration of the ultraflexible planar supercapacitor. (B) The planar supercapacitor unit showing that the 2D hybrid thin film functions as two symmetric working electrodes. (C) The hybrid thin film was stacked by the layers of chemically integrated quasi-2D $\delta$-$MnO_2$ nanosheets and graphene sheets. (D) Schematic description of the 2D planar ion transport favored within the 2D $\delta$-$MnO_2$/graphene hybrid structures.

### 3.3.2 Synthesis and characterizations of ultrathin 2D $MnO_2$ and $VOPO_4$ nanosheets

The aforementioned planar structures show promising advantages in fabricating high-performance supercapacitors. The key step to fabricate the planar structures is to synthesize the ultrathin pseudocapacitive 2D nanosheet materials. This chapter covers the

top-down synthesis of ultrathin $MnO_2$ and $VOPO_4$ nanosheets for high-performance supercapacitor applications.

### *3.3.2.1 Structural features of ultrathin 2D $MnO_2$ nanosheets*

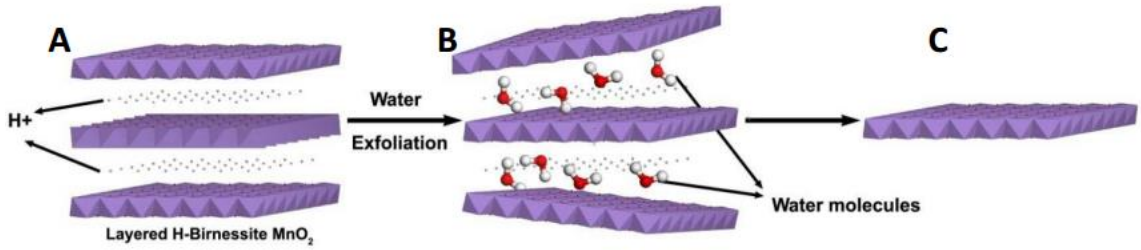


**Figure 3.2. Schematic illustration of top-down synthesis of $MnO_2$ ultrathin nanosheets.** (A) Layered bulk $\delta$-$MnO_2$ structure with $H^+$ intercalated between layers. (B) Water exfoliation of the layered bulk $MnO_2$. (C) the as-exfoliated single layered $MnO_2$ nanosheets.

In our case, graphene sheets were synthesized by reducing graphene oxides (GO) with hydrazine, which were prepared from purchased graphite powders with a grain size of 20μm according to a modified Hummers' method.[50] $\delta$-$MnO_2$ nanosheets were exfoliated from the bulk $\delta$-$MnO_2$ (**Figure 3.2**), which was obtained from the oxidation of $Mn^{2+}$ in a mild oxidative environment.[24] After an intercalation/extraction process of water molecules, the bulk $\delta$-$MnO_2$ was exfoliated into single layered $\delta$-$MnO_2$ nanosheets, forming a homogeneous dispersion with a typical Tyndall effect.[25] TEM and atomic force microscopy (AFM) images in **Figure 3.3** show the flat morphology of the $MnO_2$ nanosheets with an ultrathin atomic thickness of ~1.0 nm. Exfoliated graphene sheets shown in TEM and AFM images exhibit an average size of ~4 μm with a thickness of 0.9 nm. The graphene sheets with large area and flat morphology serve as ideal microscopic substrates to host the $\delta$-$MnO_2$ nanosheets to a maximum areal utilization. The synergic

effects of the electrostatic interaction and the flat morphology between the quasi-2D $\delta$-$MnO_2$ nanosheets and 2D graphene realized the integration of $\delta$-$MnO_2$ nanosheets onto graphene surfaces.

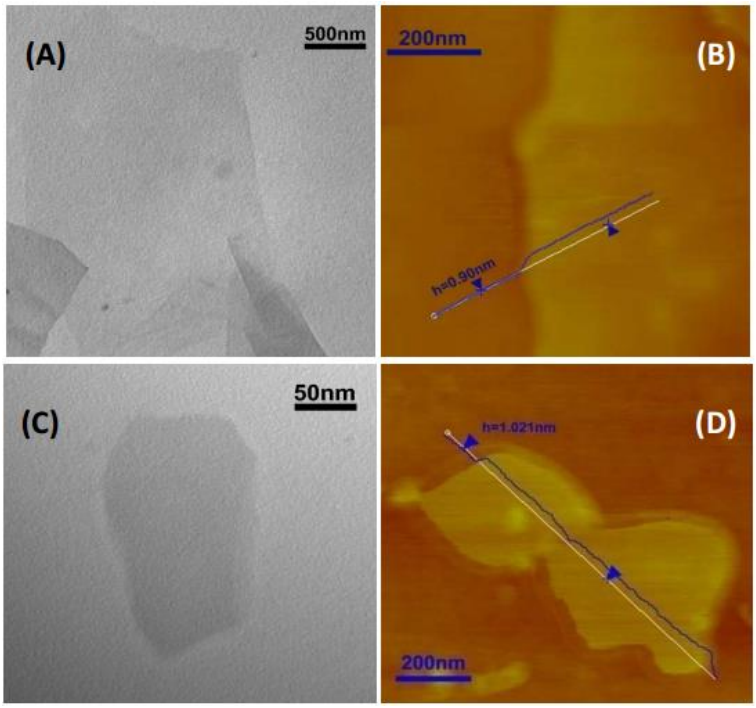


**Figure 3.3. TEM and AFM images of graphene and $\delta$-$MnO_2$ nanosheets.** (a) TEM image of graphene showing the size of ~4 μm. (b) Tapping mode AFM image of graphene nanosheet, indicating the thin thickness of ~0.9 nm. (c) TEM image of $\delta$-$MnO_2$ nanosheet. (d) Tapping mode AFM image of $\delta$-$MnO_2$ nanosheet, indicating the thin thickness of ~1.0 nm.

### *3.3.2.2 Structural features of 2D hybrid $MnO_2$/graphene thin films*

The structural features of 2D hybrid $MnO_2$/graphene nanosheets are summarized in **Figure 3.4.** Figure 3.4A shows the TEM image of the hybrid nanostructure, indicating that $\delta$-$MnO_2$ nanosheets were well-integrated on graphene sheets. Moreover, HR-TEM image and SA-ED pattern projected along *c* axis as shown in Figure 3.4B, in which the

interplanar spacing was measured to be 0.485 nm, further confirming the presence of high-quality $\delta$-$MnO_2$ integrated on the graphene surfaces. To make the best of the designed planar structures, it is critical to developing a reliable method to obtain the transferable ultrathin films with controlled thickness and orientation. Meanwhile, device fabrication of the oriented thin films relies on the structural design of material scaffolds. 2D graphene and quasi-2D graphene-like materials with the planar extensions provide a promising material platform to fabricate *c*-oriented thin films. In our case, the hybrid planar structures of $\delta$-$MnO_2$ integrated on graphene were used to fabricate the 2D hybrid film as the working electrodes via a conventional vacuum filtration process, similar to that previously reported for fabricating flexible graphene films.[26] The vacuum filtration method is adopted in our studies because self-limiting flow fields can produce films with controllable thickness and promote the assembly of hybrid nanostructures of quasi-2D $\delta$-$MnO_2$/graphene nanosheets in the *c*-orientation. Thin film X-ray diffraction (XRD) patterns were used to verify the *c* orientation of self-assembled 2D $\delta$-$MnO_2$/graphene hybrid thin films. As shown in Figure 3.4C, only the peaks of (002) and (006) facets can be detected, indicating a well-defined *c* orientation of the 2D $\delta$-$MnO_2$/graphene hybrid thin film. In Figure 3.4D, the SEM image of the surfaces of the hybrid thin film revealed the smooth and flat morphology of in-plane structure. The layered structure of the hybrid thin film could be clearly seen in the cross-sectional SEM image, with an average thickness of ~40 nm, indicating thin thickness of the hybrid thin film. The microscopic planar structure of hybrid materials provided the 2D transport pathway for the electrolyte ions and was further assembled into a macroscopic film, providing the material platform for planar supercapacitors.

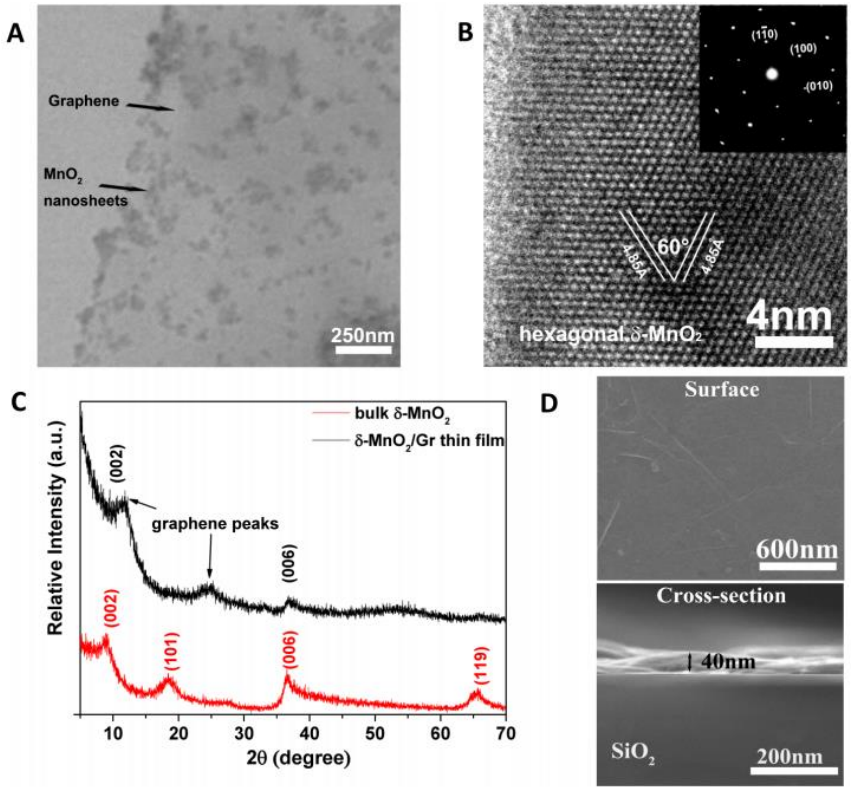


**Figure 3.4. Characterization of planar hybrid structures of $\delta$-$MnO_2$ nanosheets integrated on graphene.** (A) TEM image of the 2D hybrid structure with $\delta$-$MnO_2$ nanosheets integrated on graphene surfaces. (B) HRTEM image of a typical $\delta$-$MnO_2$ nanosheet exfoliated from the 2D $\delta$-$MnO_2$/graphene hybrid structures. Inset: SA-ED pattern of $\delta$-$MnO_2$ nanosheet showing the hexagonal symmetry. (C) XRD patterns of the bulk $\delta$-$MnO_2$ (red) and the assembled 2D $\delta$-$MnO_2$/graphene hybrid film (black). (D) SEM images showing the surface and cross-section of hybrid thin film, indicating the smooth surface with the average film thickness of ~40 nm.

### *3.3.2.3 Structural features of ultrathin $VOPO_4$ nanosheets*

The $VOPO_4$ ultrathin nanosheets were achieved by exfoliation of bulk $VOPO_4{\cdot}2H_2O$ through a simple ultrasonication method in 2-propanol with a short reaction time of 15 min (**Figure 3.5**A). For bulk $VOPO_4{\cdot}2H_2O$, $VOPO_4$ layers are linked together by hydrogen bonds from the interaction between $H_2O$ molecular and $VOPO_4$ layers. As one kind of weak intermolecular force, hydrogen bond is very sensitive to the

applied external force.[53] For example, the applied strong ultrasonication provides the powerful force to trigger the breaking of hydrogen bonds. In our case, the exfoliation process from bulk $VOPO_4 \cdot 2H_2O$ to $VOPO_4$ graphene-like material was conducted in 2-propanol solution, in that 2-propanol as a secondary alcohol is more suitable than primary alcohols as the dispersant due to the lower reactivity of hydroxyl group with the $VOPO_4$ layer matrix (**Figure 3.6**). The interaction force of hydrogen bonds between 2-propanol and $H_2O$ further promoted the $H_2O$ molecules extracted from the interlayer space of bulk $VOPO_4 \cdot 2H_2O$. The obtained $VOPO_4$ ultrathin nanosheets were homogeneously dispersed in solution with high stability for over several months.

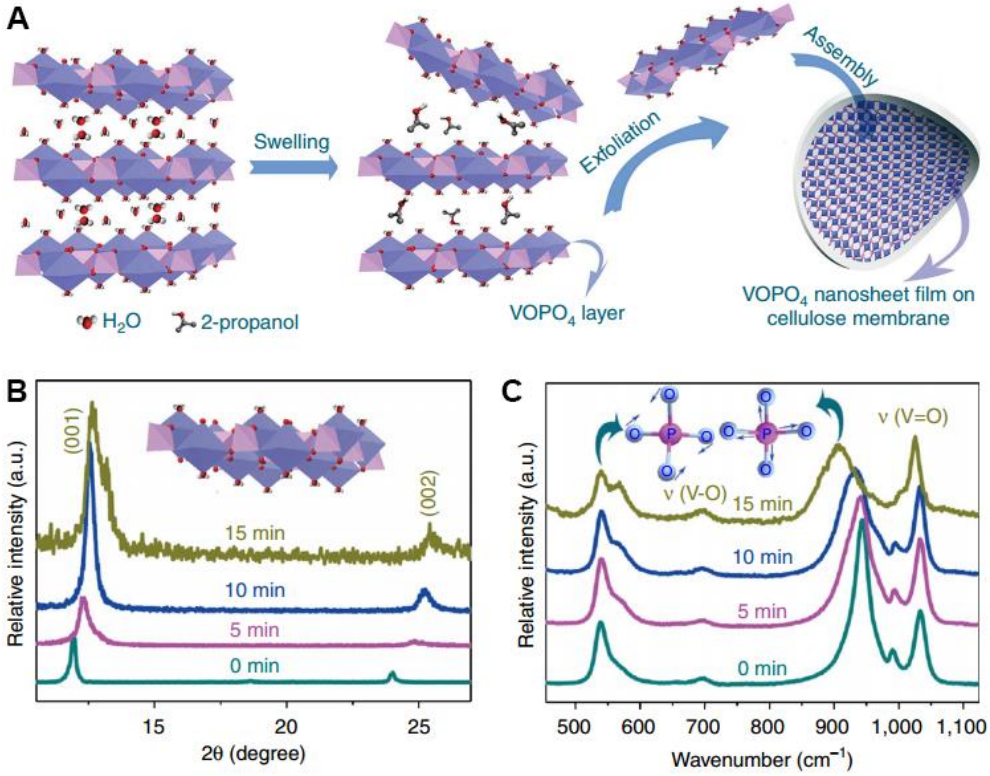


**Figure 3.5. Formation of $VOPO_4$ ultrathin nanosheets.** (A) Schematic illustration for 2-propanol-assisted exfoliation process from bulk $VOPO_4 \cdot 2H_2O$ to graphene-like $VOPO_4$ nanosheets. (B, C) XRD and Raman spectra of samples for the elongated ultrasonication time of 0, 5, 10 and 15 min, respectively. The insets in C are the symmetric bending (left) and stretching (right) modes of O–P–O, respectively.

The structural transformation process during the exfoliation could be revealed by the characterizations of X-ray powder diffraction (XRD) patterns and Raman spectra, which were performed on the transferrable $VOPO_4$ thin films. The XRD characterization of vacuum-filtration assembled films of samples at different sonication time is shown in Figure 3.5B. The XRD pattern at the initial sonication process can be readily indexed into the tetragonal $VOPO_4{\cdot}2H_2O$ with the standard JCPDS card No.84-0111 ($VOPO_4{\cdot}2H_2O$, space group P*4/nmm*, a=6.202 Å, b=6.202 Å, c=7.410 Å). As the strong ultrasonication proceeded, the (001) peak became relatively stronger compared with other XRD peaks, revealing that the applied sonication waves triggered the structural arrangements and enhanced the *c* axis orientation for the formation process of high-quality 2D nanosheets. Furthermore, the (001) peak of $VOPO_4{\cdot}2H_2O$ gradually shifted from lower 2θ (11.74 °) to a higher one (13.5 °) during the sonication process, indicating the decrease of the interlayer spacing distance from $VOPO_4{\cdot}2H_2O$ to the final $VOPO_4$ ultrathin nanosheets as a result of the escape of molecular $H_2O$ from $VOPO_4$ interlayers.

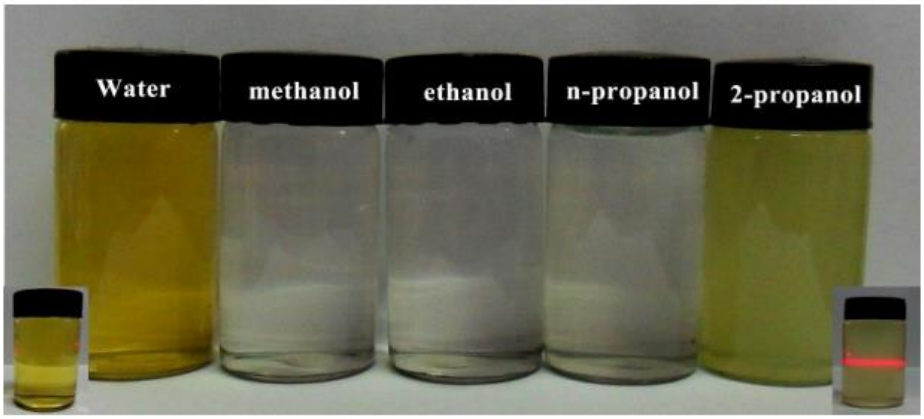


**Figure 3.6. Comparison of exfoliation efficiency in various dispersing solvents.** The synthetic $VOPO_4$ nanosheets were well dispersed in 2-propanol solution showing the Tyndall effect.

In addition, Raman spectra shown in Figure 3.5C further verified structural evolutions during the exfoliation process. The bands at 937 $cm^{-1}$ were assigned to the symmetric O–P–O stretching modes.[54, 55] With the elongated exfoliation time, the red shift of Raman peaks of O–P–O stretching mode was more noticeable. Obviously, there was a strong microstructural correlation between the symmetry of O–P–O stretching modes with the hydrogen bonding among the interlayered $H_2O$ molecular. With the breaking of hydrogen bonds from the oxygen atoms of the P–O bond in $VOPO_4$, the mitigation of the steric hindrance would facilitate the occurrence of the O–P–O stretching modes with lower energy. However, the peaks related to the symmetric bending vibrations of O–P–O, V–O and V═O stretching mode demonstrated little shift with no obvious peak position evolution (Figure 3.5C inset). The Raman results confirmed that the exfoliated $VOPO_4$ nanosheets maintained the integrity of the in-plane $VOPO_4$ structure without obvious structural deformations.

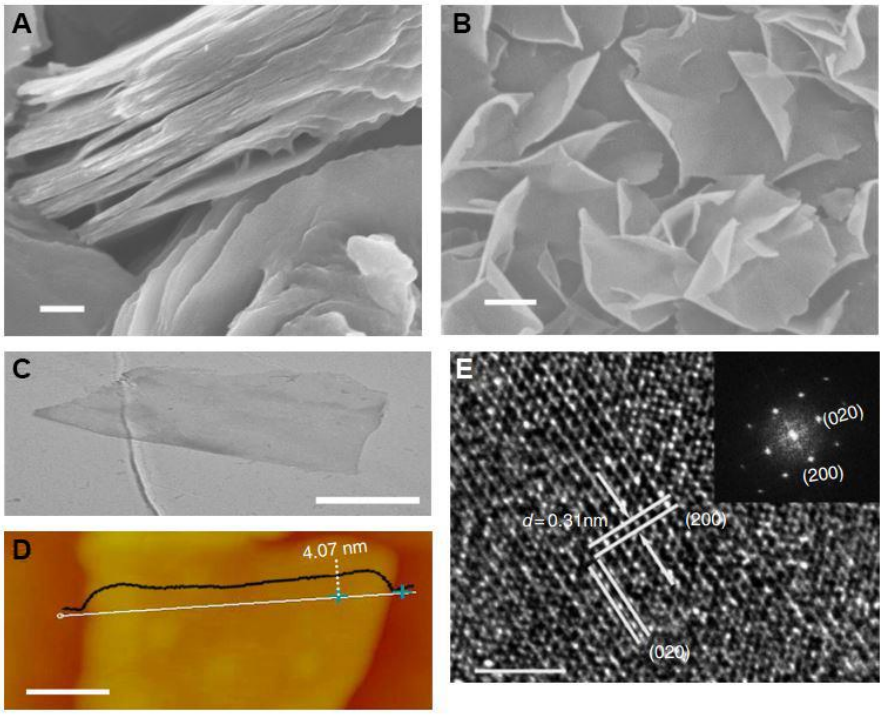


**Figure 3.7. Microstructural characterization of ultrathin $VOPO_4$ nanosheets.** (A) Field emission scanning electron microscopy image of bulk $VOPO_4{\cdot}2H_2O$ precursor. Scale bar, 200 nm. (B) The SEM image of exfoliated $VOPO_4$ ultrathin nanosheets with warped edges exhibiting the ultrathin features. Scale bar, 200 nm. (C) TEM image of a typical ultrathin nanosheet. Scale bar, 500 nm. (D) Atomic force microscopy image of a typical nanosheet with a thickness of 4.07 nm. Scale bar, 100 nm. (E) High-resolution TEM (HR-TEM) image of a typical nanosheet showing the lattice fringes of (200) and (020) planes, and the inset is the corresponding fast Fourier transform patterns of the same area in the HR-TEM image. Scale bar, 2 nm

To unravel the microscopic outlook and structural crystallinity of exfoliated 2D $VOPO_4$ nanosheets, microstructural characterizations were performed. Scanning electron microscopy (SEM) images of the precursor $VOPO_4{\cdot}2H_2O$ and graphene-like $VOPO_4$ nanosheets were taken and compared as shown in **Figure 3.7**. The bulk $VOPO_4{\cdot}2H_2O$ exhibited the typical layered structure, of which the layers were tightly stacked. In contrast, SEM image of the exfoliated products after 15 min ultrasonication (Figure 3.7B) shows the morphology of ultrathin nanosheets with a typical size ranging from 400 nm to

several micrometers. Transmission electron microscopy (TEM) image of the exfoliated $VOPO_4$ nanosheet in Figure 3.7C reveals a freestanding, sheet-like morphology with a lateral size of ~1 μm, and the nearly transparent feature implies the ultrathin thickness of exfoliated nanosheets. Atomic force microscopy image in Figure 3.7D was taken to further evaluate the thickness of the $VOPO_4$ nanosheet. The measured height was ~4.07 nm, denoting that the nanosheet was comprised of 5–6 single layers, given that the *c* parameter of the $VOPO_4 \cdot 2H_2O$ is 7.410 Å. The corresponding HR-TEM image and fast Fourier transform pattern are shown in Figure 3.7E, demonstrating that the exfoliated sheets were single crystalline with [001] preferential orientation. The interplanar distance of 0.31 nm fits well with the plane distance of $d_{200}$ and $d_{020}$, respectively. The orientation angle values 90 ° of these two planes of (200) and (020) in HR-TEM image and fast Fourier transform pattern was consistent with those calculated from tetragonal crystallographic parameters of $VOPO_4 \cdot 2H_2O$. These characterization results showed that $VOPO_4 \cdot 2H_2O$ was successfully exfoliated into ultrathin $VOPO_4$ nanosheets that exhibited good crystallinity and high *c* axis orientation, providing a strong basis for further assembly of $VOPO_4$ nanosheets into large-area practical energy storage devices. The thickness of the $VOPO_4$ nanosheets can be easily tuned by controlling the sonication time (**Figure 3.8**).

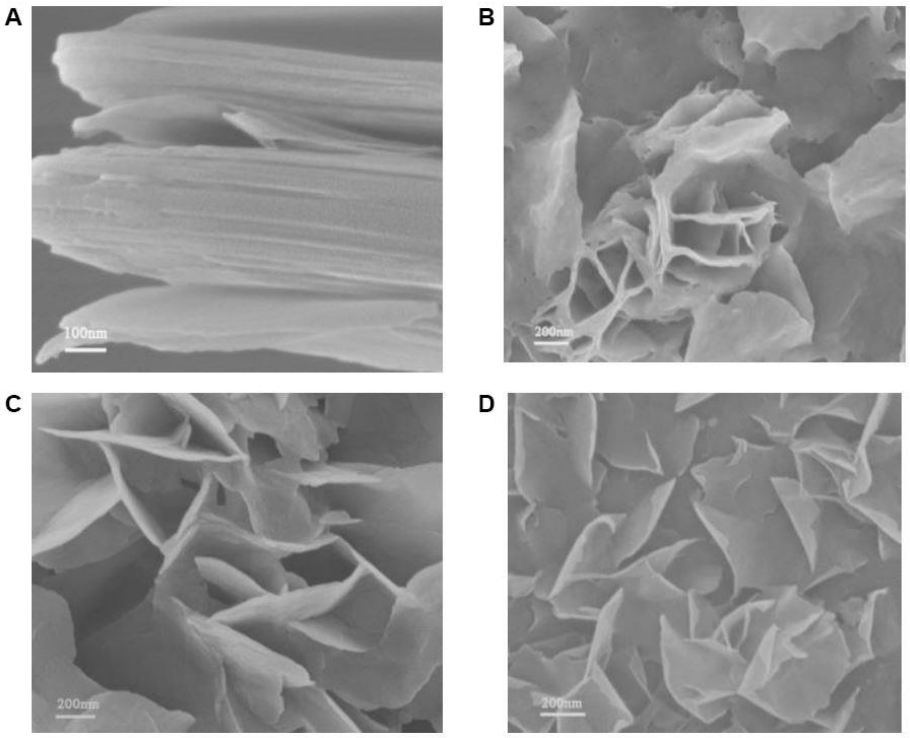


**Figure 3.8. Time-dependent morphology evolution during exfoliation.** (A) Bulk precursor $VOPO_4 \cdot 2H_2O$ was tightly stacked layer by layer. SEM images of $VOPO_4$ nanosheets obtained at different sonication time: (B) 5 min, (C) 10 min. (D) the graphene-like $VOPO_4$ nanosheets obtained at 15 min.

### *3.3.2.4 Structural features of 2D hybrid $VOPO_4$/graphene thin films*

The bulk $VOPO_4$ is well known as a high-performance electrochemical material with a high redox voltage in aqueous solution of 1.0 V versus NHE, approaching the electrochemical window of water (1.23 V), which entails the great fascination for the construction of high-efficiency energy storage devices. In our work, $VOPO_4$ ultrathin nanosheets with ~6 atomic layers, as a new inorganic graphene-like material, provide an ideal 2D material platform to investigate their electrochemical behavior, and to give the feasibility to construct the flexible pseudocapacitors. Because of the poor conductivity of $VOPO_4$ nanosheet, a layer-by-layer strategy was adopted to assemble the

$VOPO_4$/graphene hybrid film, and the hybrid thin film exhibits advantageous features of being uniform, compact and nearly transparent (**Figure 3.9**A). The hybrid film could be readily transferred and free-standing due to its high-quality film structure. Figure 3.9B is the cross-section SEM image of the hybrid film, showing the compact layer-by-layer structure with the thickness of ~90 nm thick. The inset in Figure 3.9B is the SEM image of the smooth hybrid film, where the graphene was underneath $VOPO_4$ layers as illustrated by the white arrows. The combined analyses of the TEM and XRD results further reveal that the as-formed $VOPO_4$/graphene hybrid film was the stacking of serial layers of chemically integrated $VOPO_4$ nanosheets on graphene sheets exhibiting the highly *c* axis crystalline orientation, in which the $VOPO_4$ nanosheets integrated on the graphene sheet as the building units and they assembled in stacks to form the final $VOPO_4$/graphene hybrid films (**Figure 3.10**). To better understand the layer-by-layer assembly of $VOPO_4$ nanosheets with graphene, Figure 3.9C shows the Raman spectra of the $VOPO_4$ film, graphene film, and $VOPO_4$/graphene hybrid film, respectively. The brown line is the Raman spectrum of graphene, which possesses two pronounced peaks at 1,580 $cm^{-1}$ (G) and 2,700 $cm^{-1}$ (2D) of graphene. The stronger intensity of G peak shows that the synthesized graphene is of good quality and high crystallinity and the weaker D peak at ~1,347 $cm^{-1}$ corresponds to the lower disordering.[56, 57] The red line represents the Raman spectrum of $VOPO_4$ nanosheets film with characteristic peaks of $VOPO_4$ at ~866 $cm^{-1}$ and 1,019 $cm^{-1}$ corresponding to the symmetric stretching vibration $\nu_1(PO_4)$ and V═O stretching mode. The Raman spectrum of $VOPO_4$/graphene hybrid film (blue line) in Figure 3.9C had the characteristic peaks of both $VOPO_4$ nanosheets and graphene with homogeneous distribution. The $VOPO_4$/graphene hybrid films were of high-quality with uniform, compact, free-standing and high transparency features.

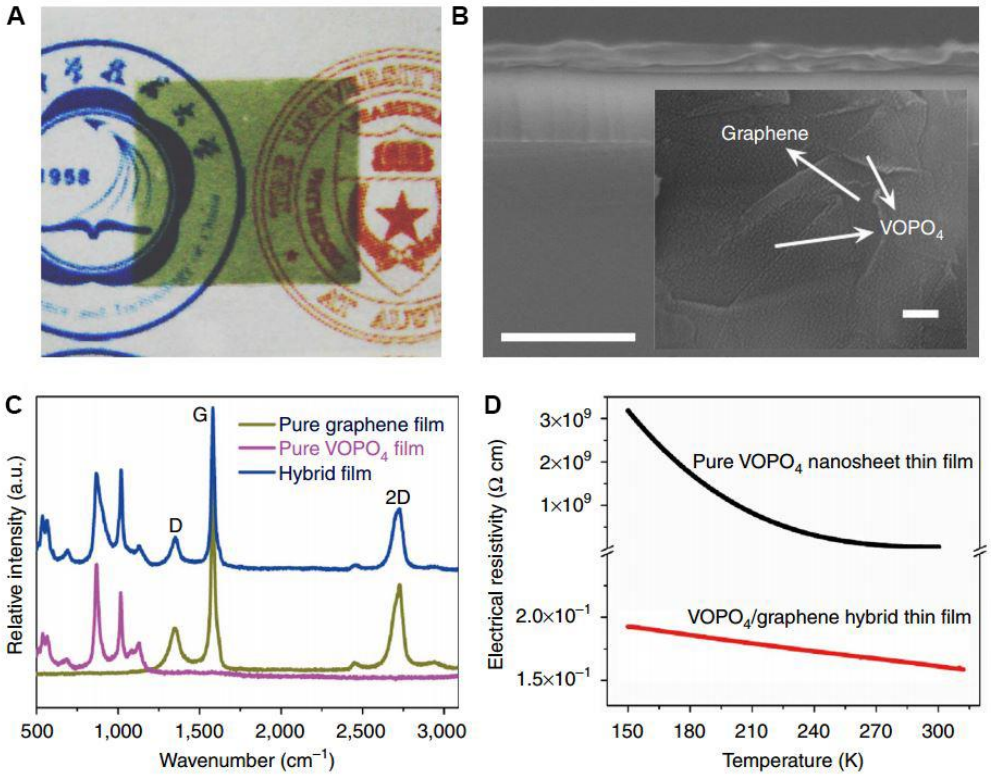


**Figure 3.9. Characterizations of the 2D $VOPO_4$/graphene hybrid thin film.** (A) Demonstration of $VOPO_4$/graphene hybrid thin film on the surface of PET substrate, exhibiting transparent feature. (B) The cross-section SEM image of the hybrid thin film with the thickness of ~90 nm. The surface of the hybrid film, of which the graphene lies under the $VOPO_4$ layers as indicated by the white arrows, is shown in the inset. Scale bar, 500 nm; Inset scale bar, 100 nm. (C) The Raman spectra of graphene film (brown line), $VOPO_4$ film (red line) and $VOPO_4$/graphene hybrid film (blue line), respectively. (D) The temperature dependence of planar resistivity of the $VOPO_4$/graphene hybrid film and pure $VOPO_4$ nanosheet thin film, where the incorporation of graphene greatly enhanced the electrical conductivity in the $VOPO_4$/graphene hybrid film.

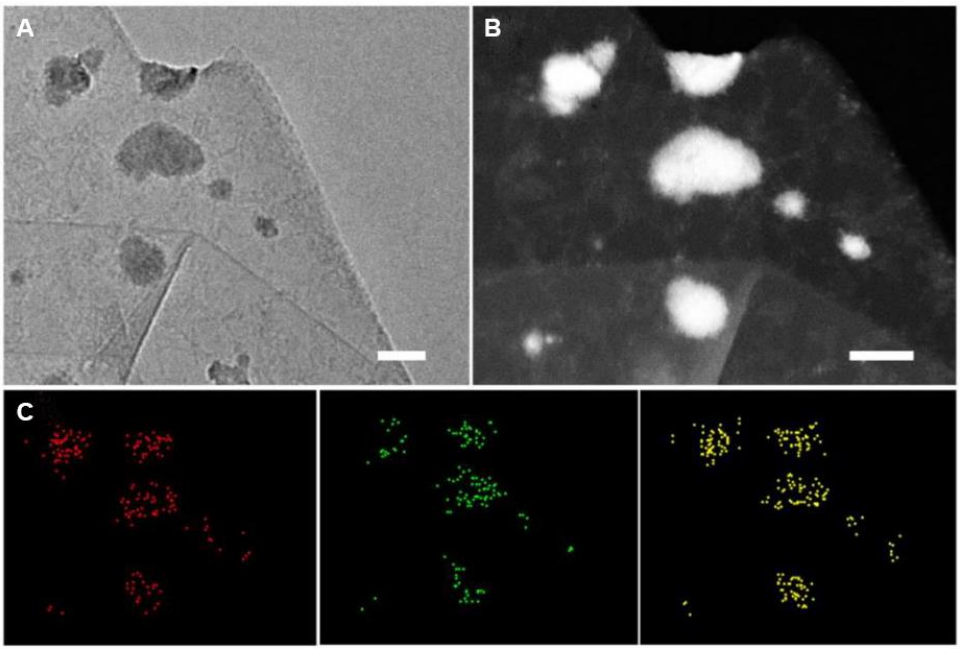


**Figure 3.10. $VOPO_4$ graphene-like material on graphene sheet.** (A) TEM image of the $VOPO_4$/graphene hybrid structure, scale bar, 80 nm. The typical HAADF-STEM (B) and elemental mapping images (C) of exfoliated $VOPO_4$ ultrathin nanosheet integrated on graphene, where the elements of V (red color), P (green color) and O (yellow color) were homogeneously distributed in the entire $VOPO_4$ nanosheet.

In addition, hybrid $VOPO_4$/graphene films exhibited greatly enhanced electrical properties. The hybrid film can be transferred onto various target substrates for electrical measurements. Temperature dependence of planar electrical resistivity of the $VOPO_4$/graphene hybrid film was carried out as shown in Figure 3.9D. As can be seen, the hybrid film possessed good conductivity in a wide temperature range from 150 to 300 K with slight resistivity change from $1.9 \times 10^{-1}$ Ω·cm (150 K) to $1.6\times 10^{-1}$ Ω·cm (300 K), which is eight orders of magnitude lower than that of pure $VOPO_4$ nanosheet thin film ($3.0 \times 10^{7}$ Ω·cm at 300 K). With the $VOPO_4$ nanosheets integrated on the graphene layers, the 2D $VOPO_4$/graphene hybrid film possessed the much improved electrical conductivity, making possible embodiment of outstanding electrochemical performance of $VOPO_4$ nanosheets.

### 3.3.3 Fabrication of thin-film based flexible supercapacitors

Assembly and transfer of ultrathin 2D nanosheet based materials onto large-area substrates are the essential processes for fabricating planar devices, especially for planar supercapacitors which require the integration of the whole device components into a two-dimensional configuration on the same horizontal plane. Briefly, a rectangle strip of the 2D $\delta$-$MnO_2$/graphene hybrid thin film obtained by vacuum filtration was rolled with a glass rod onto the flexible PET substrate, followed by tightly pressing and peeling off the cellulose acetate membrane. This procedure led to the transfer of the freestanding 2D hybrid thin film on the target substrate, as shown in **Figure 3.11**. Notably, hybrid 2D $\delta$-$MnO_2$/graphene thin films can be transferred onto a range of substrates such as PET, quartz, glass, and silicon wafer. By scraping along the dashed line as shown in Figure 3.11C and D, slim strips of the transferred thin film were obtained as the working electrodes for the planar supercapacitor. After repeated scrapings for the construction of an array of parallel lines as primary units of the working electrodes, two columns of gold current collectors were thermally evaporated on each side of the working electrodes and integrated the primary units into a typical planar supercapacitor device. The all-solid-state planar supercapacitor was finally established after filling the channel between two working electrodes with gel electrolyte of PVA/$H_3PO_4$, as demonstrated in Figure 3.11F.

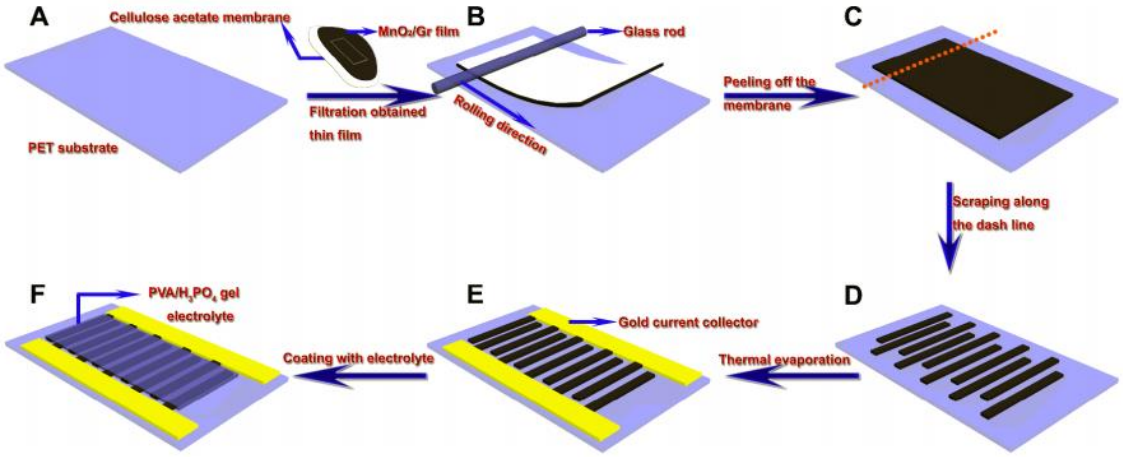


**Figure 3.11**. **Schematic of fabrication procedures for ultraflexible planar supercapacitors.** (A−C) Transferring 2D $\delta$-$MnO_2$/graphene hybrid thin film onto plastic PET substrates. (D) Obtaining strips of the hybrid thin film by scraping along the dashed line as the working electrodes. (E) Two columns of gold current collectors were thermally evaporated on each side of the working electrodes. (F) The planar supercapacitor was finally established after coating PVA/$H_3PO_4$ gel electrolyte on the parallel region filling the channel between two working electrodes.

### 3.3.4 Electrochemical performance

The planar hybrid nanostructure of quasi-2D $\delta$-$MnO_2$/graphene nanosheets is a key factor to enhance the electrochemical performance of in-plane supercapacitors. To evaluate the electrochemical performance of the planar supercapacitor based on the 2D $\delta$-$MnO_2$/graphene hybrid film, we performed cyclic voltammetry (CV), galvanostatic charge−discharge (CD) and flexibility tests using a two-electrode system.

#### *3.3.4.1 Electrochemical performance of the planar supercapacitors based on 2D δ-$MnO_2$/graphene hybrid thin film*

The as-fabricated planar supercapacitors based on 2D $\delta$-$MnO_2$/graphene hybrid structures have brought significant electrochemical performance enhancement, as clearly shown in **Figure 3.12**. A set of rate dependent CV curves of the planar supercapacitor based on 2D $\delta$-$MnO_2$/graphene hybrid (Figure 3.12A) and planar supercapacitor based on

graphene only (Figure 3.12B) were acquired at various scan rates from 50 to 400 mV $s^{-1}$ within−0.7 to 0.7 V voltage window. The nearly rectangular CV curves at different scan rates indicated the efficient intralayer charge transfer and the nearly ideal capacitive behaviors.[58] Note that no apparent redox peaks were observed at the voltage range of −0.7 to 0.7 V, which revealed that electrode materials based on $MnO_2$ nanosheets can be stabilized by PVA/$H_3PO_4$ gel electrolyte. At the same scan rates, Figure 3.12A and B showed that the resulting rectangle areas from CVs of planar supercapacitor based on $\delta$-$MnO_2$/graphene hybrids were substantially larger than those for planar supercapacitor based on graphene, suggesting that specific capacitance values of hybrid $MnO_2$/graphene planar supercapacitor were much higher than those for graphene-only based devices. Although high theoretical pseudocapacitance of transition metal oxides can significantly increase the capacitance of supercapacitor devices compared to electric double layer capacitors, in many of previously reported works,[59-61] the high values were obtained at relatively low scan rates (1−10 mV $s^{-1}$), making these supercapacitor devices lose advantages for being primary energy storage devices with high rate capability. In contrast, a high specific capacitance of ~200 F $g^{-1}$ was achieved in our studies under a high scan rate of 400 mV $s^{-1}$. Moreover, the enhanced electrochemical performance was confirmed by galvanostatic charge−discharge measurements performed under different current densities (from 0.5 to 10 A $g^{-1}$).

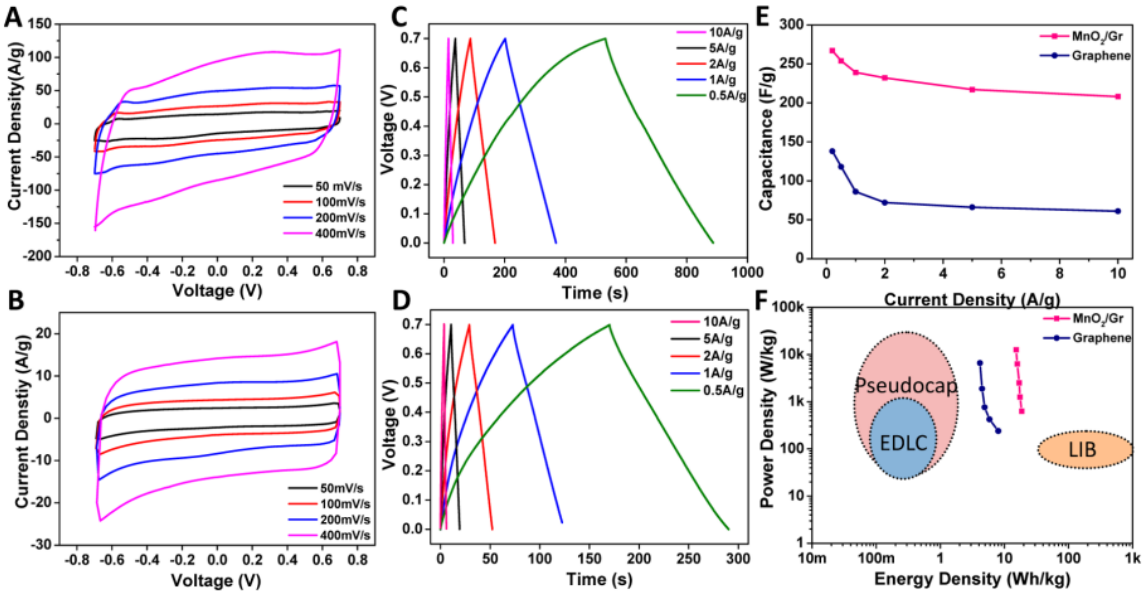


**Figure 3.12. Electrochemical performance of the planar supercapacitors based on 2D $\delta$-$MnO_2$/graphene hybrid thin film.** (A) CV curves for planar supercapacitors based on the 2D $\delta$-$MnO_2$/graphene hybrid at different scan rates (from 50 to 400 mV $s^{-1}$). (B) CV curves for planar supercapacitors based on graphene. (C) Galvanostatic charge−discharge curves of the planar supercapacitor based on the hybrid at various current densities (0.5 to 10 A $g^{-1}$). (D) Galvanostatic curves of the supercapacitor based on graphene-only. (E) Comparison of specific capacitance values for the supercapacitors based on hybrids and based on graphene. (F) A typical Ragone plot of as-fabricated supercapacitors.

Figure 3.12C and D showed that, at the same current density of 1 A $g^{-1}$, the charge−discharge time for $\delta$-$MnO_2$/graphene hybrid system was substantially prolonged (>100% increase) over graphene-only system, and the linear voltage−time profile and highly symmetric charge/discharge characteristics were indicative of good capacitive behavior achieved by hybrid electrode systems. The specific capacitance can be derived from the CD curves based on the following equation.[62]

$$C = I\frac{\Delta t}{m\Delta V}$$

in which $I$ is the constant current applied to the planar supercapacitor; $\Delta t$ and $\Delta V$ represent the discharge time and discharge voltage range respectively, and $m$ is the mass

loading of the electrodes. Accordingly, the as-fabricated in-plane supercapacitor based on the hybrid planar nanostructure yielded specific capacitances of 254, 249, 232, 217, and 208 F $g^{-1}$ at current densities of 0.5, 1, 2, 5, and 10 A $g^{-1}$, respectively, as summarized in Figure 3.12E. Meanwhile, the planar supercapacitor based on $\delta$-$MnO_2$/graphene hybrid exhibited better rate capability, with only ~22% capacitance loss when current density increases by a factor of 20 (from 0.5 to 10 A $g^{-1}$) compared to ~56% loss for graphene-based electrodes. The enhanced capacitance and rate capability can be attributed to the rational design of 2D $\delta$-$MnO_2$/graphene hybrid structures, which synergize the effects of both efficient 2D ion transport possible in the same horizontal plane and additional interfaces and pseudocapacitance brought by $\delta$-$MnO_2$ nanosheets.

To further evaluate the energy efficiency of as-fabricated planar supercapacitors based on the planar hybrid nanostructures of $MnO_2$/graphene, energy density (E) and power densities (P) were calculated from CD curves. Figure 3.12F showed the Ragone plot of the as-obtained planar supercapacitor based on $\delta$-$MnO_2$/graphene hybrid and compares specific E and P with those for pseudocapacitors, electrical double-layer capacitors (EDLC), and LIBs. As shown in the Ragone plot, the $MnO_2$/graphene hybrid based planar supercapacitors delivered a high energy density of 17 Wh $kg^{-1}$ at a power density of 2520 W $kg^{-1}$, superior to graphene-based planar supercapacitors. Moreover, the maximum energy density of 18.64 Wh $kg^{-1}$ and the highest power density of 12.6 kW $kg^{-1}$ were achieved for the hybrid $\delta$-$MnO_2$/graphene based planar supercapacitor, which are comparable to other previously reported carbon nanomaterials/$MnO_2$ based traditional supercapacitors, revealing that as-established planar supercapacitors would be a promising candidate to serve as high-energy power supply components in planar flexible electronics.

### *3.3.4.2 Cycling performance and flexibility demonstration of ultraflexible planar supercapacitors based on 2D δ-$MnO_2$/graphenehybrid thin film*

Good cycling stability is another critically important characteristic for planar supercapacitors based on hybrid nanostructures of 2D $\delta$-$MnO_2$/graphene. Owing to the good compressibility and mechanical extensibility possible with the planar ultrathin films, our planar supercapacitors achieved excellent cycling performance with impressive flexibility. CV and CD measurements were performed to illustrate these promising device characteristics. **Figure 3.13**A demonstrated that the as-fabricated planar supercapacitors based on 2D $\delta$-$MnO_2$/graphene hybrid film showed an excellent cycle life. After over 7000 times of charging/discharging cycles, the capacitance retention rates remained over 92%, and the Coulombic efficiency was still kept at~91%, indicating remarkable cycling stability of our planar supercapacitors. Taking advantage of PVA/$H_3PO_4$ gel as the electrolyte,[63] the planar structure can be stabilized to realize better capacitance retention and cyclability. CV curves of the planar supercapacitor under different bending states were measured at the scan rate of 100 mV $s^{-1}$ to explore the feasibility to fabricate an ultraflexible planar supercapacitor (Figure 3.15B). Indeed, there only existed slight differences in specific capacitances of the planar supercapacitor based on $\delta$-$MnO_2$/graphene hybrid when tested under three bending states (Figure 3.15C). Note that this hybridized thin film had no noticeable structural destruction even after being folded or rolled thousands of times, which cannot be realized using conventional three-dimensional building blocks (Figure 3.15D, E, and F). The demonstrated ultrahigh flexibility for hybrid 2D $\delta$-$MnO_2$/graphene nanosheets based planar supercapacitors can potentially be a significant feature of the next-generation flexible energy storage devices such as supercapacitors, lithium-ion batteries, and fuel cells, establishing a novel and important model to fabricate highly flexible power devices.

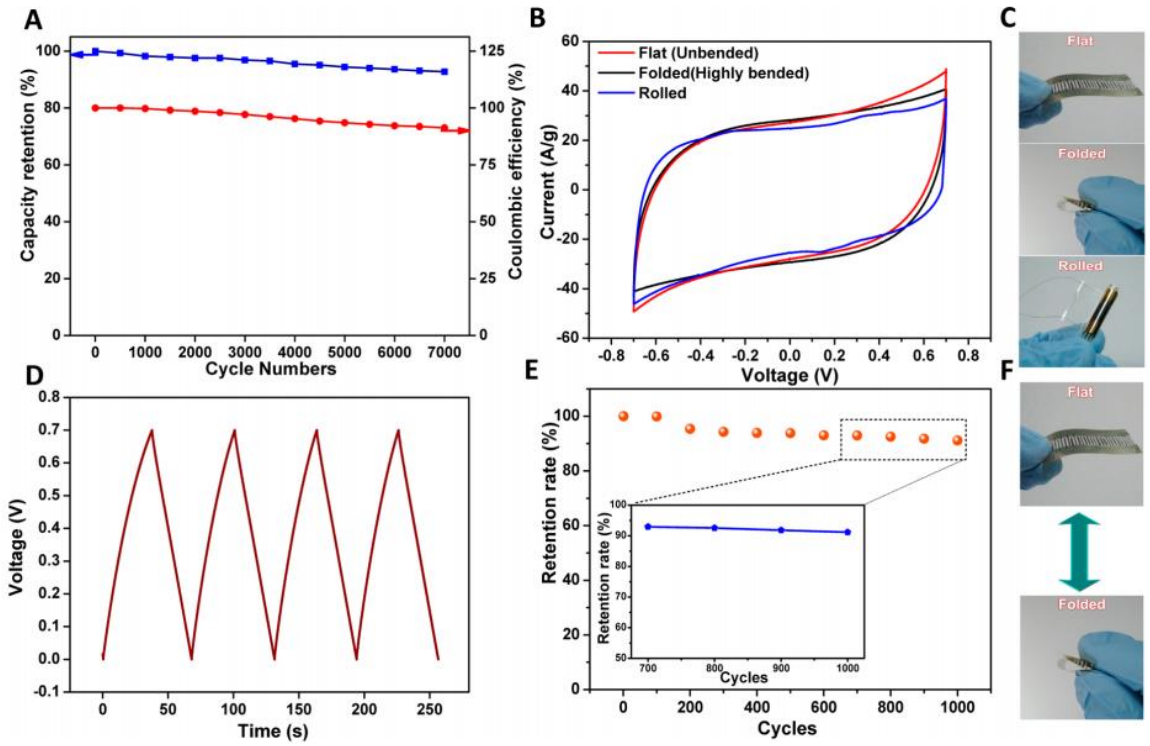


**Figure 3.13. Cycling performance of ultraflexible planar supercapacitors based on hybrid thin film.** (A) Capacitance retention (blue) and Coulombic efficiency (red) of the planar supercapacitor device over 7000 charge-discharge cycles. (B) CV curves for the planar supercapacitor under three different bending states. (C) Demonstration of three different bending states: flat, folded, and rolled. (D) Typical CD curves of the planar supercapacitor based on hybrid thin film at current density of 5 A $g^{-1}$. (E) Cycling stability under repeated flat/folded cycles. (F) Demonstration of the flat/folded cycle when testing cycling stability

### *3.3.4.3 Comparison of the traditionally sandwiched type supercapacitors and planar supercapacitors*

The planar supercapacitors based on 2D in-plane hybrid design have achieved impressive electrochemical performance compared with traditional 3D sandwich-type supercapacitors based on TMOs such as $MnO_x$, $MoO_x$, and $VO_x$ (**Figure 3.14**).[64, 65] They also exhibit the significant performance enhancement over graphene-only based

supercapacitors in aqueous electrolytes with higher energy and power density, as shown in Figure 3.12F. For previously reported planar supercapacitors based on graphene-only thin films, the densely packed layer structure of graphene-only nanosheets will hinder efficient charge transport, especially for the electrolyte ion diffusion. To mitigate this problem, we established the novel 2D hybrid structures based on 2D hybrids of $\delta$-$MnO_2$ nanosheets integrated on graphene sheets. The heterogeneous integration of $\delta$-$MnO_2$ ultrathin nanosheets onto graphene can potentially relieve the densely stacking problem as that in the graphene-only thin films, and thus allow for more electrolyte ions to penetrate efficiently into the hybridized film and for effective utilization of more active surface areas. Moreover, the uniquely hybridized $\delta$-$MnO_2$/graphene interlayer areas provide additional interfaces, where the conducting graphene could greatly facilitate electron conduction during the charging/ discharging process. In our case, the material selection of hexagonal $\delta$-$MnO_2$ nanosheets is also a key for enhancing the performance of planar supercapacitors, since $\delta$-$MnO_2$ nanosheets bring more side-exposed manganese atoms, introducing extra surfaces and serving as the chemically active sites for the pseudocapacitive reactions during the charge/discharge process.


**Figure 3.14. Schematic comparison of the traditional sandwich-type supercapacitor (left) and planar supercapacitor (right).**

#### *3.3.4.4 Electrochemical performance of flexible thin-film supercapacitors based on 2D $VOPO_4$/graphene*

To further study the electrochemical properties of the $VOPO_4$ graphene-like materials, a flexible all-solid-state pseudocapacitor based on the 2D $VOPO_4$/graphene hybrid film was fabricated. The devices were configured and fabricated according to the typical principles of flexibility, ultra-thinness, and all-solid-state, as illustrated in **Figure 3.15**A. In this regard, $VOPO_4$/graphene hybrid film was transferred onto the gold-coated polyethylene terephthalate (PET) sheet as the working electrode. The polyvinyl alcohol (PVA)/LiCl was introduced as the solid electrolyte and separator to prevent potential dissolving of the active material of $VOPO_4$ nanosheets. Note that the LiCl salt could not be easily crystallized out during the process of gel drying and could provide a neutral pH medium, which makes PVA/LiCl an excellent electrolyte for vanadium-involved solid-state pseudocapacitors. The as-assembled pseudocapacitors exhibited excellent electrochemical performance. **Figure 3.15** summarizes the electrochemical performance of the as-fabricated pseudocapacitors based on $VOPO_4$/graphene ultrathin film with a thickness of ~90 nm. Figure 3.15B shows the cyclic voltammetry (CV) curve in the PVA/LiCl electrolyte from 0 to 1.2 V at scan rate of 0.1 mV $s^{-1}$. The obvious redox current peaks at ~1.1 V (oxidation peak) and 0.9 V (reduction peak) in the CV plots correspond to the reversible pseudocapacitive reactions of $VOPO_4$ nanosheets with lithium-ion.

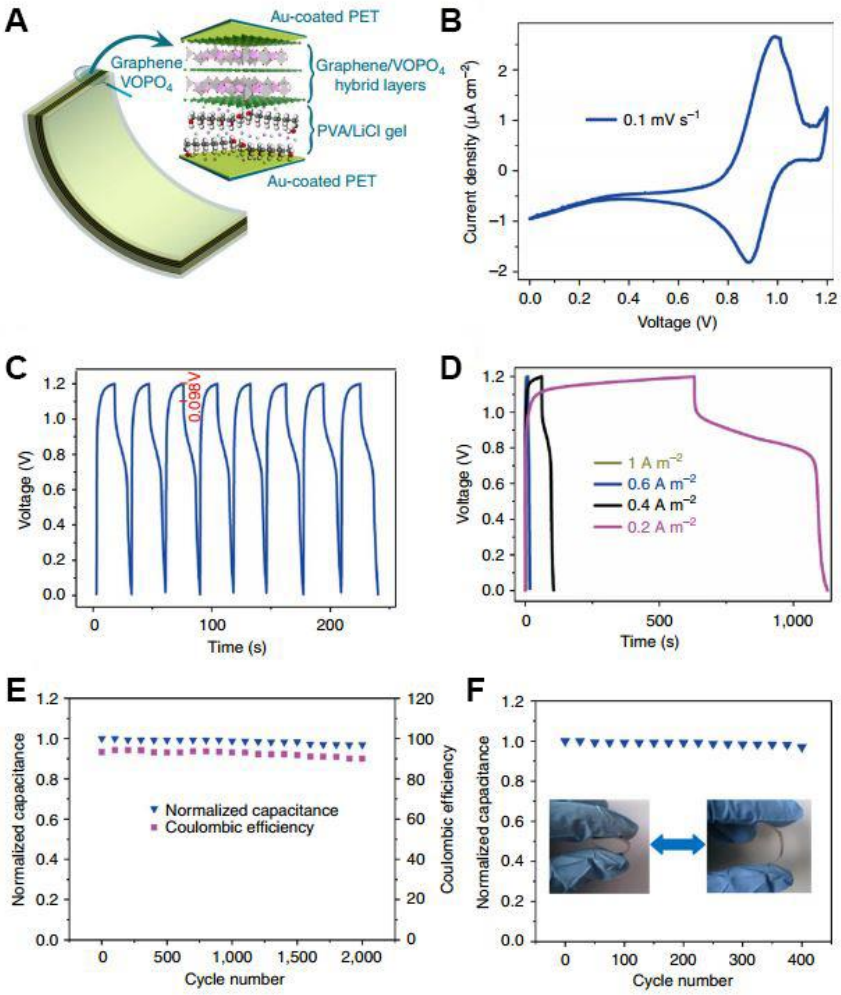


**Figure 3.15. Electrochemical performance of $VOPO_4$/graphene based pseudocapacitors.** (A) Schematic illustration of an as-fabricated flexible ultrathin-film pseudocapacitor. (B) CV curves from 0 to 1.2 V at 0.1 mV $s^{-1}$. (C) Galvanostatic cycling behavior and its IR drop. (D) Galvanostatic charge–discharge curves at different current density of 0.2, 0.4, 0.6 and 1 A $m^{-2}$. (E) Cycle test over 2,000cycles. (F) Cycling stability under repeated bending/extending deformation

The slight internal resistance (IR) drop of 0.098 V observed in Figure 3.15C implies a small intrinsic series resistance of $VOPO_4$/graphene hybrid film. Figure 3.15C shows the galvanostatic charge–discharge curves, from which the specific capacitance is calculated to be 8,360.5 μF $cm^{-2}$ at current density of 0.2 A $m^{-2}$. Our areal capacitance

of 8,360.5 μF $cm^{-2}$ (that is, 928.9 F $cm^{-3}$) is the highest value among all reported flexible pseudocapacitors. The electrochemical performance of 2D $VOPO_4$/graphene hybrid thin film is superior to that of bulk $VOPO_4$, that of pure 2D $VOPO_4$ nanosheets and even to that of other crystal forms of $VOPO_4$. Moreover, the flexible pseudocapacitors fabricated with higher mass loading of active materials (thickness up to ~10 μm) can still maintain good electrochemical performance, in which the areal capacitance increased 72 times when the thickness of electrode increased from ~90 nm to ~10 μm. (**Figure 3.16**). Employing pseudocapacitor in-plane, micro-electrodes can potentially further enhance the performance of 2D hybrid $VOPO_4$/graphene thin film, as it could mitigate the issues from contact resistance and electrolyte ions diffusion in the case of much higher mass loading.[66] Furthermore, the discharge voltage up to ~1.0 V is a significant step for constructing high energy density supercapacitors. Our reported discharge voltage up to 1.0 V is a fairly high value compared with previously reported supercapacitors in the aqueous electrolytes. The high specific capacitance (8,360.5 μF $cm^{-2}$) and redox voltage (up to 1.0 V) lead to the ultrahigh energy density of 1.7 mWh $cm^{-2}$ and power density of 5.2 mW $cm^{-2}$. The improved energy density of the as-fabricated flexible pseudocapacitors would make it more competitive for practical applications of energy storage devices.[67] As shown in Figure 3.15E, the as-fabricated flexible pseudocapacitors have an excellent cycle life, as after 2,000 charge–discharge cycles specific capacitance retained 96% of the initial capacitance and coulombic efficiency is kept at ~90%, demonstrating excellent long-term cycling stability. Figure 3.15F demonstrates the excellent flexibility with negligible degradation of the specific capacitance even after 400 bending cycles. In short, the graphene-like $VOPO_4$ materials have shown the fascinating electrochemical and mechanical characteristics for practical applications in high

performance, flexible energy storage devices catering for portable and flexible electronics.

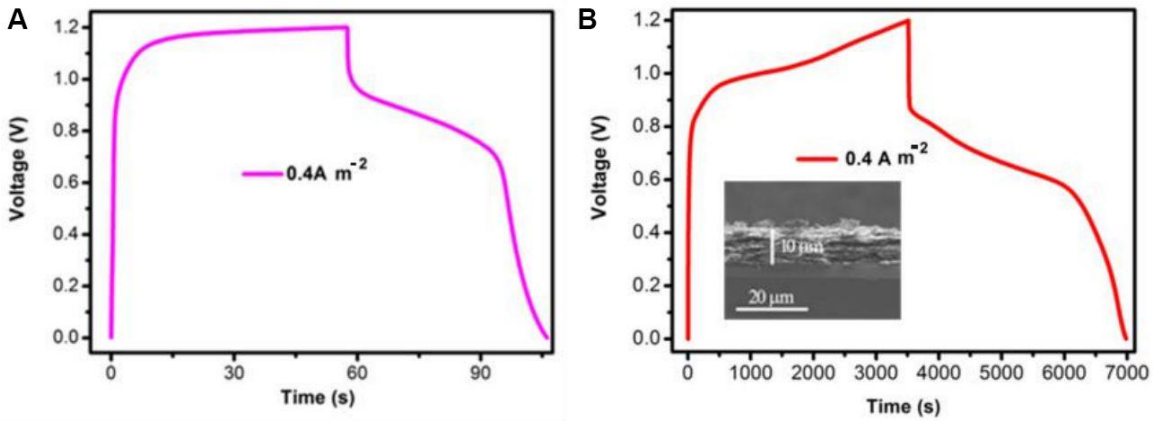


**Figure 3.16. Electrochemical performance of hybrid thin films with different thickness.** Galvanostatic charge/discharge curves of $VOPO_4$/graphene hybrid film with a thickness of 90 nm (A) and $VOPO_4$/graphene with a thickness of 10 μm (B) based flexible pseudocapacitor.

### *3.3.4.5 Electrochemical performance of the $VOPO_4$ nanosheets for lithium-ion storage*

The electrochemical behavior of $VOPO_4$ nanosheets electrode in potentiodynamic mode (0.02 mV $s^{-1}$) showed a multistep intercalation process, similar to the previous study on bulk $VOPO_4 \cdot 2H_2O$.[68] However, at a higher rate (0.1 mV $s^{-1}$) nanosheets and bulk chunks electrodes showed large differences (**Figure 3.17**A). The redox peak profile of nanosheets was much more symmetric and sharper than that of bulk chunks and individual peaks could still be resolved, while the latter only showed two broad peaks. Moreover, for nanosheets electrode the polarization between the charge/discharge curves is small (~130 mV), whereas for bulk chunks electrode the value is much larger (~320 mV). Both demonstrate that the redox kinetics are much better in nanosheets electrode. This could be explained as a larger surface-to-volume ratio as a result of 2D thin

nanosheets morphology compared to bulk chunks. Such improved redox kinetics may contribute to the high capacity at high current densities, that is, superior rate and cycling performance compared to bulk counterparts. This was clearly observed in the rate performance of the $VOPO_4$ nanosheets electrode and the $VOPO_4 \cdot 2H_2O$ bulk chunks electrode (Figure 3.17B). At a relatively low current density of 0.1 C, both electrodes delivered comparable reversible capacities, for instance, ca. 154 (93% of the theoretical value) and 141 mAh $g^{-1}$ for nanosheets electrode and bulk chunks electrode, respectively. However, a cell assembled from bulk chunks' electrode lost nearly half of the initial capacity in less than 10 cycles at 0.1 C rate. In contrast, cell assembled from nanosheets electrode exhibited distinctly stable electrochemical performance, maintaining its capacity at the same rate. Impressively, the nanosheets electrode was able to deliver reversible capacities of 154, 146, 141, 133, 118, 99, and 74 mAh $g^{-1}$ at C rate of 0.1, 0.2, 0.5, 1, 2, 5 and 10, respectively, while bulk chunks' electrode only delivered less than 70 mAh/g at 0.2 C rate and was barely rechargeable at the current rate higher than 5 C. In addition, the average reversible capacity of nanosheets reaches approximately 100 mAh/g at a current rate of 5 C and is sustained for 500 cycles with no obvious capacity decay (Figure 3.17C).

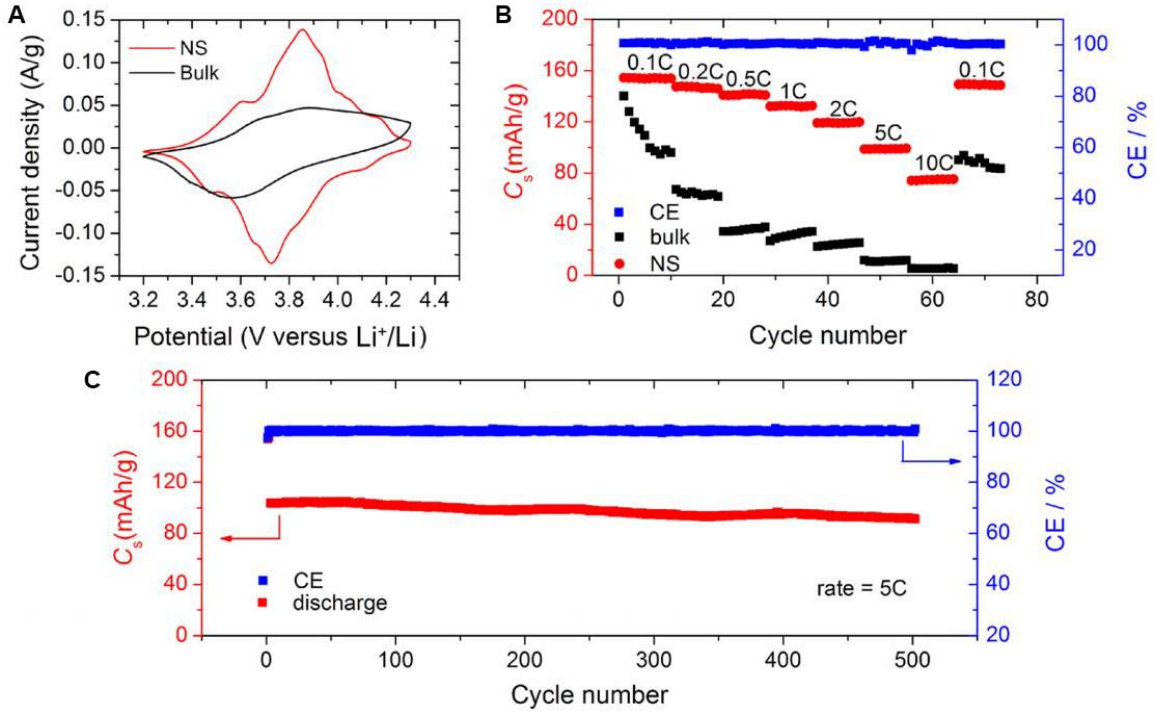


**Figure 3.17. Electrochemical performance of the $VOPO_4$ nanosheets electrode in lithium storage device.** (A) Cyclic voltammetric profiles of $VOPO_4$ nanosheets (NS, red) and $VOPO_4 \cdot 2H_2O$ chunks (bulk, black) at a fixed scan rate of 0.1 mV $s^{-1}$. (B) Rate capability at the C rate ranging from 0.1−10 C. (C) Specific capacity ($C_s$) retention at 5 C rate and corresponding coulumbic efficiency (CE).

### *3.3.4.6 Kinetics analysis of the electrochemical behavior toward $Li^+$ for the $VOPO_4$ nanosheets electrode*

To examine the possible reasons for the improved rate capability and cycling stability of the nanosheets electrode, detailed kinetics analysis was conducted for lithium storage device. Cyclic voltammetry (CV) measurements were carried out to further understand the electrochemical kinetics of nanosheets electrode. The CV curves at various scan rates from 0.02 to 2 mV $s^{-1}$ display similar shapes and a gradual broadening of the peaks can be observed (**Figure 3.18**A). For an electrochemical energy storage device, several processes could contribute to total stored charge and they can be characterized by analyzing the CV data at various sweep rates according to to[69]

$$i = a\upsilon^b$$

where the measured current *i* obeys a power law relationship with the sweep rate $\upsilon$ and *a* and *b* are adjustable parameters. In particular, the *b*-value of 0.5 indicates a total diffusion controlled process, whereas 1.0 represents a capacitive process.[70] By plotting to *log i* vs *log* $\upsilon$, *b*-values determined as the slopes and 0.86 and 0.92 were calculated for cathodic and anodic peaks (Figure 3.18B), indicating that the majority of the current at the peak potential is capacitive. A similar observation was reported on *T*-$Nb_2O_5$ films and $TiO_2$ nanosheets.[71] The total capacitive contribution at a certain scan rate could be quantified by separating the specific contribution from the capacitive and diffusion-controlled process at a particular voltage according to to[70]

$$i(V) = k_1\upsilon + k_2\upsilon^{1/2}$$

where $k_1$ and $k_2$ are constants for a given potential. By plotting $i(V)/\upsilon^{1/2}$ versus $\upsilon^{1/2}$, $k_1$ is determined as the slope, therefore capacitive and diffusion contributions can be obtained. For example, at scan rate 1 mV $s^{-1}$ (Figure 3.18C), ~90% of the total current, namely the capacity, is capacitive in nature. In the cathodic sweep, the diffusion-controlled process appears during the initial lithium-ion intercalation and mostly at the peak voltage of 3.6 V. In the anodic sweep, nearly all of the diffusion-controlled contributions occur at around the peak voltage. Both demonstrate that the diffusion process is feasible at regions corresponding to the redox reaction between $V^{5+}/V^{4+}$.[45] Similarly, contribution ratios between the two different processes at other scan rates were calculated (Figure 3.18D). The quantified results show that the capacitive contribution gradually improves with increasing the scan rate. It is interesting to note at very low scan rate, for example, 0.02 mV $s^{-1}$, the capacitive contribution is already significant (~64%). On the other hand, it is very likely that capacitive contribution in bulk chunks electrode would be minimum, as indicated by the low specific capacity at relatively high C rate. For $VOPO_4$ nanosheets,

both the calculated *b*-value and capacitive contribution clearly demonstrate the unique characteristic behavior as a result of intercalation pseudocapacitance, which is different from charge storage mechanism in classical batteries, for example, $LiFePO_4$. Combined with prior structural characterization, it can be concluded that charge storage in $VOPO_4$ nanosheets follows intercalation pseudocapacitive mechanism.

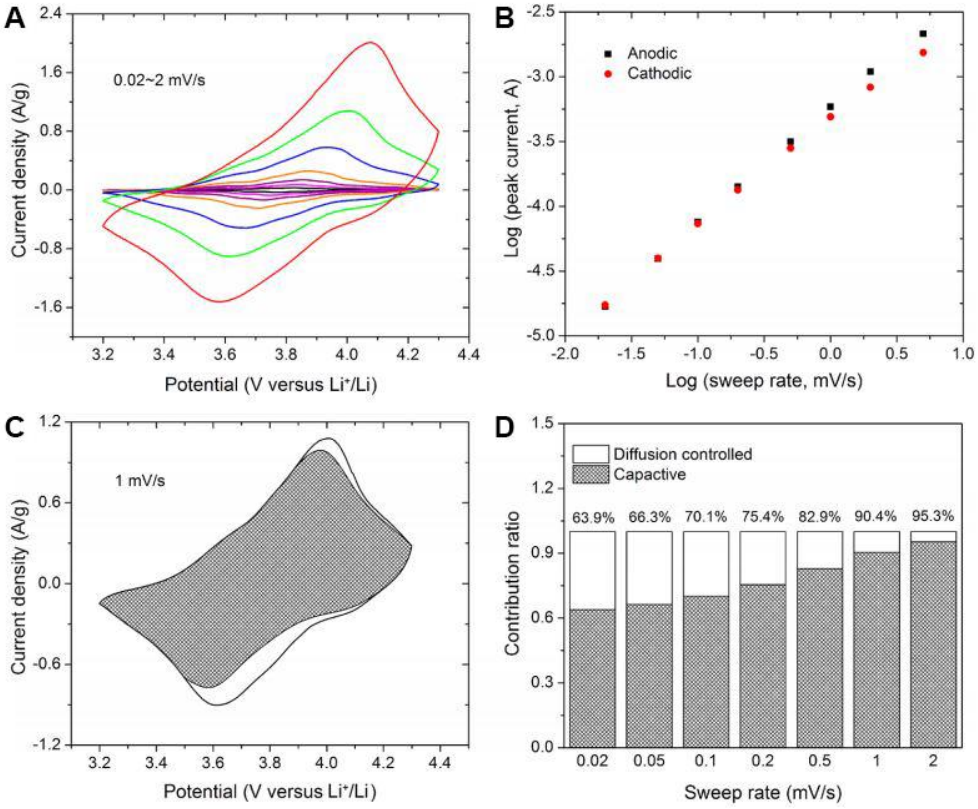


**Figure 3.18. Kinetics analysis of the electrochemical behavior toward $Li^+$ for the $VOPO_4$ nanosheets electrode.** (A) CV curves at various scan rates from 0.02 to 2 mV $s^{-1}$. (B) Determination of the *b*-value using the relationship between peak current and scan rate. (C) Separation of the capacitive and diffusion currents at a scan rate of 1 mV $s^{-1}$. (D) Contribution ratio of the capacitive and diffusion-controlled charge at various scan rates.

### *3.3.4.7 Electrochemical performance of the $VOPO_4$ nanosheets for sodium-ion storage*

Though $VOPO_4$ system has been previously exploited as cathode materials for LIBs,[72] its application in high-performance SIBs have been rarely reported. The sodium-ion storage properties of $VOPO_4$ nanosheets are summarized in **Figure 3.19**. As shown in the charge/discharge profiles (Figure 3.19A), $VOPO_4$ nanosheets electrode was able to deliver capacities of 136, 127, 114, 101, 87, 70, and 48 mAh $g^{-1}$ at C rate of 0.1, 0.2, 0.5, 1, 2, 5 and 10, respectively. All the values are less than those in lithium-ion cell at the same C rate, as expected from the kinetics analysis. However, the capacities are still superior to those of the cell made from bulk chunks, especially at high C rates. For example, after 5 C the latter showed almost zero capacity and could not recover any capacity when C rate changed back to 0.1 C after 10 C rate. A slight capacity drop occurred in the rate performance test when the C rate changed back to 0.1 (Figure 3.19B), which was absent in the case of lithium-ion cell. This electrochemical instability was more noticeable in the cycling test, in which the initial capacity of nanosheets reaches approximately 73 mAh $g^{-1}$ at a current rate of 5 C and the capacity retention is 73% after 500 cycles (Figure 3.19C). It was found the surface of nanosheets electrode became rough after long-term cycles in the sodium-ion cell, while in lithium-ion cell, the surface remained clean and smooth (**Figure 3.20**). In both cases, the nanosheets morphology remained intact, similar to that of the electrode before cycling test. Therefore, the rough surface may be a possible reason for the capacity decay in sodium-ion cell and further investigation is required.

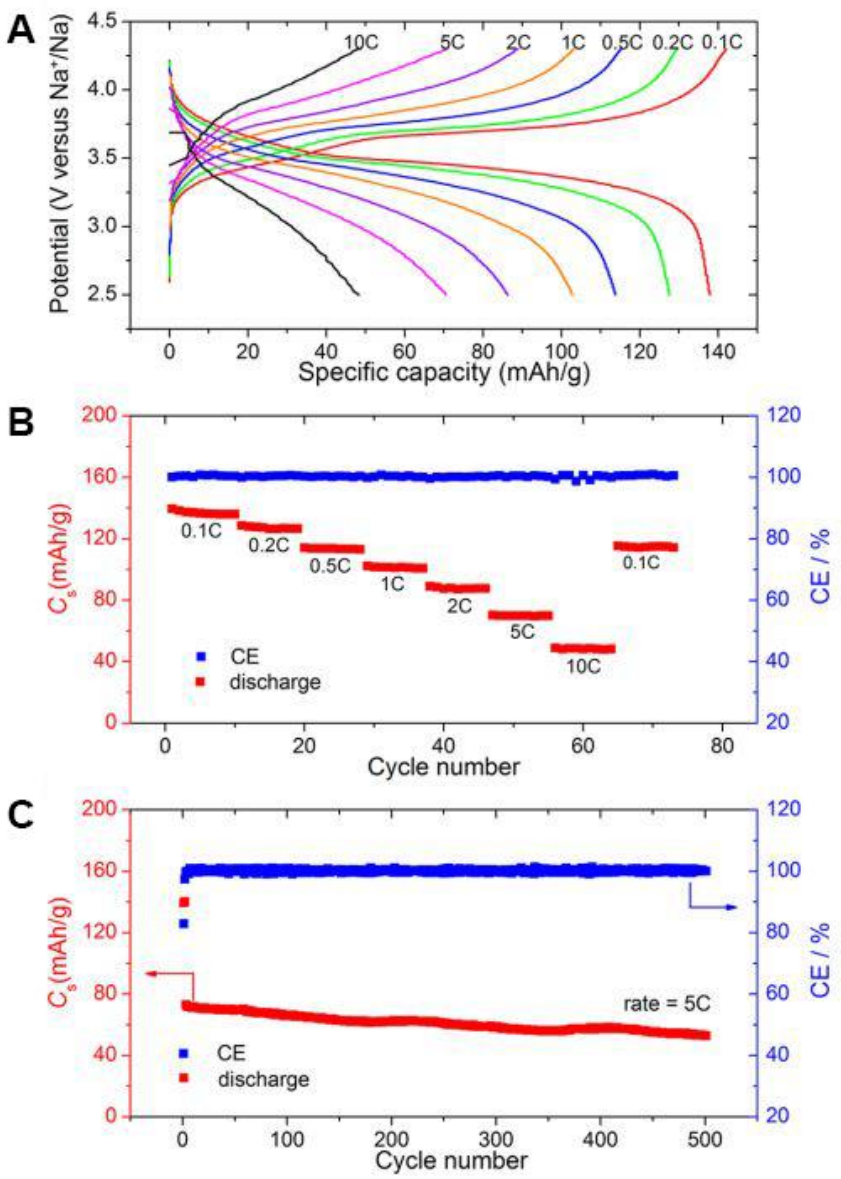


**Figure 3.19. Electrochemical performance of the $VOPO_4$ nanosheets electrode in sodium storage device.** (A) Charge/discharge profiles at various current rates from 0.1 to 10 C. (B) Rate capability at the C rate ranging from 0.1−10 C. (C) Specific capacity ($C_s$) retention at 5 C rate and corresponding coulumbic efficiency (CE).

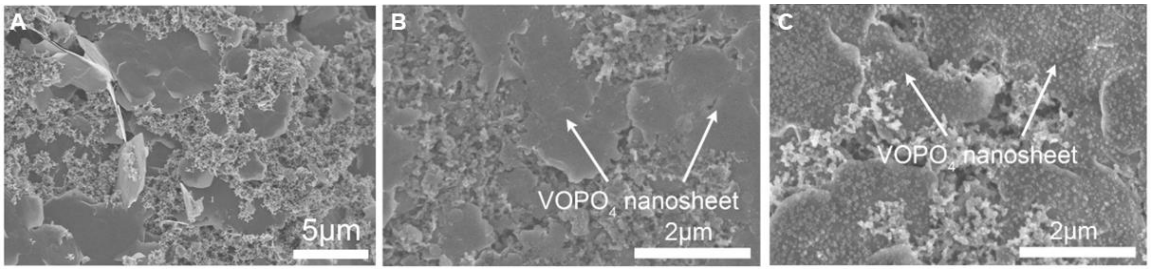


**Figure 3.20. Top-view SEM characterizations of $VOPO_4$ nanosheet electrodes before and after cycling tests.** (A) Top-view SEM image of $VOPO_4$ nanosheets electrode before cycling test. (B) $VOPO_4$ nanosheet electrodes after cycled in lithium storage device. (C) In sodium storage device, the surface of $VOPO_4$ nanosheets became rather rough.

### *3.3.4.8 Kinetics analysis of the electrochemical behavior toward $Na^+$ for the $VOPO_4$ nanosheets electrode*

Sodium-ion batteries represent potential alternatives of lithium-ion batteries for large-scale energy storage due to low cost and resource abundance. Inspired by the superior rate performance and cycling stability of lithium storage devices, the same CV measurements, and kinetic analysis were performed on sodium-ion cells (**Figure 3.21**). Several differences can be spotted when compare the kinetics in lithium- and sodium-ion cells (**Table 3.1**). First, the calculated *b*-values for cathodic and anodic peaks in sodium-ion cell are 0.68 and 0.71, smaller than those in lithium-ion cell, but still larger than 0.5. This indicates a mixture of diffusion-controlled and capacitive processes. Second, for sodium-ion cell, the capacitive contribution at low scan rate (0.02 mV $s^{-1}$) is significantly smaller than that in lithium-ion cell. Third, polarization between the charge/discharge curves is high (340 mV), even at low scan rate (0.02 mV $s^{-1}$). All above observations conclude a relatively inferior kinetics in the sodium-ion cell and this can be understood as the sodium-ion cell has higher diffusion barrier, which is commonly observed for sodium version of the lithium-ion intercalation materials and supported by theoretical calculation.[73, 74] Despite such an obvious disadvantage, the calculated *b*-values still

signify reasonable rate performance resulted from large capacitive contributions as shown at high scan rates.

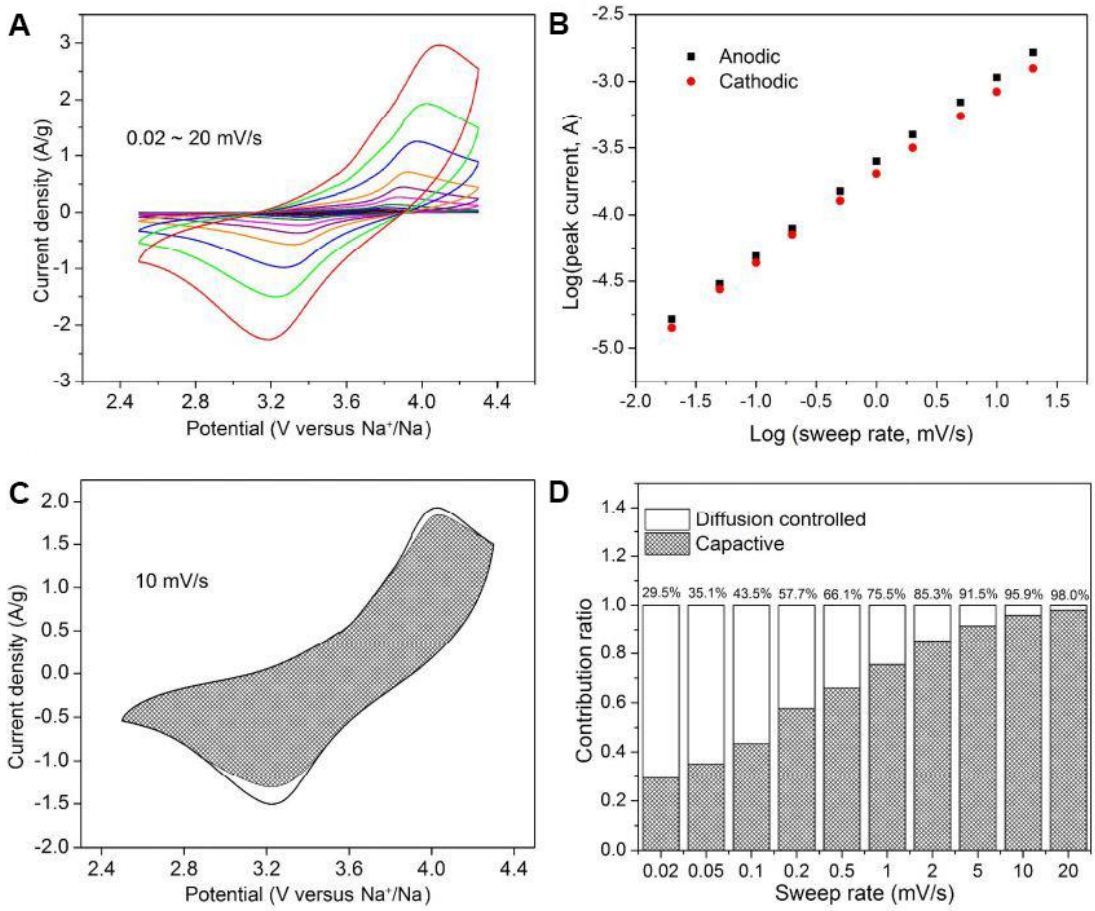


**Figure 3.21. Kinetics analysis of the electrochemical behavior towards $Na^+$ for the $VOPO_4$ nanosheets electrode.** (A) CV curves at various scan rates, from 0.02 to 20 mV $s^{-1}$. (B) Determination of the *b*-value using the relationship between peak current and scan rate. (C) Separation of the capacitive and diffusion currents at a scan rate of 10 mV $s^{-1}$. (D) Contribution ratio of the capacitive and diffusion-controlled charge at various scan rates.

| | CV scan range (mV/s) | *b*-value cathodic/anodic | Capacitive contribution at 0.02 mV/s | Polarization at 0.02 mV/s (mV) |
|---|---|---|---|---|
| Li | 0.02~2 | 0.86/0.92 | 63.9% | 130 |
| Na | 0.02~20 | 0.68/0.71 | 29.5% | 340 |

**Table 3.1. Comparison of electrochemical performance of $VOPO_4$ nanosheets electrode in lithium and sodium storage devices**

### *3.3.4.9 Investigation of $VOPO_4$ nanosheets for high-energy sodium-ion full battery*

To further evaluate the electrochemical performance of $VOPO_4$ nanosheets, we assemble the sodium-ion full battery by matching $VOPO_4$ nanosheet cathodes with the layered $Na_2Ti_3O_7$ nanomaterials. **Figure 3.22** shows the design rule of the sodium-ion full battery based on the $VOPO_4$ nanosheets and layered $Na_2Ti_3O_7$ nanomaterials. $VOPO_4$ nanosheets and layered $Na_2Ti_3O_7$ nanomaterials all exhibit sodium-ion insertion/exaction mechanism with distinct redox peaks and plateaus (Figure 3.22A and C).

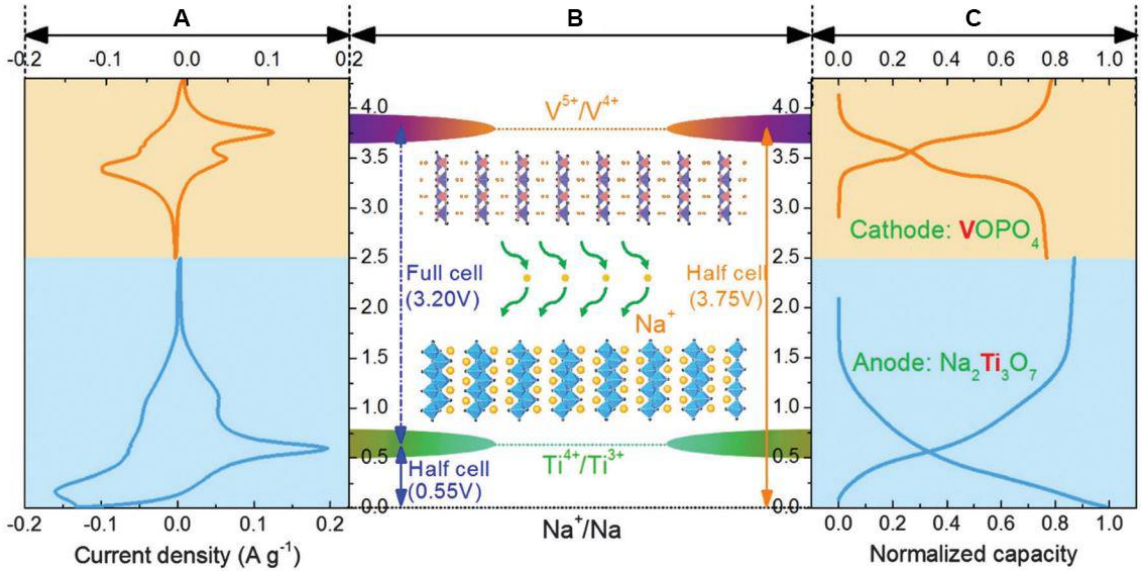


**Figure 3.22. Design rule of $Na_2Ti_3O_7$ and $VOPO_4$ based sodium-ion full battery.** (A) CV curves of $VOPO_4$ nanosheets and layered $Na_2Ti_3O_7$ nanomaterials for sodium-ion half-battery. (B) Structural properties of the $VOPO_4$ nanosheets and layered $Na_2Ti_3O_7$ nanomaterials. (C) The typical charge–discharge profiles of $VOPO_4$ nanosheets and layered $Na_2Ti_3O_7$ nanomaterials.

The sodium-ion full battery based on $VOPO_4$ nanosheets and layered $Na_2Ti_3O_7$ nanomaterials is investigated under galvanostatic cycling conditions at room temperature in the voltage window of 1.8–3.8 V. **Figure 3.23**A illustrates the representative CV curve of a $Na_2Ti_3O_7$//$VOPO_4$ full cell at a scanning rate of 0.1 mV $s^{-1}$. Two well-defined peaks can be observed at 2.86 V (cathodic sweep) and 3.19 V (anodic sweep), which are consistent with the predicted values in Figure 3.23B. The rate capability test shown in Figure 3.23C demonstrates that the full cell can be effectively cycled at different rates of 0.1C, 0.2C, 0.5C, 1C, 2C, and 5C. The capacity varies from 114 mAh $g^{-1}$ at a 0.1C rate to 102 mAh $g^{-1}$ at a 0.5C rate. Even at a rate of 2C, the discharge capacity remains at 74 mAh $g^{-1}$, approximately 65% of the reversible capacity at a rate of 0.1C. Figure 3.23D shows the cycling performance and corresponding coulombic efficiency tested at a rate of 1C. It is worth noting that more than 92.4% capacity still remains after 100 desodiation

and sodiation cycles, indicating the outstanding cycling stability of the $Na_2Ti_3O_7$// $VOPO_4$ based full cell. We are not aware of other asymmetric sodium-ion full cells that are capable of meeting these performances so far.

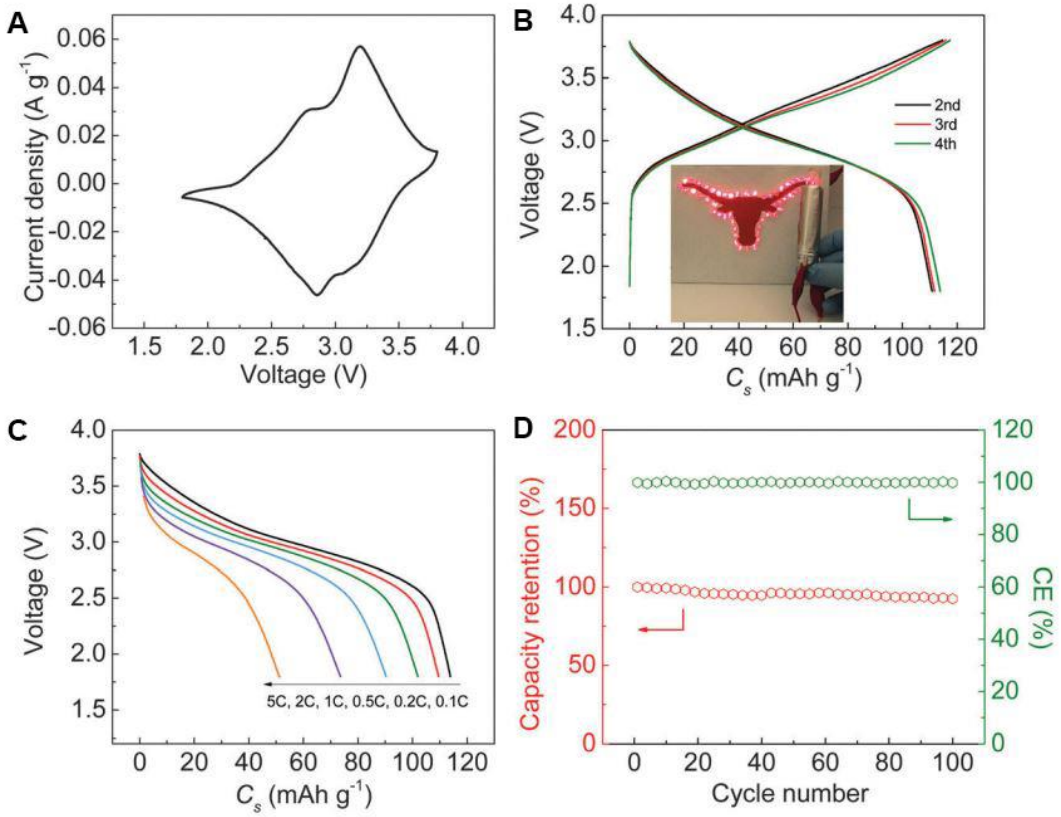


**Figure 3.23. Electrochemical performance of $Na_2Ti_3O_7$//$VOPO_4$ full cells.** (A) CV curve profile at a scan rate of 0.1 mV $s^{-1}$. (B) The typical charge/discharge profiles between 1.8 and 3.8 V at a rate of 0.1C (a rate of 1C corresponds to 100 mA $g^{-1}$). The inset shows an array of commercial red LEDs for UT logo (longhorn) powered by the assembled full cell under rolled state. (C) The capacity at different rates of 0.1C, 0.2C, 0.5C, 1C, 2C and 5C (each curve represents the second cycle at the corresponding C-rate). (D) The capacity retention with coulombic efficiency at a 1C rate showing the outstanding cycling performance (92.4% capacity retention after 100 cycles).

**Figure 3.24** summarizes many recently reported sodium-ion full cell configurations, where their main electrochemical parameters such as voltage, capacity,

energy density and power density are concluded in the plots. In comparison, our $Na_2Ti_3O_7$//$VOPO_4$ full cells display superior electrochemical performances. Furthermore, a flexible punch cell based on the $Na_2Ti_3O_7$ anode and the $VOPO_4$ cathode is fabricated to demonstrate its potential application. As shown in the inset of Figure 3.23B, the pouch cell is able to power an array of the commercial red light-emitting diode (LED) for UT logo (Longhorn) even when the cell is completely rolled.

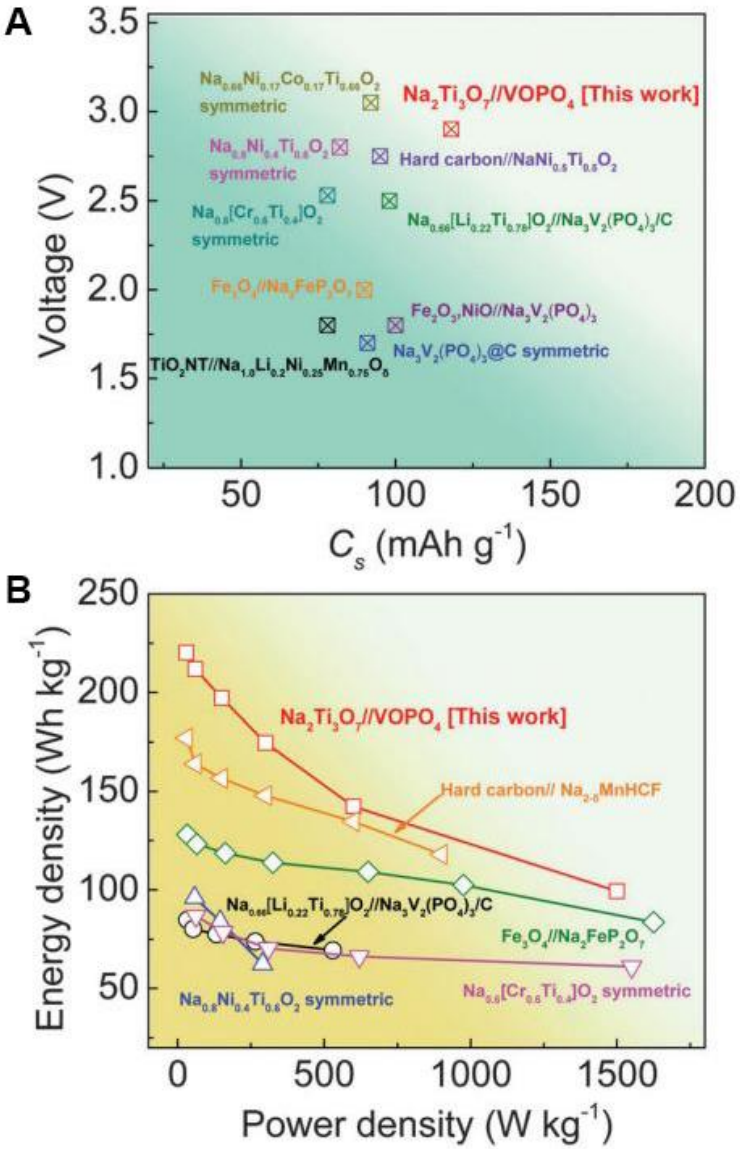


**Figure 3.24. Sodium-ion storage properties of the $Na_2Ti_3O_7$//$VOPO_4$ full cells and other recently reported literature**

### 3.4 CONCLUSIONS

In summary, we have fabricated the high-performance pseudocapacitors based on the 2D pseudocapacitive nanomaterials (ultrathin $MnO_2$ and $VOPO_4$ nanosheets) and lithium- and sodium-ion batteries based on ultrathin $VOPO_4$ nanosheets. The flexible

pseudocapacitors exhibit impressive electrochemical performance with high specific capacitance, good rate capability, and cycling performance as well as superior flexibility. The impressive electrochemical performances are attributed to the layer-by-layer planar structure. It can introduce more electrochemically active surfaces for absorption/desorption of the electrolyte ions and bring extra interface at the hybridized interlayer areas to facilitate charge transport during charge/discharge processes, offering good rate capability and cycling stability. In addition, the integrated pseudocapacitive nanosheets serving as active centers for the pseudocapacitive reactions contribute to the great enhancement of the specific capacitance. Meanwhile, the pseudocapacitive nanosheets integrated on graphene can potentially tailor the distance between each sheet of densely stacked graphene and open up the interlayer space to allow for more electrolyte ions to penetrate efficiently into the hybridized film. The rationally designed planar supercapacitors represent a promising direction for building future generation high-performance, flexible energy storage devices as the power back-ups for stretchable/flexible electronic devices. Ultrathin $VOPO_4$ nanosheets display high reversible capacities for lithium and sodium ion storage, as well as excellent rate and cycling performance. Kinetics analysis confirms the $Li^+/Na^+$ intercalation pseudocapacitive behavior in the $VOPO_4$ nanosheets and also reveals a high contribution of capacitive charge. Our study provides a direction on developing electrode materials of electrochemical energy devices with high-rate capability for alkali-ion storage and we anticipate that the demonstrated intercalation pseudocapacitive mechanism will find application in new material systems or old materials with proper structural engineering.

# Chapter 4: Bottom-up synthesis of 2D $LiFePO_4$ nanosheets for lithium-ion batteries*

## 4.1 INTRODUCTION

Next-generation rechargeable lithium-ion batteries with high performance, especially higher energy and power densities and longer cyclic life are very urgent to meet the ever-increasing energy demands.[75] Metal phosphate is a promising cathode material system for lithium-ion batteries owing to its high operating voltage, large theoretical capacity, and thermal stability, as well as being inexpensive, nontoxic, and environmentally benign.[76] For instance, olivine orthophosphate lithium iron(II) phosphate ($LiFePO_4$) shows a high operating voltage of ~3.4 V vs $Li/Li^+$ and a large theoretical capacity of ~170 mAh $g^{-1}$. The electrochemical properties, however, are greatly restricted by the sluggish kinetics originating from low electronic and ionic conductivity.[77-80] Many efforts have been devoted to overcoming the ionic and electronic transport limitations by various methods. The former limitation is extensively studied with success by modification of the interface of $LiFePO_4$ particles with electrolyte through coating/doping to lower the charge transfer resistance.[81-83] For the latter one, both the size and morphology control of $LiFePO_4$ is necessary because lithium-ion diffusion in $LiFePO_4$ can only occur along [010] direction unlike layered or spinel cathode materials, which possess multiple diffusion directions for lithium-ion. In this regard, it appears that controlled synthesis of cathode materials with specific morphology can serve as an effective solution to improve the electrochemical properties.

---

* Y. Zhao,† L. Peng,† B. Liu, G. Yu, "Single-Crystalline $LiFePO_4$ Nanosheets for High-Rate Li-Ion Batteries" *Nano Lett.*, **2014**, *14*, 2849.
P. Xiong,† L. Peng,† D. Chen, Y. Zhao, X. Wang, G. Yu, "Two-Dimensional Nanosheets Based Li-ion Full Batteries with High Rate Capability and Flexibility" *Nano Energy*, **2015**, *12*, 816.
L. Peng co-carried out the experiments, co-analyzed the results, and co-wrote the paper. G. Yu supervised the project. All participated in the preparation of the project.

Rational design and facile synthesis of 2D nanomaterials have attracted extensive attention in recent decades. Among the numbers of methods have been developed to prepare 2D nanomaterials, general routes are mechanical exfoliation or direct liquid-phase exfoliation of their layered crystals. Almost all bulk layered crystals can be exfoliated in common solvents (such as NMP, IPA) to give mono- and few-layer nanosheets. Unfortunately, scalable synthesis of 2D nanomaterials via exfoliation is still challenging. Moreover, based on these top-down synthesis strategies, only a few kinds of 2D nanomaterials possessing suitably layered crystal matrix can be obtained. Therefore, it is highly desirable to explore a scalable approach for the synthesis of various 2D materials especially these not having layered host materials.

In this chapter, we report the facile synthesis of 2D $LiFePO_4$ nanosheets from the intrinsically non-layered olivine structures as cathodes for lithium-ion batteries. To demonstrate the feasibility to improve the electrochemical properties via controlled synthesis of cathode materials with specific morphology, 2D $LiFePO_4$ nanosheets with {010} facet exposed are studied as the cathodes for LIBs. We report here the preparation of single-crystalline, {010}-oriented $LiFePO_4$ nanosheets with thickness down to tens of nanometers (30−60 nm) via solvothermal synthesis by using diethylene glycol as solvent and surface modifier reagent. The as-prepared $LiFePO_4$ nanosheets provide large effective surface areas that allow carbon coating and electrolyte penetration, improving the electronic conductivity and reducing the diffusion path of lithium-ion. This feature, combined with the high tap density, results in battery electrodes offering high volumetric energy density, impressive rate capability, and excellent cycling stability.

## 4.2 EXPERIMENTAL DETAILS

### 4.2.1 Preparation of bulk $LiFePO_4$ powders

The preparation of bulk $LiFePO_4$ powders was carried out under solvothermal reaction with diethylene glycol as solvent. Firstly, $FeCl_2 \cdot 4H_2O$ (3 mmol, Fisher Scientific) and LiCl (3 mmol, Acros) were dissolved in diethylene glycol (20 mL, Acros) with magnetic stirring to form a light green transparent solution. Afterward, $LiH_2PO_4$ (3 mmol, Fisher Scientific) was dissolved in deionized water (0.5 mL) and slowly added into diethylene glycol with magnetic stirring until greyish green homogenous suspension formed. The preparation of the precursor solution was carried out under Ar atmosphere with the presence of traces of L-ascorbic acid (Acros, 5% with respect to the weight of $FeCl_2 \cdot 4H_2O$) to avoid the oxidation of $Fe^{2+}$. Then, the precursor solution was transferred into a glass vial which was directly put into the Teflon pot. Finally, the Teflon pot was put into the stainless steel autoclave and kept at 200 °C for sufficient time. Typically, solvothermal treatment for 24 hours yields light greenish white, phase pure bulk $LiFePO_4$ powders.

### 4.2.2 Preparation of $LiFePO_4$ nanosheets and carbon coating

Single-crystalline $LiFePO_4$ nanosheets could be readily obtained by the exfoliation of bulk $LiFePO_4$ powders. In a typical procedure, bulk $LiFePO_4$ powders (1 g) and 2-propanol (10 mL, Aldrich) were mixed and exposed to ultrasonication. The white suspension was collected by centrifuging and dried in vacuum. The carbon coating was achieved using polyethylene oxide (Mw. 600,000, Aldrich) as the carbon source. In a typical procedure, polyethylene oxide (10% in weight ratio), the as-prepared $LiFePO_4$ nanosheets and proper amount of deionized water were mechanically mixed in Thinky

centrifugal mixer (ARE-310) for 30 min, dried in vacuum, and annealed in $Ar/H_2$ (90/10, v/v) atmosphere at 650 °C for 12 hours.

### 4.2.3 Cell assembly

The $LiFePO_4$ nanosheets electrode was prepared by mixing the as-prepared carbon-coated $LiFePO_4$ nanosheets, Super P carbon (Timcal Graphite & Carbon), and polyvinylidene fluoride binder (Fisher Scientific) with a weight ratio of 80: 15: 5 in N-methyl-2-pyrrolidone (anhydrous, Fisher Scientific). The mixture was thoroughly mixed in the Thinky centrifugal mixer to form a homogenous slurry, which was then casted on aluminum foil and dried in vacuum at 115 °C for 12 hrs. The electrochemical performance was evaluated with a standard CR2032 coin cell using metallic lithium as the anode, Celgard 2500 as the separator, and $LiPF_6$ in 1:1 ethylene carbonate and diethyl carbonate (BASF Corp.) as the electrolyte.

### 4.2.4 Materials characterizations

X-ray powder diffraction patterns were performed on a Philips X-ray diffractometer (APD 3520) equipped with Cu Kα radiation. SEM and TEM observations were carried out on Hitachi S-5500 scanning electron microscope (S-5500) and JEOL transmission electron microscope (2010F), respectively. Raman and FTIR measurements were performed on Renishaw Raman system equipped with a 633 nm argon ion laser and Thermal Scientific FT-IR spectrometer (Nicolet™ iS™ 5), respectively. BET surface area was tested with a NOVA® surface area analyzer (Quantachrome Instruments NOVA4000). Electrochemical characterization was performed on LANHE battery cycler (CT2001A) and Bio-logic potentiostat (VMP3) equipped with impedance modules. To measure the tap density, a certain amount of the carbon-coated $LiFePO_4$ nanosheets were placed in a small measuring cylinder and tapped for 10 min by hand. The measured

volume of the tapped powder and its mass were used to calculate the tap density of the product.

## 4.3 RESULTS AND DISCUSSION

### 4.3.1 Crystal structure and surface energy of $LiFePO_4$ crystals

$LiFePO_4$ undergoes a first-order phase transformation at well-defined compositions when Li-ions are inserted/extracted along the [010] direction.[84] Engineering the Li-ion intercalation pathway through controlling the morphology of $LiFePO_4$ is of practical importance, as the intercalation kinetics directly determines its rate capability (**Figure 4.1**A). For a crystal in its thermodynamic equilibrium shape, the relative area of each facet of a particle depends on its surface free energy. In the case of $LiFePO_4$, a preference of the {010} facet on the crystal implies that the {010} surface is thermodynamically favored over other facets.[85] Though there is little theoretical prediction of the solvent effects on the stabilization of {010} facets of $LiFePO_4$, most {010}-oriented plate-like $LiFePO_4$ have been prepared under solvothermal conditions, typically using ethylene glycol as the solvent.[86-88] Though ethylene glycol is supposed to bond with Fe(II) in the reactive $FeO_5$ group at the {010} facets due to its strong chelating ability,[89] we have found that diethylene glycol also shows the strong binding effect to the {010} facet as indicated in Figure 4.1. The binding energy, which is defined as the energy difference after the absorption of solvent molecules, is −1.5 eV $mol^{-1}$ for diethylene glycol and −1.0 eV $mol^{-1}$ for ethylene glycol. The more stable binding geometry originates from the two oxygen groups of diethylene glycol available for the Fe atoms on the {010} facet. The directional alignment of diethylene glycol molecules may take place at the {010} facet and create a long chain and/or net structure as a result of hydrogen bonds between diethylene glycol molecules, thereby making the diethylene

glycol-terminated {010} surfaces more stable. The theoretical modeling results provide the guidance for the solvothermal synthesis of $LiFePO_4$ nanosheets in this chapter.

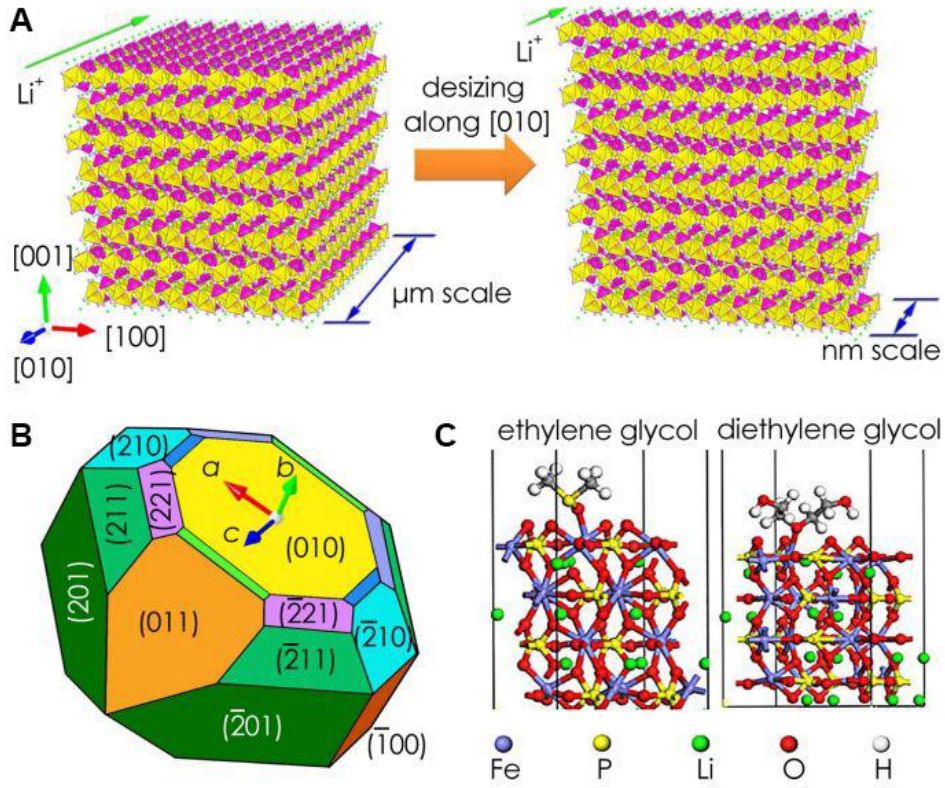


**Figure 4.1. Crystal structure and surface energy of $LiFePO_4$ crystals.** (a) Schematic illustration of shortening the lithium-ion diffusion distance along the [010]. (b) Wulff shape of $LiFePO_4$ constructed with relaxed surface energies. (c) Binding geometries of adsorbed ethylene glycol (left) and diethylene glycol (right) on $LiFePO_4$ (010) surface.

### 4.3.2 Structural characterizations of 2D $LiFePO_4$ nanosheets

The structural and phase purity characterization of the $LiFePO_4$ nanosheets is provided in **Figure 4.2**. Scanning electron microscope (SEM) images indicated that the as-prepared $LiFePO_4$ particles showed a characteristic structure assembled from latitudinally accumulated nanosheets with lateral size ~15 μm (Figure 4.2A) and

thickness of 30−60 nm (Figure 4.2B). The interaction between adjacent nanosheets is weak, as evident by the fact that bulk $LiFePO_4$ particles could be readily exfoliated into $LiFePO_4$ nanosheets with high efficiency (in minute scale) and scalability (in gram scale). The lateral size of the as-exfoliated nanosheets reached micrometer scale as shown in the inset of Figure 4.2B. The single-crystalline nature of the as-exfoliated $LiFePO_4$ nanosheets is confirmed by transmission electron microscopy (TEM). TEM image of the nanosheets (Figure 4.2C) clearly demonstrated the $LiFePO_4$ nanosheets of which the ripple-like contrast revealed their ultrathin nature. Figure 4.2D showed the high-resolution TEM (HRTEM) image and electron diffraction (ED) pattern, demonstrating the single crystalline nature of the nanosheets. The lattice spacing of 1.03 and 0.47 nm could be assigned to {001} and {100} crystal planes, respectively, indicating that the nanosheet surface was terminated by {010} facet. Considering an average thickness of the nanosheets, ∼50 nm, the effective diffusion time ($t$) for lithium-ion to diffuse over a $LiFePO_4$ nanosheet with thickness ($L$) of 50 nm was calculated to be ∼12 min (equal to the C-rate of ∼5C) assuming the phase boundary moving toward the [010] direction and lithium diffusion coefficient ($D$) of $10^{-14}$ $cm^2$ $s^{-1}$.[90] A conservative estimation could be made that the area of {010} facet exceeds 93% of the total surface area of the nanosheet, by assuming the maximum thickness and moderate width/length of the nanosheets were 100 nm and 3 μm, respectively. Note that in addition to the decrease in tap density, further reduction in thickness implies more obvious surface effects. The surface layer does not necessarily have the same properties as the bulk, with important impact on the electrochemical properties such as charge/discharge plateau shrinking[91] and surface amorphization.[92]

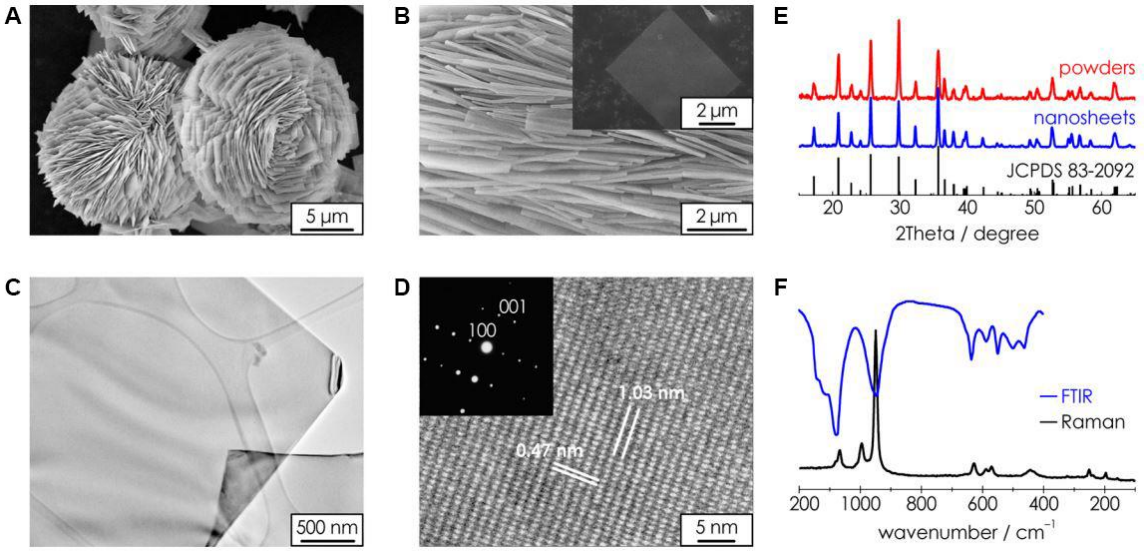


**Figure 4.2. Structural and phase purity characterization of the $LiFePO_4$ nanosheets.** (A) Representative SEM image of the as-synthesized $LiFePO_4$ particles. (B) SEM image showing the latitudinally accumulated nanosheets. Inset: an individual nanosheet obtained after exfoliation. (C) TEM and (d) HRTEM image and associated ED pattern of the $LiFePO_4$ nanosheets. (E) XRD patterns of as-synthesized $LiFePO_4$ particles and exfoliated $LiFePO_4$ nanosheets. All diffraction peaks are well consistent with standard values (JCPDS 83-2092). (F) Raman (black) and FTIR (blue) spectra of the as-exfoliated $LiFePO_4$ nanosheets.

The phase purity of the exfoliated $LiFePO_4$ nanosheets was further examined by X-ray diffraction, Raman spectroscopy, and Fourier Transform Infrared Spectroscopy (FTIR). Both the $LiFePO_4$ particles and nanosheets under solvothermal treatment for sufficient time were phase-pure orthorhombic $\alpha$-$LiFePO_4$ as confirmed by X-ray diffraction (Figure 4.2E). It should be pointed out that decreased reaction time would result in the formation of $\beta$-$LiFePO_4$, which was proved to be less electrochemically active than the α-$LiFePO_4$.[93] Raman spectroscopy and FTIR were further utilized to analyze the surface composition of the $LiFePO_4$ nanosheets as shown in Figure 4.2F. Three major bands in the Raman spectra between 1100−900 $cm^{-1}$ were attributed to intermolecular stretching motions and antisymmetric stretching modes of the $PO_4^{3-}$. The

bands between 650−550 $cm^{-1}$ and between 500−400 $cm^{-1}$ were assigned to the combined antisymmetric stretching modes of $PO_4^{3-}$.[94] The bands below 400 $cm^{-1}$ were suggested to be caused by lattice vibrations. The observed vibrational bands were in good agreement with the assignments reported in the literature,[95] suggesting the absence of impurities on the surface. The antisite defect, which is a typical defect of $LiFePO_4$ synthesized at low temperature and a barricade for lithium-ion migration,[96] was examined by FTIR spectrum. The infrared absorption bands at 947 $cm^{-1}$, which corresponds to the symmetric stretching P−O vibration peak of the $PO_4$ tetrahedron in defect-free $LiFePO_4$, implied that the antisite defect concentration was very low for thermally annealed $LiFePO_4$ nanosheets.

### 4.3.3 Electrochemical properties

#### *4.3.3.1 Lithium-ion diffusion coefficient of the $LiFePO_4$ nanosheets*

Diffusion coefficient is a key parameter to evaluate the lithium-ion transport properties of the 2D $LiFePO_4$ nanosheets.[97-100] In this chapter, we will use two different methods, i.e. EIS and CV curve methods, to characterize the lithium-ion diffusion coefficient. The conductivity of the $LiFePO_4$ nanosheets coated with a few nanometer thick carbon layer is revealed by an electrochemical impedance spectrum and cyclic voltammetry. To demonstrate the hypothesis that better electrochemical performance could be achieved by using the highly {010}-oriented $LiFePO_4$ nanosheets, commercial $LiFePO_4$/C powders with irregular shape were used as a reference. The electrodes made from $LiFePO_4$ nanosheets showed higher electronic conductivity and lower charge-transfer resistance compared with those of commercial $LiFePO_4$/C powders as revealed by the Nyquist plots (**Figure 4.3**). With the simplified-contact-Randles equivalent

circuit,[101] the electronic conductivity and total resistance of the electrode made from $LiFePO_4$ nanosheets were fitted to be 1.8 $S \cdot cm^{-2}$ and 66.5$\Omega \cdot cm^{-2}$, superior to 0.4 $S \cdot cm^{-2}$ and 74.4 $\Omega \cdot cm^{-2}$ of the electrode made from commercial $LiFePO_4$/C powders. The lithium-ion diffusion coefficient can be calculated from the Nyquist plots based on the following equations:

$$D = R^2T^2 / 2A^2n^4F^4C^2\sigma^2$$

$$Z_{\mathrm{Re}} = K + \sigma\omega^{-1/2}$$

where $D$ is the diffusion coefficient ($cm^2\ s^{-1}$), $R$ is the gas constant (8.31 J $mol^{-1}\ K^{-1}$), $T$ is the absolute temperature (298 K), $A$ is the surface area of the cathode, $n$ is the number of electrons transferred in the half-reaction for the redox couple (for $LiFePO_4$, $n$=1), $F$ is the Faraday constant (96485 C $mol^{-1}$), $C$ is the is the molar concentration of Li ions in $LiFePO_4$ (2.28 × $10^{-2}$ mol $cm^{-3}$), $K$ is a constant, $\omega$ is frequency, and $\sigma$ is the Warburg factor which corresponds to the slope of the curve shown in **Figure 4.4**A.

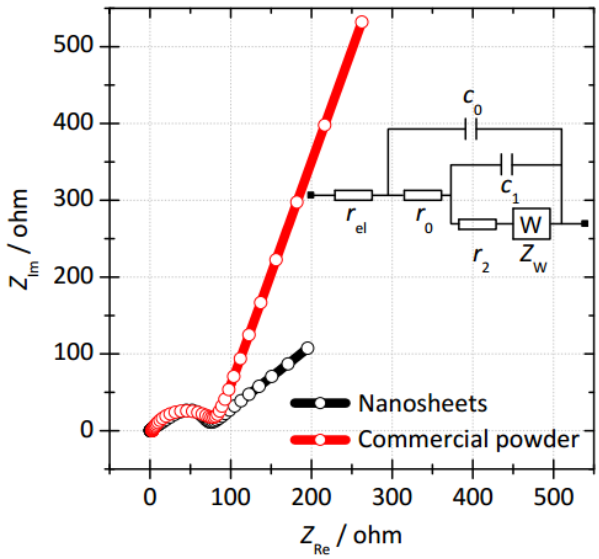


**Figure 4.3. Nyquist plots of $LiFePO_4$ nanosheets/Li metal (black) and commercial $LiFePO_4$/Li metal (red) half-cells measured in the frequency region of $10^6$–0.01 Hz.**

The lithium-ion diffusion coefficient at open circuit was calculated to be ~6.2 × $10^{-13}$ $cm^2$ $s^{-1}$ for the $LiFePO_4$ nanosheets, compared to ~8.3 × $10^{-14}$ $cm^2$ $s^{-1}$ for the commercial $LiFePO_4$/C powders according to the slopes of the real part of the complex impedance versus the square root of frequency, $\omega^{-1/2}$. Cyclic voltammetry profiles at a fixed scan rate of 0.1 mV $s^{-1}$ revealed that the potential interval between the anodic and cathodic peaks of $LiFePO_4$ nanosheets was ~180 mV, much lower than ~340 mV for commercial powders (Figure 4.4B). Moreover, the redox peak profile of $LiFePO_4$ nanosheets was more symmetric and sharper than that of commercial $LiFePO_4$/C powders, demonstrating that the redox kinetics was enhanced due to the improvement of conductivity and the reduced diffusion length along the [010] direction. The lithium-ion diffusion coefficient of $LiFePO_4$ nanosheets during charge/discharge process was further revealed by cyclic voltammetry profiles at different scanning rates (Figure 4.4C). The peak current is in linear response to the square root of scanning rate ($v$) as shown in Figure 4.4D, from which the average lithium-ion diffusion coefficient of the $LiFePO_4$ nanosheets could be estimated to be ~6.8×$10^{-14}$ and ~2.8 ×$10^{-14}$ $cm^2$ $s^{-1}$ during the charge and discharge processes, respectively, according to the following equation.

$$I_{pc} = 2.69 \times 10^5 n^{3/2} A D^{1/2} C \upsilon^{1/2}$$

where $I_{pc}$ is the peak current (A), n is the number of electrons in the charge-transfer step (for $LiFePO_4$, n=1), $A$ is the total surface area of the electroactive material calculated from the mass loading of $LiFePO_4$ nanosheets and their corresponding specific surface area ($cm^2$), $D$ is the lithium ion diffusion coefficient in $LiFePO_4$ at 298 K ($cm^2$ $s^{-1}$), $C$ is the molar concentration of Li ions in $LiFePO_4$ (2.28 × $10^{-2}$ mol $cm^{-3}$), and $v$ is the scan rate (V $s^{-1}$).

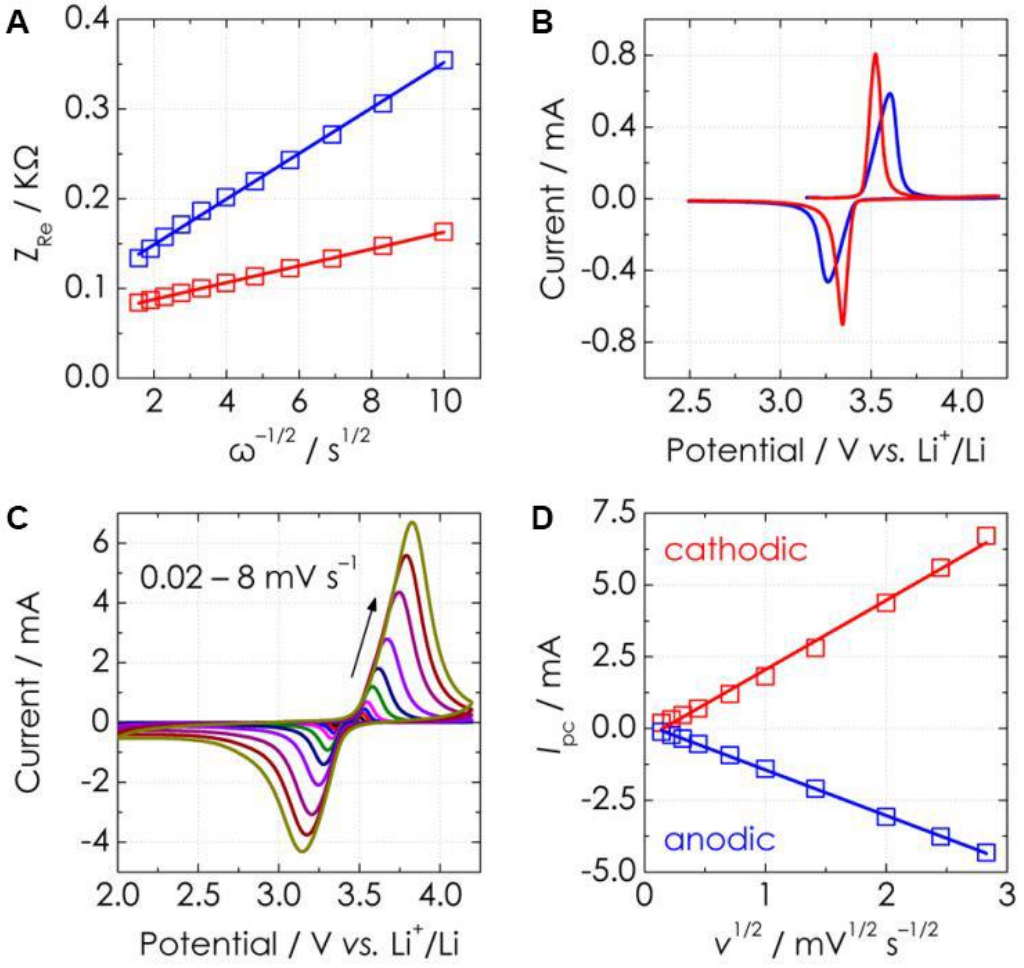


**Figure 4.4. Electrochemical characterization of the $LiFePO_4$ nanosheets.** (A) The real part of the complex impedance versus $\omega^{-1/2}$ at open circuit voltage for $LiFePO_4$ nanosheets (red) and commercial $LiFePO_4$/C (blue). (B) Cyclic voltammetric profiles of $LiFePO_4$ nanosheets (red) and commercial $LiFePO_4$/C powders (blue) at a fixed scan rate of 0.1 mV $s^{-1}$. (C) CV profiles of $LiFePO_4$ nanosheets at various scan rates of 0.02, 0.05, 0.1, 0.2, 0.5, 1, 2, 4, 6, and 8 mV $s^{-1}$. (D) Linear response of the peak current ($I_{pc}$) as a function of the square root of scanning rate (ν).

### *4.3.3.2 Electrochemical performance of the $LiFePO_4$ nanosheets*

The highly oriented {010} surface and low antisite defect concentration may contribute to the high capacity at high current densities. **Figures 4.5**A and B show the rate capability of the carbon-coated $LiFePO_4$ nanosheet electrode and commercial

$LiFePO_4$/C powder electrode, respectively. At low or moderate current densities, both electrodes showed comparable reversible capacities, for example, ca. 151 and 140 mAh $g^{-1}$ for $LiFePO_4$ nanosheets and ca. 147 and 134 mAh $g^{-1}$ for $LiFePO_4$/C powders at C-rate of 0.5 and 1, respectively. When the C-rate increased to higher than 5 C, the difference in rate capability between two electrodes became distinctly obvious. The $LiFePO_4$ nanosheets presented a high discharge capacity of ca. 120, 85, and 72 mAh $g^{-1}$ at the C-rate of 5, 10, and 20, respectively, while $LiFePO_4$/C powders only present ca. 85, 58, and 40 mAh $g^{-1}$ at the corresponding C-rates. The $LiFePO_4$ nanosheets even showed a capacity of 55 mAh $g^{-1}$ at the C-rate of 30, but the commercial $LiFePO_4$/C powders were barely rechargeable at this current rate. Noticeably, more stable potential plateau during the charge/discharge process for the $LiFePO_4$ nanosheet electrodes (**Figure 4.6**) indicated less pseudocapacitive contribution from surface/interfacial lithium storage.[102] The pseudocapacitive effect, which means the charge storage of lithium-ion from faradaic processes occurring at the electrode/electrolyte interface, has to be considered when materials approach the nanoscale dimensions. In fact, both capacitive behavior and lithium intercalation processes contribute to the total storage of charge with different storage mechanisms.[103] The $LiFePO_4$ nanosheet electrodes showed less contribution from the pseudocapacitive effect but higher specific capacity over the $LiFePO_4$/C powder electrodes, suggesting considerably enhanced lithium-ion insertion/extraction efficiency inside the nanosheets. This result is consistent with the hypothesis that particles with higher exposed {010} facet percentage could facilitate the extraction/insertion of lithium-ion, thus leading to an enhanced rate capability. The average reversible capacity of $LiFePO_4$ nanosheets reached 90 mAh $g^{-1}$ at a current rate of 10 C and was sustained for 1000 cycles with no obvious capacity fading as summarized in Figure 4.5C. The corresponding Coulombic efficiency was approaching ~100% after the first few cycles.

The performance of the $LiFePO_4$ nanosheets is superior to that of commercial $LiFePO_4$/C powders, in which an average reversible capacity of ca. 70 mAh $g^{-1}$ was sustained with capacity retention of 84% at current rate of 5 C over 500 cycles (Figure 4.5D). These results are exceeding/comparable to previously reported nanoplate-like $LiFePO_4$ obtained via hydro/solvothermal method and $LiFePO_4$ materials obtained via other methods.[104-106]

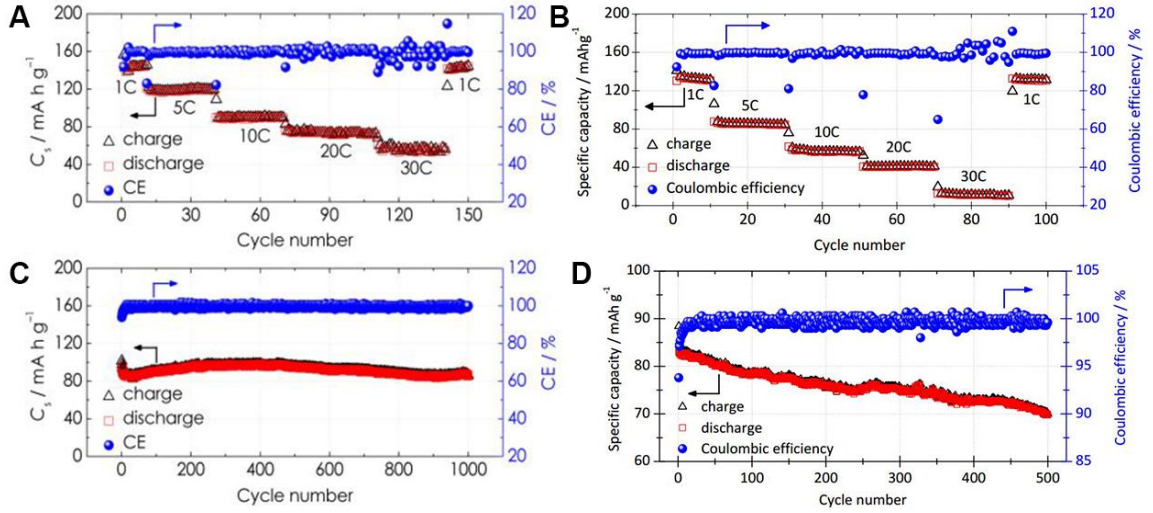


**Figure 4.5. Electrochemical performance of the $LiFePO_4$ electrodes.** (A) Rate capability of the $LiFePO_4$ nanosheets at the C-rate ranging from 1−30 C. (B) Rate capability of the commercial $LiFePO_4$ powders at the C-rate ranging from 1−30 C. (C) Cycling stability of $LiFePO_4$ nanosheets at 10 C rate for 1000 cycles. (C) Cycling stability of commercial $LiFePO_4$ powders at 10 C rate for 1000 cycles.

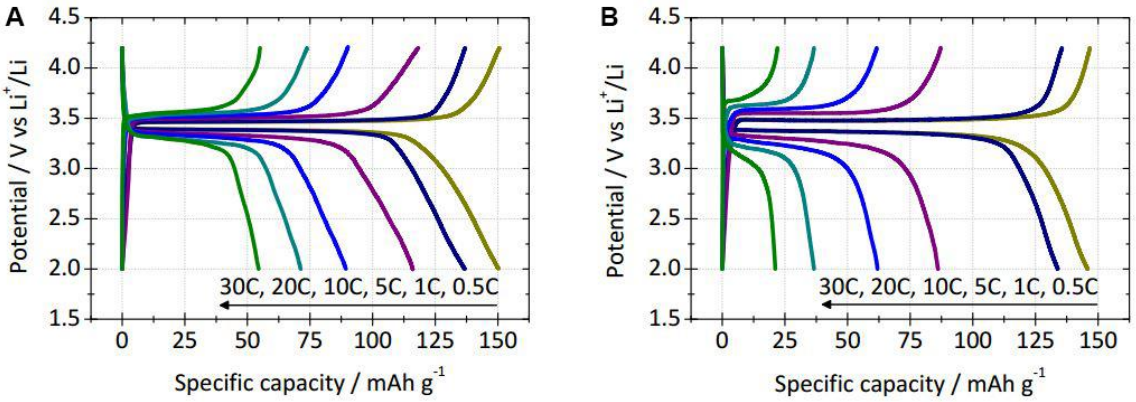


**Figure 4.6. Typical charge/discharge profiles of the $LiFePO_4$ electrodes at current rate ranging from 0.2−30 C.** (A) $LiFePO_4$ nanosheets. (B) commercial $LiFePO_4$/C powders.

### *4.3.3.3 Investigation of $LiFePO_4$ nanosheets for all 2D nanosheets based lithium-ion full batteries*

2D nanostructured materials, though only measured in a half-cell configuration so far, have been found to possess high rate capability and capacity for lithium storage. It is important to further exploit these materials into full battery in terms of the practical application as energy storage devices. Therefore, we combined the 2D $ZnMn_2O_4$/graphene anode and $LiFePO_4$ nanosheet cathode in a full cell, as a representative example, for better understandings of 2D nanomaterials based full cells (**Figure 4.7**). To demonstrate the hypothesis that the 2D nanostructured electrodes could lead to enhanced charge and discharge rate, a control full battery using conventional graphite anode and commercial $LiFePO_4$ powder cathode is also fabricated via the same steps.

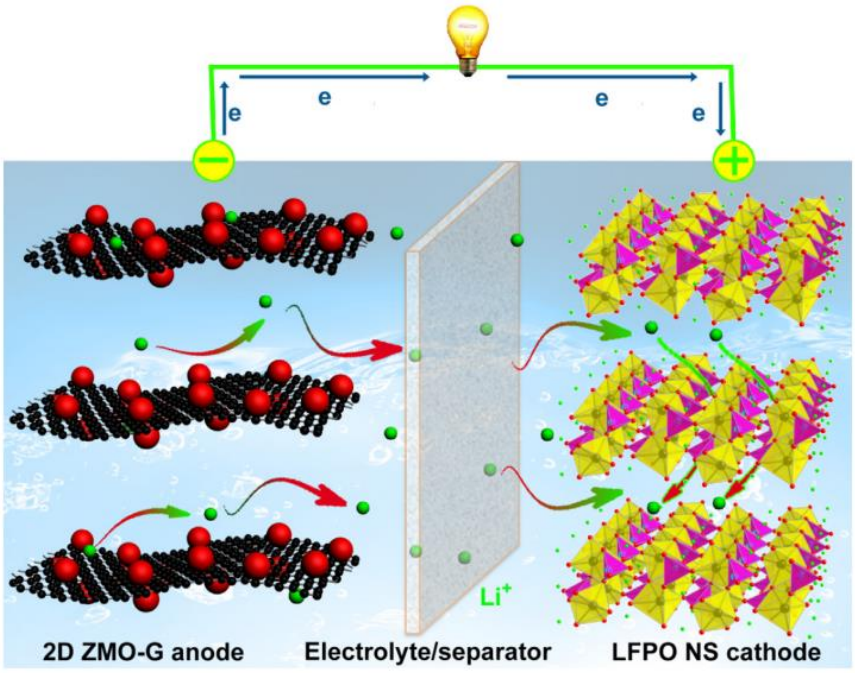


**Figure 4.7. Schematic of all-nanosheet-based Li-ion full battery using 2D $ZnMn_2O_4$/graphene hybrid nanosheet and $LiFePO_4$ nanosheet as anode and cathode, respectively.**

The all-nanosheet-based full battery was first charged and discharged at a rate of 0.2 C (1 C=150 mA $g^{-1}$) between 3.9 and 0.9 V for several cycles. The initial charge and discharge capacities are ca. 138 and ca. 132 mAh $g^{-1}$, respectively, resulting in an initial coulombic efficiency of ~96% (**Figure 4.8**A). It should be noted that the pre-lithiation is a necessary step in our studies to improve the coulombic efficiency of the full battery. A reversible capacity of ca. 124 mAh $g^{-1}$ was obtained after 100 charge/discharge cycles, corresponding to ~94% capacity retention. The corresponding coulombic efficiency was approaching ca. 100% after the first few cycles. In contrast, at the same rate, the control full battery showed gradually decreased specific capacity from ca.125 to ca.73 mAh $g^{-1}$ during the 100 cycles.

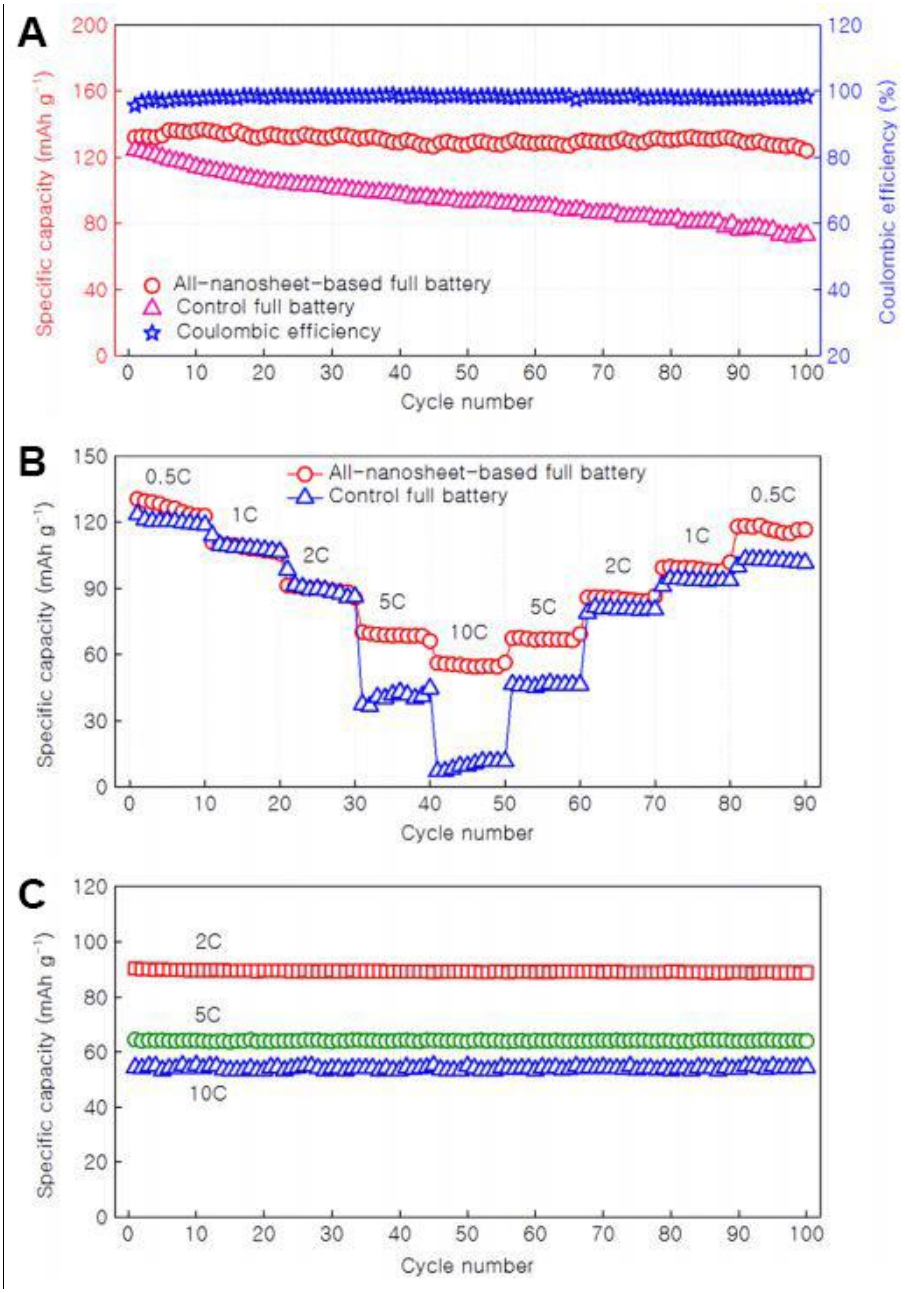


**Figure 4.8. Electrochemical performance of the $ZnMn_2O_4$-$LiFePO_4$ lithium-ion full battery.** (A) Cycling performances of all-nanosheet-based full battery and control full battery together at 0.2 C for 100 cycles. (B) Comparison of rate capabilities of all-nanosheet-based full battery and control full battery. (C) Cycling performances of all-nanosheet-based full battery at 2 C, 5 C and 10 C for 100 cycles, respectively.

Further, the rate capability of all-nanosheet-based full battery was characterized. Figure 4.8B shows the specific capacities of all-nanosheet-based full battery and control full battery at various current densities. At low rates, these two batteries showed comparable capacities, for example, ca. 122, 109 and 90 mAh $g^{-1}$ for all-nanosheet-based full battery and ca.120, 108 and 90 mAh $g^{-1}$ for control full battery at 0.5 C, 1 C, and 2 C, respectively. When the current density increased, the superiority of our all-nanosheet based full battery became obvious. A reversible capacity of ca. 69 mAh $g^{-1}$ was obtained for all-nanosheet-based full battery at 5 C, while the control full battery only presented ca. 44 mAh $g^{-1}$ at the same rate. Noticeably, the all-nanosheet-based full battery can be operated at a 10 C rate with a capacity of ca. 58 mAh $g^{-1}$, ca. 48% of the capacity at a 0.5 C rate, but the control full battery was barely rechargeable at this current density. The high cycling stability of the all-nanosheet-based full battery was further investigated at high current density. Figure 4.8C shows cycling performances of the all-nanosheet-based battery at 2 C, 5 C, and 10 C. No obvious capacity decay was observed at all current densities after 100 cycles, further demonstrating the high electrochemical stability of this all-nanosheet-based full battery. The as-fabricated all-nanosheet-based full battery presented comparable and superior power capability to recently reported all-nanostructure-based full batteries. An energy density of ca. 231 Wh $kg^{-1}$ was obtained at a low rate, higher than that of the conventional Li-ion battery. It also exhibited a power density of ca. 1060 W $kg^{-1}$ at a high rate, comparable to that of electrochemical capacitors. It should also be noted that such a high-rate and long-life all-nanosheet-based full battery is comparable/superior to most full batteries reported to date.[107-110]

## 4.4 CONCLUSIONS

In conclusion, single-crystalline $LiFePO_4$ nanosheets nanosheets have been successfully obtained via the bottom-up method. The as-synthesized nanosheets provide large effective surfaces for ion transport and storage. This feature results in battery electrodes offering high volumetric energy density, impressive rate capability, and excellent cycling stability. Our experimental results have identified the superior electrochemical performance of the 2D nanomaterials, no matter in half-cell configuration or full battery devices. Our study provides a direction on developing electrode materials of electrochemical energy devices with high-rate capability for alkali-ion storage.

# Chapter 5: Interlayer engineering of ultrathin 2D nanosheets for superior sodium-ion storage*

## 5.1 INTRODUCTION

Sodium-ion batteries (SIBs) are of great interest as a potentially low-cost and safe alternative to the prevailing lithium-ion battery technology owing to the high abundance of sodium in earth crust, even distribution in nature and its favorable redox potential (only ≈0.3 V above that of lithium).[111-114] Figures of merit for future SIBs call for a breakthrough in energy (>200 Wh $kg^{-1}$) and power density (>2000 W $kg^{-1}$) as well as the cycle life (>4000 cycles) by designing new electrode structures, materials engineering and identifying new chemistries, to satisfy the requirements of many potential applications ranging from ubiquitous portable electronics to grid energy storage.[14, 115, 116] 2D energy materials especially those that undergo ion insertion/extraction reaction have shown promising electrochemical performance especially excellent rate capability and cycling stability for alkali ion storage.[117, 118] 2D vanadyl phosphate ($VOPO_4$) nanosheets have long been recognized as promising cathode materials for electrochemical energy storage, such as pseudocapacitors, lithium and sodium-ion batteries, due to the rich redox reactions, high theoretical capacity, high redox reaction potential as well as unique structural features.[92, 119] When one sodium-ion is considered to take part in the insertion/extraction process, 2D $VOPO_4$ nanosheets output a flat voltage plateau at ~3.5 V vs $Na/Na^+$ for $V^{4+}/V^{5+}$ redox couple and a high theoretical capacity of 166 mAh $g^{-1}$. Recently, Manthiram and co-workers prepared the $VOPO_4$ layered structures by chemical

* L. Peng, Y. Zhu, X. Peng, Z. Fang, W. Chu, Y. Wang, Y. Li, Y. Xie, J. J. Cha, G. Yu, "Interlayer Engineering of $VOPO_4$ Ultrathin Nanosheets via Organic Molecule Intercalation for Superior Sodium-ion Transport Properties" under review.
L. Peng carried out the experiments, analyzed the results, and wrote the paper. G. Yu supervised the project. All participated in the preparation of the project.

delithiation of the tetragonal $\alpha_I$-$LiVOPO_4$ at room temperature.[75] In sodium-ion cells, the $VOPO_4$ cathodes delivered a reversible capacity of 110 mAh $g^{-1}$, most of which are contributed by a long plateau at 3.4~3.5 V. 2D $VOPO_4$ nanosheets also show advantageous structural features for energy storage. For instance, 2D ultrathin $VOPO_4$ nanosheets possess open 2D ion transport channels and short ion diffusion distances, which enable fast ion transport. Yu and co-workers reported a highly reversible pseudocapacitance intercalation of sodium-ion in the ultrathin $VOPO_4$ nanosheets synthesized by isopropanol exfoliation.[120] The ultrathin $VOPO_4$ exhibited superior rate capability and cycling stability for lithium-ion storage and decent electrochemical performance for sodium-ion storage. The promising performance are attributed to the pseudocapacitance intercalation occurred in the ultrathin nanosheet structures. Another intriguing aspect of 2D $VOPO_4$ nanosheets is that the interlayer spacing can often be readily controlled (e.g., by intercalating different species such as polymers and/or polyelectrolytes), which may improve the insertion/extraction of ions and make the electrode more tolerant to cycling-induced volume changes.[121, 122]

Meanwhile, a general concern about 2D energy materials has been raised recently. While 2D open framework materials have proven effective in constructing kinetically favorable sodium-ion channels, the irreversible restacking of the individual 2D nanosheets during materials processing or device fabrication may lead to the decrease of active surfaces for sodium-ion storage and the sluggish sodium-ion transport.[17] To address this issue, one promising strategy to accommodate sodium-ions is to increase the interlayer spacing to facilitate sodium-ion transport by creating a lower energy barrier for sodium-ion transport through the interlayer space. Interlayer-expansion method has been reported in 2D $MoS_2$ nanosheets to improve the sodium and magnesium ion transport. Yao and co-workers reported interlayer expansion in 2D $MoS_2$ nanosheets via an

exfoliation-restacking method using poly(ethylene oxide) (PEO) as intercalants.[123, 124] The interlayer spacing of $MoS_2$ can be tuned from 0.615 nm to 1.45 nm by insertion of controlled amounts of PEO. The materials with different interlayer spacings exhibited different Na/Mg diffusivities and thus different electrochemical performances for sodium and magnesium ion storage. The critical steps of this interlayer expansion method are the synthesis of good single-layered $MoS_2$ dispersion and the proper restacking process between $MoS_2$ dispersion and PEO solution. Otherwise, the uniformity of PEO intercalated in $MoS_2$ layer is not good enough to ensure the improved electrochemical performance. Layered $VOPO_4$ materials have been extensively explored as host materials for various organic molecule intercalations, such as alcohols, ethers, aldehydes, carboxylic acids, amines and heterocyclic N- and S-donors. Many reports and review papers about the intercalation, in terms of the intercalation mechanism, species of intercalants and the possible bonding between the intercalants and the host, have been reported in the past decades.[125] But none of these studied the electrochemical characteristics of the intercalated $VOPO_4$. The intercalated $VOPO_4$ materials show controllable interlayer distances, which are anticipated to show potential for large cations storage, such as $Na^+$, $Ca^{2+}$, $Mg^{2+}$ and even $Al^{3+}$. Compared with the restacking of $MoS_2$ with PEO, organic molecules intercalation into $VOPO_4$ layers shows much superior feasibility and uniformity.[126]

In this chapter, we develop a general interlayer-expansion strategy to improve the sodium-ion transport in $VOPO_4$ nanosheets via organic molecules intercalation. As a proof-of-concept, triethylene glycol (TEG) and tetrahydrofuran (THF) are chosen as the intercalants to demonstrate the feasibility of this interlayer-expansion strategy and the advantageous features for superior sodium-ion transport and storage brought by this strategy. The as-obtained $VOPO_4$ nanosheets show similar 2D morphology with thin

thickness and expanded interlayer distances, as identified by the XRD patterns and the cross-sectional high-resolution transmission electron microscopy (HR-TEM). The intercalation process can be extended to various organic molecules and the interlayer distance of the $VOPO_4$ nanosheets can be easily tuned by intercalating different organic molecules, like the TEG and THF molecules adopted in the current report. We also use the XAFS, for the first time, to study the chemical bonding between the organic intercalants and the $VOPO_4$ host layers. The XAFS results show that the organic intercalants are successfully intercalated into the individual $VOPO_4$ layer. We also perform density functional theory (DFT) calculations for the diffusion behavior of sodium-ion in the pure and TEG intercalated $VOPO_4$ nanosheets. Due to the expanded interlayer spacing in combination with the decreased energy barriers for sodium-ion diffusion, the interlayer expanded $VOPO_4$ nanosheets show much improved sodium-ion transport kinetics and much improved rate capability and cycling stability for sodium-ion storage. Our results afford deeper understanding on the interlayer-expansion strategy to boost the sodium-ion storage performance of the $VOPO_4$ nanosheets. Our results may also bring a paradigm shift of the current sodium-ion storage research to the exploration of large cations storage, such as $K^+$, $Mg^{2+}$, $Ca^{2+}$ and even $Al^{3+}$.

## 5.2 EXPERIMENTAL DETAILS

### 5.2.1 Synthesis of $VOPO_4 \cdot 2H_2O$ bulk chunks

$VOPO_4 \cdot 2H_2O$ bulk chunks were synthesized according to a simple reflux method reported in the previous literature. 4.8 g of $V_2O_5$ powders (Aldrich) and 26.6 mL concentrated $H_3PO_4$ (85%, Aldrich) were dispersed in 115.4 mL of DI $H_2O$. The mixed dispersion was then refluxed at 110 °C for 16 h. Thereafter, the dispersion was permitted cool down to room temperature. The yellow-greenish precipitate was finally collected by

centrifugation and washed several times with water and acetone. The resulting sample was dried in vacuum at 60 °C for 3 h.

### 5.2.2 Intercalation processes of TEG and THF molecules into $VOPO_4$ nanosheets

The intercalation compounds were obtained by a displacement reaction. In a typical intercalation process, 100 mg $VOPO_4 \cdot 2H_2O$ bulk chunks were dispersed in 7 mL isopropanol (IPA) solvent, and then 8 mL organic intercalants, like TEG and THF, were added into the $VOPO_4$ IPA dispersion. After magnetic stirring under 110 °C for 2 days, the blue-greenish TEG-$VOPO_4$ sample and the dark-green THF-$VOPO_4$ samples were obtained. The as-obtained powders were further washed with IPA for three times, and dried in vacuum at 80 °C for overnight.

### 5.2.3 Materials characterization

The structure of the as-synthesized samples was characterized by powder X-ray diffraction (XRD) patterns performed on a Philips Miniflex diffractometer. The morphology of the samples was investigated using scanning electron microscope (SEM), scanning transmission electron microscope (STEM) (Hitachi S5500), and transmission electron microscope (TEM) (JEOL 2010F). The TG analysis was tested by a TGA/SDTA851e thermogravimetric analyzer under an air atmosphere from 25 to 850 °C at a heating rate of 10 °C $min^{-1}$.

### 5.2.4 Electrochemical measurements

The working electrodes were prepared by mixing active materials (TEG and THF intercalated $VOPO_4$ nanosheets and the pure $VOPO_4$ nanosheet control sample), sodium carboxymethyl cellulose (CMC) and superP carbon at a weight ratio of 85:10:5. Then the slurries were drop-casted onto the aluminum foil. The as-prepared electrodes were dried under vacuum at 110 °C for 10 h. The loading of active materials was ~1.0 mg $cm^{-2}$.

After being sealed, the electrodes were assembled into coin cells (CR2032) in an argon-filled glovebox using Celgard 2320 as separator, 1 mol $L^{-1}$ $NaClO_4$ in propylene carbonate (PC) with 2% fluoroethylene carbonate (FEC) added as the electrolyte and Na metal as the counter electrode. The assembled coin cells were tested on the LAND and Biologic VMP3 battery test systems with a voltage range of 2.5~4.3 V.

### 5.2.5 Energy barrier calculation details

DFT calculations were performed using Vienna *ab* Initio Simulation package (VASP) package, with ion–electron interaction treated by the projector-augmented plane wave (PAW) pseudopotentials. The Perdew−Burke−Ernzerhof (PBE) generalized gradient approximation (GGA) functional and a plane-wave cutoff energy of 400 eV were used in all computations. The convergence of energy and forces were set to $1\times10^{-5}$ eV and 0.04 eV/Å, respectively. The Brillouin zone was sampled with 3 × 3 × 4 k-points. The climbing-image nudged elastic band (CI-NEB) method was adopted to determine the minimum diffusion path of Na on the surface of $VOPO_4$. Specially, the CI-NEB simulations were calculated based on a 2 × 2 supercell (56 atoms) and 11 images (including initial and final states). For the Brillouin zone, a 3 × 3 × 1 k-points grid was adopted for the supercell. The ordinary and enlarged interlayer spacing were realized by fixed the atoms of $VOPO_4$ bilayer with specific distances. Specially, two possible diffusion pathways, namely P1 and P2, were identified for the controlled pure and TEG intercalated $VOPO_4$ nanosheets.

## 5.3 RESULTS AND DISCUSSION

### 5.3.1 Synthesis and characterizations of 2D TEG and THF intercalated $VOPO_4$ nanosheets.

The concept for the developed general synthesis of 2D TEG and THF intercalated $VOPO_4$ nanosheets is illustrated in **Figure 5.1**. The intercalation compounds were obtained by a facile displacement reaction, and the intercalation process was suitable for large-scale production. In brief, $VOPO_4 \cdot 2H_2O$ bulk chunk was first employed as the starting material for the intercalation (Figure 5.1A) and mixed with IPA and the organic intercalants, i.e. TEG and THF solvents (Figure 5.1B). The as-obtained $VOPO_4$ nanosheets with organic molecules intercalation exhibited different and controllable interlayer distances, due to the different chemical structures of the TEG and THF molecules. TEG and THF can uniformly replace the water molecules in the bulk chunk and intercalate in the layers through the hydrogen bonds formed between the intercalants and $VOPO_4$ layers (Figure 5.1D). We proposed the possible bonding structures of the TEG and THF molecules with the $VOPO_4$ layers in Figure 5.1E. TEG molecules were aligned between the $VOPO_4$ layers because the final product exhibited the large interlayer distance.

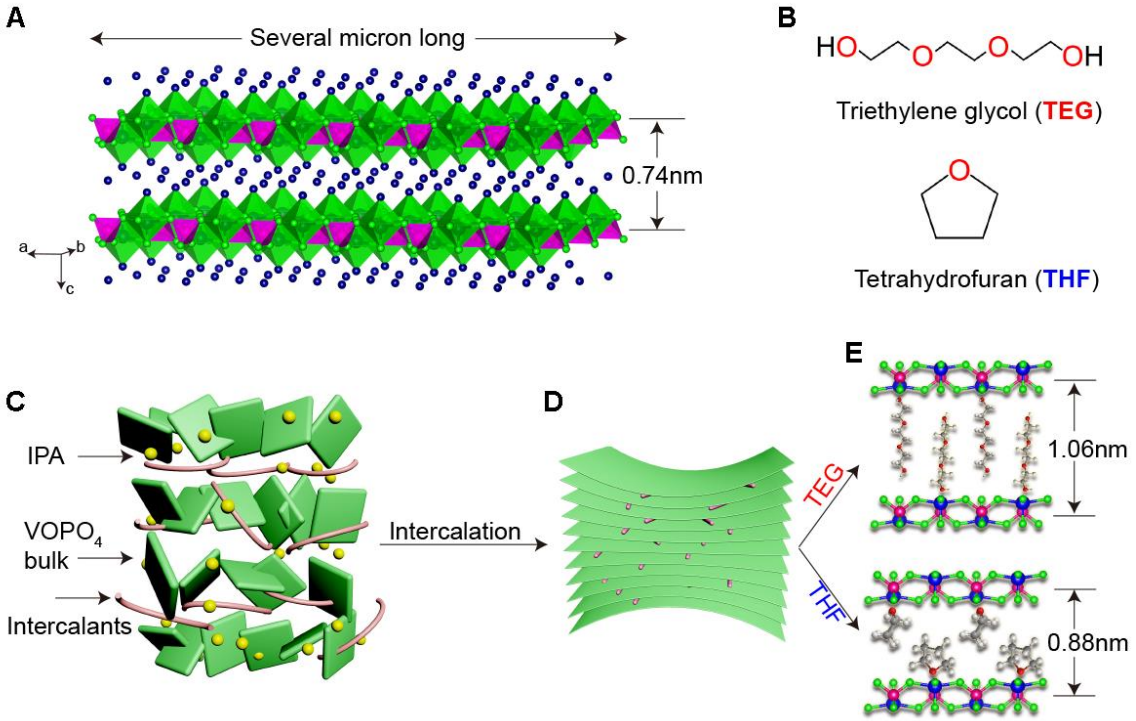


**Figure 5.1. Schematic illustration of the intercalation process of 2D $VOPO_4$ nanosheets.** (A) Crystal structure of the intrinsic $VOPO_4 2H_2O$ nanosheets, in which the sheets of $VOPO_4$ form from vertex-sharing $VO_6$ octahedra linking to phosphate $PO_4$ tetrahedra. Between each $VOPO_4$ layer, one water molecule coordinates with a vanadium atom through an oxygen atom and the other links adjacent layers together through weak hydrogen bonds (blue dots represent the water molecules). (B) Chemical structure of the TEG and THF intercalants. (C-D) Schematic illustration of intercalation process and the intercalated structure. (E) The bonding structure of the TEG and THF in $VOPO_4$ nanosheets.

The interlayer distances of TEG and THF intercalated $VOPO_4$ were studied with X-ray diffractometry (XRD) and cross-sectional HR-TEM. As shown in **Figure 5.2**A, the diffraction peaks corresponding to the interlayer spacing shift to lower angles after the intercalation of TEG and THF molecules. This shift indicates a gradually increased interlayer distance according to Bragg's formula ($d$= 0.5$\lambda$/sin($\theta$)). The interlayer distance of pristine $VOPO_4 \cdot 2H_2O$ bulk chunk is calculated to be 0.74 nm.[127] Upon intercalation of organic molecules, the spacings further increase to 0.88 nm for THF intercalated $VOPO_4$

nanosheets (THF-$VOPO_4$) and 1.06 nm for TEG intercalated $VOPO_4$ nanosheets (TEG-$VOPO_4$), corresponding to 20 and 43 % of increase, respectively. The calculated spacing values were cross-validated by HR-TEM observation, as shown in Figure 5.2B-D. Figure 5.2B showed the typical STEM image of TEG-$VOPO_4$ nanosheets with flat surface and thin thickness. Similar morphology and thickness can be obtained in the THF-$VOPO_4$ nanosheets. Focused ion beam (FIB) was used to cut the nanosheets for the cross-sectional TEM characterizations. Cross-sectional TEM of the TEG-$VOPO_4$ nanosheets in Figure 5.2C and D showed the well-defined layered structures with an interlayer distance of ~1 nm, which is consistent with the value obtained from the XRD patterns.

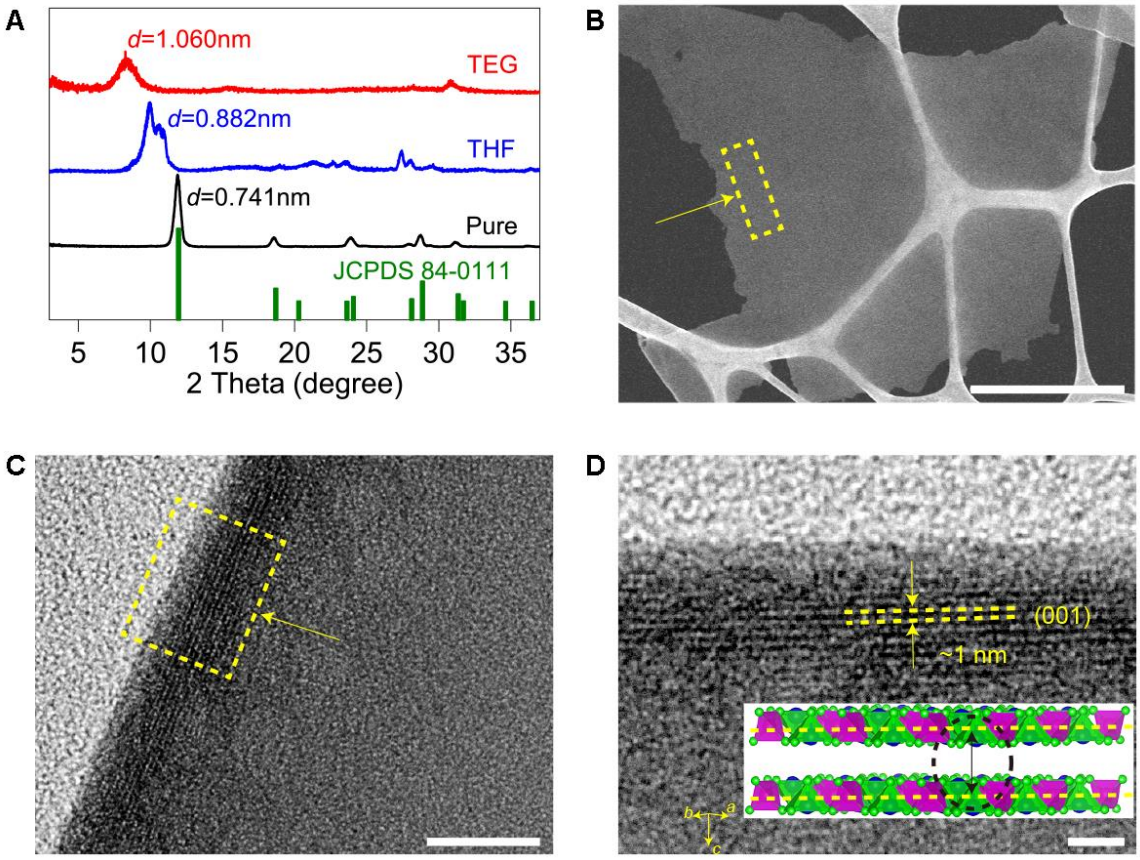


**Figure 5.2. Structural characterizations of the organic molecules intercalated $VOPO_4$ nanosheets.** (A) XRD patterns of pure $VOPO_4 \cdot 2H_2O$ bulk chunk, THF and TEG intercalated $VOPO_4$ nanosheets. (B) Typical STEM image of the TEG-$VOPO_4$ nanosheets. Scale bar: 500 nm. (C) Cross-sectional high-resolution transmission electron microscopy (HR-TEM) image of 2D TEG-$VOPO_4$ nanosheets, showing a characteristically layered structure. Scale bar: 20 nm. (D) Enlarged picture of the cross-sectional TEM, showing an interlayer distance of ~1 nm. A crystallographic model of the layered structure is also shown here, highlighting the (001) planes. The black dashed circle correlates these planes to the lattice fringes shown in the cross-sectional TEM image. Scale bar: 5 nm.

Further characterizations give insights into the chemical composition and structural properties of the interlayer expanded $VOPO_4$ nanosheets. Raman spectra shown in **Figure 5.3**A verified the structural properties of the pure $VOPO_4 \cdot 2H_2O$ bulk chunk, THF and TEG intercalated $VOPO_4$ nanosheets. The bands at 937 $cm^{-1}$ in the pure sample

curve was assigned to the symmetric O–P–O stretching modes.[54, 55] Obviously, there was a strong microstructural correlation between the symmetry of O–P–O stretching modes with the hydrogen bonding among the interlayered $H_2O$ molecules. With the intercalation of THF and TEG molecules and the breaking of hydrogen bonds from the oxygen atoms of the P–O bond in $VOPO_4$, the mitigation of the steric hindrance would facilitate the occurrence of the O–P–O stretching modes with lower energy (shifting to lower wavenumbers). However, the peaks related to the symmetric bending vibrations of O–P–O, V–O and V=O stretching mode demonstrated little shift with no obvious peak position evolution. The Raman results confirmed that the intercalated $VOPO_4$ samples are found to not contain trapped water, and the intercalated $VOPO_4$ nanosheets maintained the integrity of the in-plane layered $VOPO_4$ structure without obvious structural deformations. Thermogravimetric analyses of the pure, TEG and THF intercalated $VOPO_4$ samples reveal the weight loss (Figure 5.3B). Pure $VOPO_4$ bulk chunk showed a weight loss of 18%, indicating the loss of the two structural water molecules in the layers. The intercalated samples showed weight loss of 25% and 30% for THF and TEG intercalated $VOPO_4$ nanosheets, indicating that 0.3 THF molecule and 0.4 TEG molecule were intercalated in $VOPO_4$.

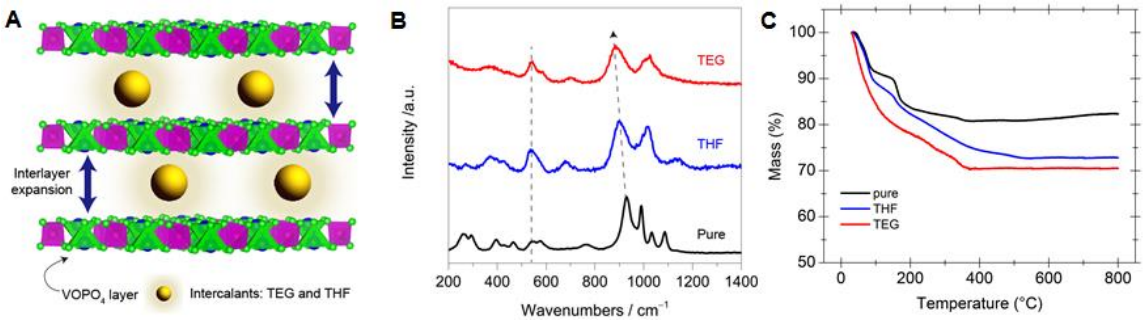


**Figure 5.3. Raman spectra and the thermogravimetric analysis of the pure $VOPO_4{\cdot}2H_2O$ bulk chunks, THF and TEF intercalated $VOPO_4$ nanosheets.**

### 5.3.2 XAFS characterizations of 2D TEG and THF intercalated $VOPO_4$ nanosheets.

To further unravel the chemical bonding/configuration between the organic intercalants and the $VOPO_4$ host layers, X-ray absorption fine structure (XAFS) tests were conducted. Considering the polarity or the dielectric property of the ligand can affect the chemical value of the center metal, synchrotron-based X-ray absorption spectroscopy (XAS), that is sensitive to the partial electronic structure and the local geometry around the selected absorber, has been used to monitor the change of the chemical configuration of the $VOPO_4$ nanosheet to determine the interaction between vanadium and the different intercalants, $H_2O$, TEG and THF (**Figure 5.4**). Figure 5.4A shows the vanadium K-edge X-ray absorption near-edge spectroscopy (XANES) of the $VOPO_4$ nanosheet intercalated with different molecules. The XANES spectra of the vanadium foil and $VO_2$ were also measured to calibrate the X-ray energy. It is easy to find the edge shifts to the lower energy with the order of $H_2O$ > TEG > THF. That means the chemical value of vanadium in the samples gradually decreases with the same order. This is also verified by the XPS results of the three samples (**Figure 5.5**). The chemical value changes of these samples also were reflected by the pre-edge feature of the XANES. The XANES of $VOPO_4{\cdot}2H_2O$ presents an obvious pre-edge peak at 5472.0 eV, labeled by *b*. Besides the peak *b*, the other pre-edge peak, labeled by *a*, appeared at 5470.5 eV for the $VOPO_4$-THF. Pre-edge peak at this position is a typical fingerprint of the $V^{4+}$ oxidation state, as shown by the pre-edge peak of $VO_2$ reference. The energy shift of 1.5 eV indicates the V oxidation state in $VOPO_4{\cdot}2H_2O$ sample is about $V^{5+}$. Higher oxidation state of the vanadium means the stronger electronegativity of the coordinated molecule for this case. We know that the electronegativity of TEG is less than that of $H_2O$ and stronger than THF. This coherence between the oxidation state of the center vanadium and the electronegativity of the ligand molecules suggests the organic

molecules TEG and THF have been successfully intercalated into the $VOPO_4$ nanosheet and coordinated into vanadium.

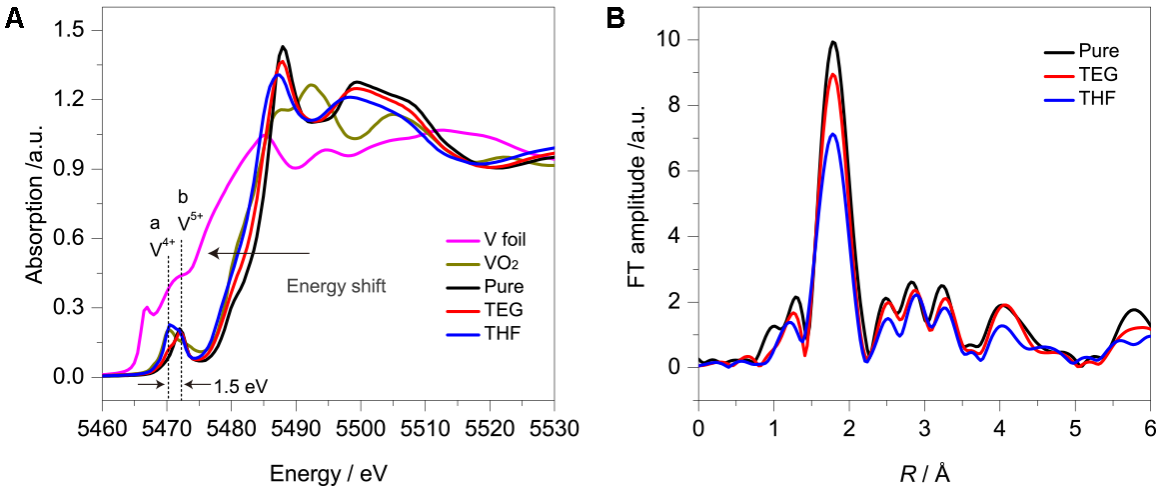


**Figure 5.4. XAFS characterizations of 2D TEG and THF intercalated $VOPO_4$ nanosheets.** (A) K-edge X-ray absorption near-edge spectroscopy (XANES) of the $VOPO_4$ nanosheet intercalated with different molecules. (B) Extended X-ray absorption fine structure (EXAFS) at vanadium K-edge of the $VOPO_4$ nanosheet intercalated with different molecules.

Extended X-ray absorption fine structure (EXAFS) at vanadium K-edge was also performed to check if any rearrangement occurs for the local atomic environment around the vanadium ion. Figure 5.4B shows the $k^3$-weighted Fourier transforms (FTs) of the EXAFS oscillations of three prepared samples. All of these FT curves present similar pair distribution functions until the distance of 6 Å, as means the integrity of the local structure around vanadium ion conserved while the organic molecules TEG and THF were intercalated into the $VOPO_4$ nanosheet layers. Though there are three types of coordinated oxygen atoms in the intercalated $VOPO_4$ nanosheet: 1) the single coordinated oxygen atom, with a short V-O bond of ~1.57 Å along the c axis (perpendicular to the layer); 2) the four-fold coordinated oxygen atoms bridged phosphorus atoms, with V-O

bond of ~1.97 Å; 3) an oxygen atom from water or organic molecules out of layers, with a large bond distance of ~2.23 Å. FT curves of these samples only show a strong peak at ~1.79 Å (no phase corrections) and show the four-fold coordinated oxygen atoms from $PO_4^{3-}$ dominates the V-O pair distribution. The position of this peak does almost not change, but its intensity gradually decreases with the order of $H_2O$ > TEG > THF. It means the average distances of V-O bonds of these samples are same, but the distortion of V-O bonds becomes larger and larger with the intercalation of TEG and THF. This trend is consistent with the change of the chemical value of vanadium ions revealed by XANES spectra discussed above. This is due to the weaker electronegativity of TEG and THF results in the larger dynamics of the coordinated oxygen atoms from the organic group.

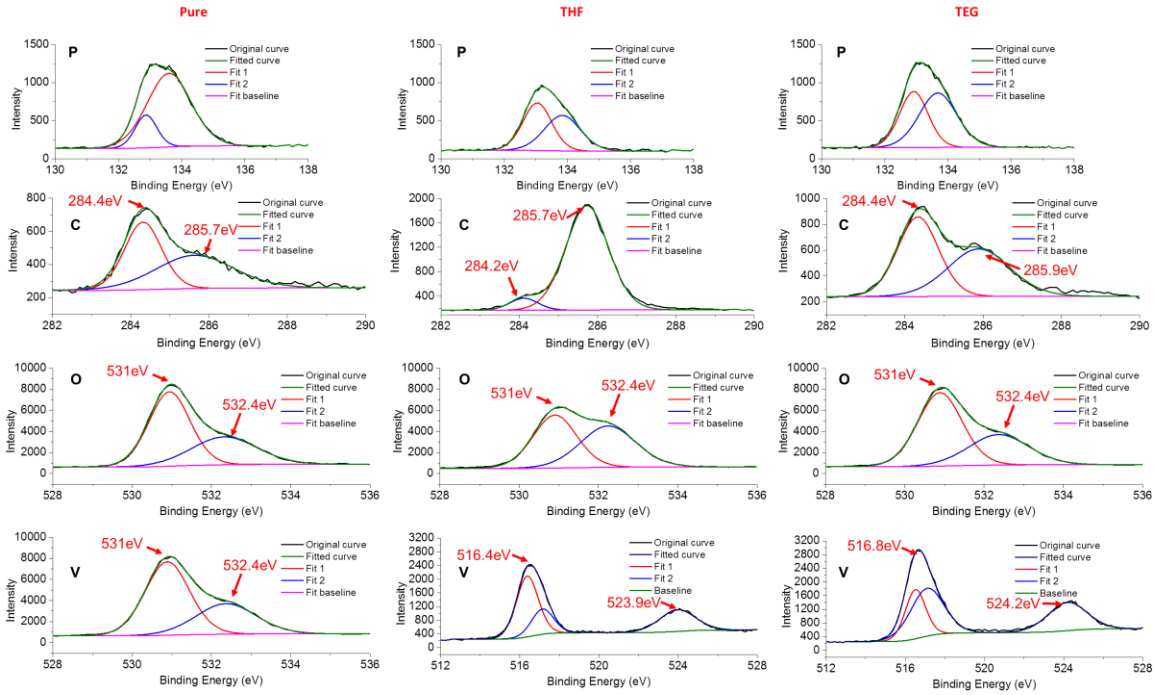


**Figure 5.5. XPS curves of the $VOPO_4 \cdot 2H_2O$ bulk chunks, THF and TEF intercalated $VOPO_4$ nanosheets.**

### 5.3.3 Electrochemical properties

#### *5.3.3.1 Sodium-ion storage properties of 2D TEG and THF intercalated $VOPO_4$ nanosheets*

To examine electrochemical properties of the 2D TEG and THF intercalated $VOPO_4$ nanosheets, CV curves, rate capability and cycling stability were conducted. **Figure 5.6**A shows the CV curves of the TEG, THF intercalated $VOPO_4$ nanosheets, and the control pure $VOPO_4$ nanosheets at the scan rate of 0.1 mV $s^{-1}$. All of the three samples exhibited two sharp redox peaks, corresponding to the sodiation/desodiation process, at the scanning range of 2.5V~4.3V. Figure 5.6B shows the rate performance of the TEG and THF intercalated $VOPO_4$ nanosheets and the pure $VOPO_4$ control sample. Three electrodes were able to deliver similar capacities of ~151, 149 and 151 mAh $g^{-1}$ at the current density of 0.1C. The capacities are similar because the major contribution to

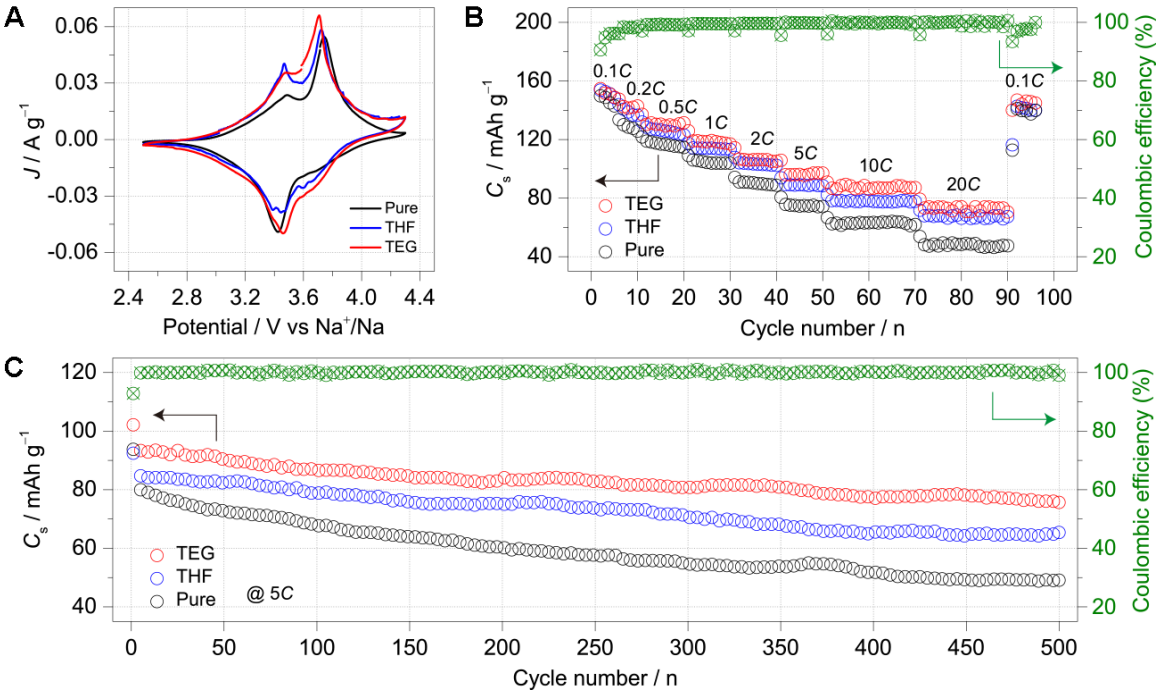


**Figure 5.6. Sodium-ion storage properties of 2D TEG and THF intercalated $VOPO_4$ nanosheets.** (A) CV curves of the TEG, THF intercalated $VOPO_4$ nanosheets, and the control pure $VOPO_4$ nanosheets at the scan rate of 0.1 mV $s^{-1}$. (B) Rate performance of the TEG, THF intercalated $VOPO_4$ nanosheets, and the control pure $VOPO_4$ nanosheets from the C rates of 0.1 C to 20 C. (C) Long-term cycling stability and Coulombic efficiency of the TEG, THF intercalated $VOPO_4$ nanosheets and the control pure $VOPO_4$ nanosheets at 5C for over 500 cycles.

the capacity is from the diffusion controlled process. As the charge/discharge rates increase, three electrodes delivered different capacities indicating the different rate capabilities. As shown Figure 5.6B, the TEG intercalated $VOPO_4$ nanosheets were able to deliver reversible capacities of 155, 143, 132, 119, 107, 100, 89 and 74 mAh $g^{-1}$ at C rate of 0.1, 0.2, 0.5, 1, 2, 5, 10 and 20, and the THF intercalated $VOPO_4$ nanosheets were able to deliver reversible capacities of 149, 140, 126, 114, 103, 89, 78 and 68 mAh $g^{-1}$ at C rate of 0.1, 0.2, 0.5, 1, 2, 5, 10 and 20. Both samples showed better rate performance than the pure $VOPO_4$ nanosheet control electrodes demonstrated in this work. The charge-discharge curves of the TEG, THF intercalated $VOPO_4$ nanosheets at various C rates

were shown in **Figure 5.7**. The reasons are attributed to the expanded interlayer distances of the TEG and THF intercalated $VOPO_4$ nanosheets, which opens up the inner surfaces for sodium-ion storage and facilitates the sodium-ion transport between the layers. In addition, Figure 5.6C shows the cycling stability of the three nanosheet electrodes. TEG intercalated $VOPO_4$ nanosheets delivered an average reversible capacity of approximately 88 mAh $g^{-1}$ at a current rate of 5 C and the capacity can be sustained for 500 cycles with no obvious capacity decay, showing a capacity retention rate of 88%. THF intercalated showed a capacity of approximately 68 mAh $g^{-1}$ at a current rate of 5 C and can be maintained for 500 cycles with a capacity retention rate of 76%. Those values were higher than those of the pure $VOPO_4$ nanosheets (51%). To be noted, the intercalated $VOPO_4$ nanosheets showed good stability in terms of the organic molecules intercalations and morphology, which were verified by the XRD patterns and morphology characterizations before and after 500 cycles test (**Figure 5.8**).

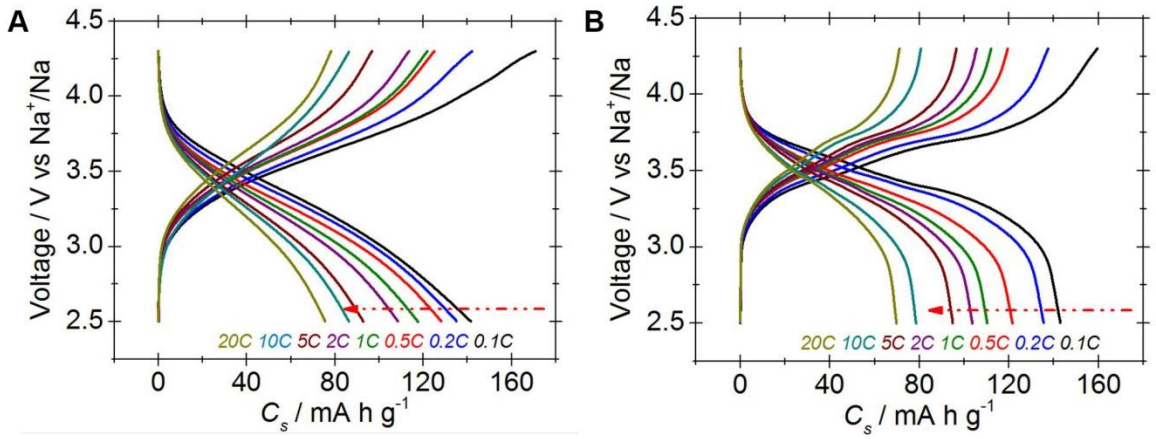


**Figure 5.7. Charge-discharge curves of the TEG (A), THF (B) intercalated $VOPO_4$ nanosheets at various C rates.**

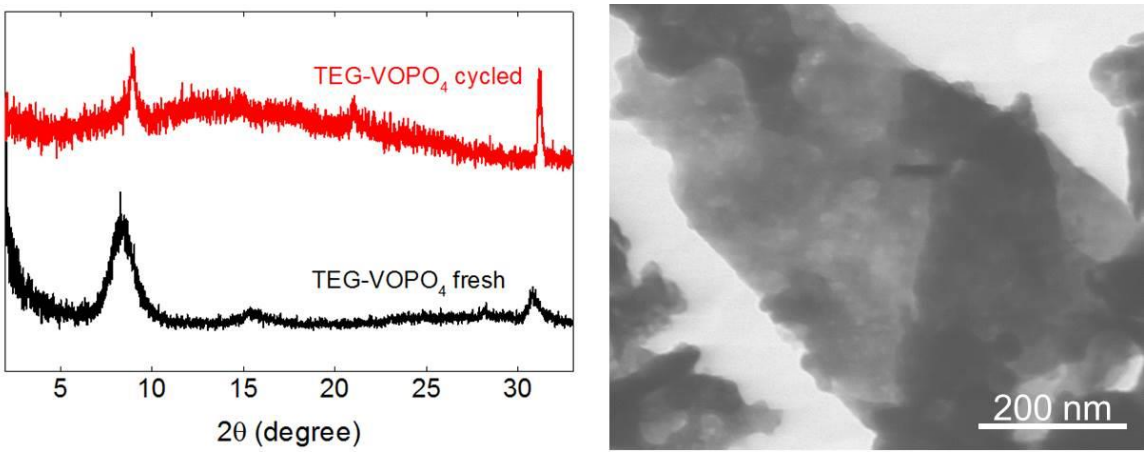


**Figure 5.8. XRD patterns and the TEM image of the TEG-intercalated $VOPO_4$ nanosheets after cycling tests.**

### *5.3.3.2 Kinetics analysis of the 2D TEG and THF intercalated $VOPO_4$ nanosheets for sodium-ion storage*

To explore the reasons for the improved electrochemical characteristics for sodium-ion storage of the TEG and THF intercalated $VOPO_4$ nanosheets, cyclic voltammetry (CV) measurements at various scanning rates were carried out to further understand the electrochemical kinetics (**Figure 5.9**). CV curves at various scan rates from 0.02 to 0.2 mV $s^{-1}$ displayed similar shapes and a gradual broadening of the peaks can be observed (Figure 5.9A). For an electrochemical energy storage device, the capacity is always contributed by the diffusion controlled and capacitive controlled processes and these two processes can be characterized by analyzing the CV data at various sweep rates according to the following equation.

$$i = a\upsilon^b$$

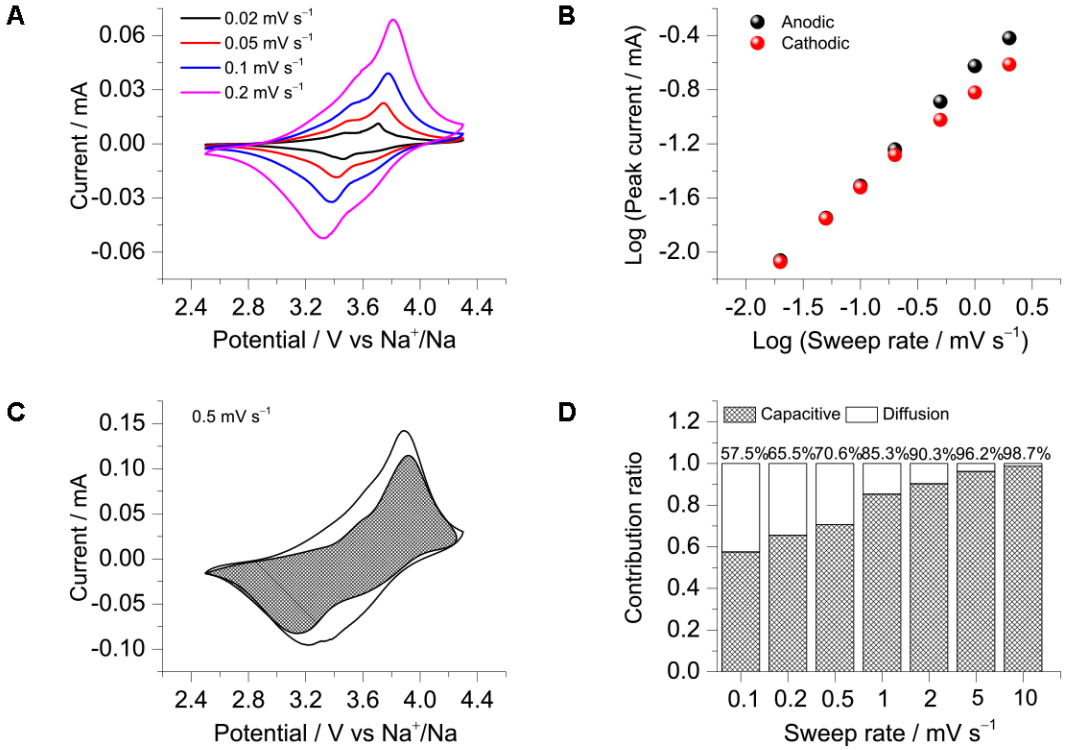


**Figure 5.9. Kinetics analysis of the 2D TEG intercalated $VOPO_4$ nanosheets for sodium-ion storage.** (A) CV curves at various scan rates from 0.02 to 0.2 mV $s^{-1}$ for TEG intercalated $VOPO_4$ nanosheets. (B) Determination of the b-value using the relationship between peak current and scan rate. (C) Separation of the capacitive and diffusion currents at a scan rate of 0.5 mV $s^{-1}$. (D) Contribution ratio of the capacitive and diffusion-controlled charge at various scan rates.

where the measured peak current *i* obeys a power law relationship with the sweep rate υ and a and b are adjustable parameters. In particular, the *b*-value of 0.5 indicates a total diffusion controlled process, whereas 1.0 represents a total capacitive process. By plotting to log *i* vs log υ, *b*-values determined as the slopes and 0.82 and 0.87 were calculated for cathodic and anodic peaks (Figure 5.9B), indicating that the majority of the current at the peak potential is capacitive. The total capacitive contribution at a certain scan rate could be quantified by separating the specific contribution from the capacitive and diffusion-controlled process at a particular voltage according to

$$i(V) = k_1\upsilon + k_2\upsilon^{1/2}$$

where $k_1$ and $k_2$ are constants for a given potential. By plotting $i(V)/\upsilon^{1/2}$ versus $\upsilon^{1/2}$, $k_1$ is determined as the slope, therefore capacitive and diffusion contributions can be obtained. For example, at scan rate 0.5 mV $s^{-1}$ (Figure 5.9C), ~70.6% of the total current, namely the capacity, is capacitive in nature. Similarly, contribution ratios between the two different processes at other scan rates were calculated (Figure 5.9D). The quantified results showed that the capacitive contribution gradually improves with the scan rate increasing. For instance, a significantly high contribution (~57.5%) of the capacity is from the capacitive process at the low scan rate of 0.1 mV $s^{-1}$. When scan rate increasing to 10 mV $s^{-1}$, the contribution increases to 98.7%. The electrochemical kinetic study for THF-intercalated $VOPO_4$ nanosheets are shown in Figure 5.10. The *b*-values for the cathodic and anodic peaks in THF-intercalated $VOPO_4$ nanosheet electrodes were calculated to be 0.73 and 0.79, respectively. At the scan rate of 0.1 mV $s^{-1}$, ~52.7% of the total capacity is capacitive in nature. The capacitive contribution increases to 96.3% as the scan rate improve to 10 mV $s^{-1}$. The capacity contribution ratios at various scan rates were also showed in **Figure 5.10**. Both the calculated *b*-value and capacitive contribution clearly demonstrate the unique characteristic behavior as a result of intercalation pseudocapacitance (**Table 5.1**). This unique storage behavior verifies the reasons for the improved rate capability and cycling stability in TEG and THF intercalated $VOPO_4$ nanosheets.

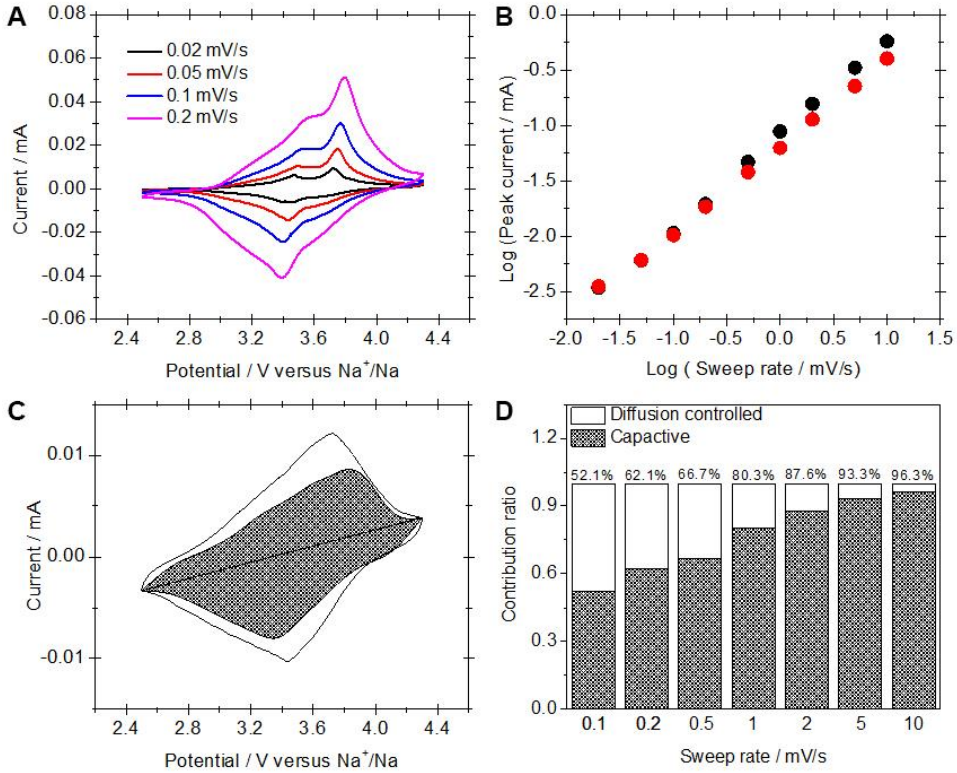


**Figure 5.10. Kinetics analysis of the 2D THF intercalated $VOPO_4$ nanosheets for sodium-ion storage.** (A) CV curves at various scan rates from 0.02 to 0.2 mV $s^{-1}$ for THF intercalated $VOPO_4$ nanosheets. (B) Determination of the *b*-value using the relationship between peak current and scan rate. (C) Separation of the capacitive and diffusion currents at a scan rate of 0.5 mV $s^{-1}$. (D) Contribution ratio of the capacitive and diffusion-controlled charge at various scan rates.

| | CV scan range (mV/s) | *b*-value cathodic/anodic | Capacitive contribution at 0.1 mV/s | Capacitive contribution at 5 mV/s | Polarization at 0.02 mV/s (mV) |
|---|---|---|---|---|---|
| TEG | 0.02~10 | 0.82/0.87 | 57.5% | 96.2% | 244 |
| THF | 0.02~10 | 0.73/0.79 | 52.1% | 93.3% | 270 |
| Pure | 0.02~20 | 0.68/0.71 | 43.5% | 91.5% | 340 |

**Table 5.1. Summary of the kinetics parameters of the 2D TEG, THF intercalated $VOPO_4$ nanosheets and the pure $VOPO_4$ nanosheets for sodium-ion storage.**

#### *5.3.3.3 Energy barriers for sodium-ion transport in the pure $VOPO_4$ nanosheets, and TEG intercalated $VOPO_4$ nanosheets*

To validate our material design and gain a fundamental insight into the intercalation effect on the enhanced rate and cycling performance, we then performed density functional theory (DFT) calculations for the diffusion behavior of sodium-ion in the pure and TEG intercalated $VOPO_4$ nanosheets. Computationally, the mobility of sodium-ion in $VOPO_4$ nanosheets can be deduced from the migration barriers. Thus, sodium-ion migration simulations based on the TEG intercalated $VOPO_4$ and the control pure $VOPO_4$ nanosheets were carried out using the climbing-image nudged elastic band (CI-NEB) method as implemented in VASP software.[128, 129] Note that two possible diffusion pathways (P1 and P2) were identified for the diffusion of sodium-ion in $VOPO_4$ nanosheets (**Figure 5.11**). Figure 5.11A shows the minimum migration pathways of the pure and TEG intercalated $VOPO_4$ nanosheets. According to our calculations, the pure

$VOPO_4$ nanosheets prefer the P1 pathway for sodium-ion migration, whereas the TEG intercalated $VOPO_4$ nanosheets with enlarged interlayer distance is in favor of P2. Specially, compared with the pure $VOPO_4$ nanosheets ($E_{ba}$ = ~0.72 eV), sodium-ion diffusion over TEG intercalated $VOPO_4$ nanosheets with enlarged interlayer spacing exhibits a much lower $E_{ba}$ of ~0.22 eV (Figure 5.11B). Since the diffusion energy barrier describes the minimum energy which must be available for the sodium-ion diffusion in the $VOPO_4$ layers, the values of the energy barriers are closely related to the difficulty of the sodium-ion transport. Therefore the increased interlayer distances should be the essential reasons for the enhanced electrochemical performance in the intercalated $VOPO_4$ nanosheets. These simulations not only provide theoretical evidence for the much improved rate capability and cycling stability in the TEG and THF intercalated $VOPO_4$ nanosheets but also strongly suggest that interlayer-expansion strategy is a powerful technique to improve the diffusion kinetics of large cations (such as $Na^+$) in layer-structured hosts.

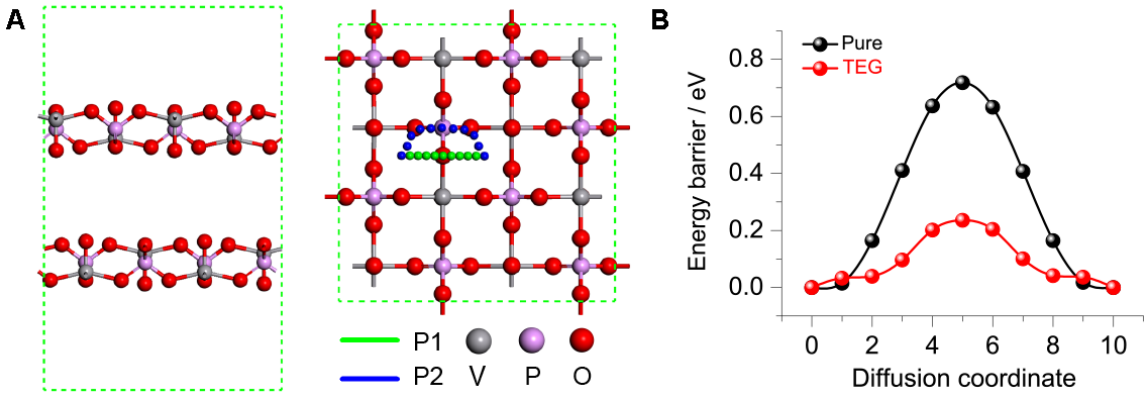


**Figure 5.11. Diffusion barrier profiles of sodium-ion transport in pure $VOPO_4$, and TEG intercalated $VOPO_4$ nanosheets.** (A) Views of geometric structures of $VOPO_4$ nanosheets (left) and sodium-ion diffusion pathways (right). (B) Diffusion barrier (minimum energy path) profiles of sodium-ion transport in pure $VOPO_4$ nanosheets, and the TEG intercalated $VOPO_4$ nanosheets.

## 5.4 CONCLUSIONS

The most significant result of this work is the demonstration of interlayer expanded $VOPO_4$ nanosheets with excellent sodium-ion transport and storage characteristics achieved by a general strategy of organic molecules intercalation. The general synthesis of the organic intercalated $VOPO_4$ nanosheets can be extended to many other organic molecules, such as TEG, THF, Amine, Alcohols. The intercalated $VOPO_4$ nanosheets show controlled and expanded interlayer distance due to the different structures of the organic molecular intercalants. As a proof-of-concept, triethylene glycol (TEG) and tetrahydrofuran (THF) are chosen as the intercalants to demonstrate the feasibility of this interlayer-expansion strategy and the advantageous features for superior sodium-ion transport and storage brought by this strategy. The TEG and THF intercalated $VOPO_4$ nanosheets exhibit expanded interlayer distance with 1.06 nm and 0.88 nm, respectively. We use the XAFS, for the first time, to study the chemical bonding between the organic intercalants and the $VOPO_4$ host layers. The XAFS results show that the organic intercalants are successfully intercalated into the individual $VOPO_4$ layer. Due to the expanded interlayer spacing in combination with the uniform intercalation of intercalants in $VOPO_4$, the interlayer expanded $VOPO_4$ nanosheets show much improved sodium-ion transport kinetics and much improved rate capability and cycling stability for sodium-ion storage, compared with the pure $VOPO_4$ nanosheets without organic molecules intercalation. We also perform DFT calculation of the energy barriers for sodium-ion transport in 2D pure and TEG intercalated $VOPO_4$ nanosheets. The results demonstrate that the energy barrier of sodium-ion transport in TEG intercalated $VOPO_4$ nanosheets is 0.22 eV, which is much lower than that of the pure $VOPO_4$ nanosheets

(0.72 eV). The simulations not only provide theoretical evidence for the much improved rate capability and cycling stability in the TEG and THF intercalated $VOPO_4$ nanosheets, but also strongly suggest that interlayer expansion is a powerful technique to improve the diffusion kinetics of large cations (such as $Na^+$) in layer-structured hosts. Our results afford deeper understanding on the interlayer-expansion strategy to boost the sodium-ion storage performance of the $VOPO_4$ nanosheets. Our results may also bring a paradigm shift of the current sodium-ion storage research to the exploration of large cations storage, such as $K^+$, $Mg^{2+}$, $Ca^{2+}$ even $Al^{3+}$.

# Chapter 6: Porosity engineering of transition metal oxide nanosheets for efficient energy storage*

## 6.1 INTRODUCTION

Two-dimensional (2D) nanocrystals offer exciting opportunities for both fundamental studies and many technological applications due to their unique and fascinating properties.[130, 131] This has been highlighted over the past decade by 2D graphene and transition metal dichalcogenides, which exhibit exceptional chemical/physical properties that are absent in their bulk counterparts and other dimensional nanostructures.[132-134] Mixed transition metal oxide (MTMO) nanomaterials have been widely studied as attractive candidates for electrocatalysis, photocatalysis, energy storage, and conversion technologies, owing to their mixed valence states and rich redox reactions.[135-137] Inspired by the success of 2D nanomaterials as mentioned above, it is of great interest to fabricate the MTMO materials into 2D nanostructures, which are expected to exhibit greatly improved properties in many energy related applications, especially alkali ion storage. However, up to now, MTMOs are mainly studied in the form of 0D nanoparticles,[138] 1D nanotubes or nanowires,[139] and 3D nanoclusters or microspheres.[140] In contrast, there are only a few reports studying the 2D nanostructured MTMOs, especially those with confined thickness.[141] MTMOs are intrinsically non-layered materials, which cannot be mechanically or chemically exfoliated to 2D nanostructures via the general top-down exfoliation methods.[142, 143] Therefore, a general

* L. Peng, P. Xiong, L. Ma, Y. Yuan, Y. Zhu, D. Chen, X. Luo, J. Lu, K. Amine, G. Yu, "Holey Two-Dimensional Transition Metal Oxide Nanosheets for Efficient Energy Storage" *Nat. Commun.*, **2017**, *8*, DOI: 10.1038/ncomms15139.
L. Peng carried out the experiments, analyzed the results, and wrote the paper. G. Yu supervised the project. All participated in the preparation of the project.

and facile bottom-up strategy for the controlled synthesis of 2D MTMO nanostructures is highly needed.

Although 2D nanomaterials generally exhibit improved capacity, rate capability, and cycling stability for lithium-on storage due to the abundant active sites for electrochemical reaction and the shortened lithium-ion diffusion distance, they still suffer from several disadvantages. 2D nanomaterials with high surface areas may consume more electrolytes for the formation of SEI, and cause more unwanted side reactions to deteriorate the battery performance.[144] The irreversible restacking of individual 2D nanosheets during materials processing or device fabrication may lead to the decrease of active surfaces for ion transport and storage. Moreover 2D TMO nanomaterials also suffer from severe morphology changes and structural degradation, especially in the first discharge cycle, due to the reduction of the metal cation to M(0).[145, 146] For example, Tarascon et al. reported cobalt oxide (CoO) nanoparticles as a good anode material with high lithium-ion storage capacity and capacity retention. The authors proved that when CoO nanoparticles were fully reduced by Li, the overall shape of the starting material can be preserved because the disintegrated metallic nanoparticles would be dispersed in a lithia ($Li_2O$) matrix, with the $Li_2O$ + nanoparticles being surrounded by a solid electrolyte interface.[147] Over the past decades, there is a great amount of research on simple and mixed transition metal oxides as lithium-ion battery and sodium-ion battery anodes,[148, 149] but detailed conversion reaction process in terms of the oxidation state changes (chemical stability) and morphology evolution (mechanical stability) are still relatively poorly understood. Given the fact that the mechanism of Li reactivity with metal oxides involves the formation and decomposition of $Li_2O$, accompanying the reduction and oxidation of metal nanoparticles (in the range 1-5 nm) respectively, the chemical/mechanical stability of these metal oxides and the detailed understanding of their oxidation state changes

during electrochemical processes are crucial for further optimization of electrochemical performance.

Here we report a general two-step strategy for controlled synthesis of holey 2D TMO nanosheets with tunable pore sizes using graphene oxides as a sacrificial template. This approach has demonstrated to synthesize various 2D holey TMO nanosheets, including simple oxides such as $Fe_2O_3$, $Co_3O_4$, $Mn_2O_3$, and mixed oxides such as $ZnMn_2O_4$ (ZMO), $ZnCo_2O_4$ (ZCO), $NiCo_2O_4$ (NCO), and $CoFe_2O_4$ (CFO). As a result, 2D holey TMO nanosheets exhibit much improved the rate capability and cycling stability for both lithium and sodium-ion storage, due to the increased surface areas and interfaces, and facile interfacial transport and shortened diffusion paths. What's more, the operando X-ray diffraction (XRD) and X-ray absorption structures (XAS) were employed to investigate the mechanism for charge storage in the conversion reaction involving 2D holey $ZnMn_2O_4$ (ZMO) nanosheets and to understand the oxidation state changes of Zn and Mn elements. We also use in-situ transmission electron microscopy (TEM) to follow the morphology evolution of the 2D holey ZMO nanosheets during lithiation/delithiation and pressing process in real time. Operando XRD and XAS results show that holey ZMO nanosheets deliver high capacity due to the formation of ZnLi alloy as well as the reversible transformation between $Mn^{2+}$ and $Mn^{3+}$. In-situ TEM characterizations show that 2D holey ZMO nanosheets composed of chemically interconnected metal oxide nanoparticles inherit the strong mechanical properties from graphene oxide, maintaining the holey morphology and displaying minimal structural changes during the lithiation/delithiation processes and under press states. The electrochemical results, in combination of the in-situ TEM, operando XRD and XAS studies, show that these 2D holey nanostructured TMO materials are a promising material platform for both fundamental understanding of the electrode stability during lithiation/delithiation, and for

improving electrochemical performance because of the synergistic effects of the inherently good chemical/mechanical stability and the enhanced charge transport properties.

## 6.2 EXPERIMENT DETAILS

### 6.2.1 Synthesis of graphene oxide (GO)

GO was prepared from purified natural graphite by a modified Hummers' method. Simply, 10 g of graphite powder was first added to 15 mL of concentrated $H_2SO_4$. 5 g of $K_2S_2O_8$ and 5 g of $P_2O_5$ were then added slowly. The as-obtained mixed solution was heated to 80 °C and maintained at this temperature for 6 h. After cooling to room temperature, the resultant was carefully diluted with distilled water, filtered, and washed on the filter until the rinse water pH became neutral. The product was dried in air at ambient temperature overnight. Then the preoxidized graphite was added to 230 mL of concentrated $H_2SO_4$ cooled in an ice-water bath. 30 g of $KMnO_4$ was added very slowly into the mixture with stirring and cooling. All the operations were carried out very slowly in a fume hood. The mixture was then stirred at 35 °C for 30 min. 460 mL of distilled water was slowly added to cause an increase in temperature to 98 °C and the mixture was maintained at that temperature for 15 min. The reaction was terminated by adding 1.4 L of distilled water followed by 10 mL of 30% $H_2O_2$ solution. The solid product was separated by centrifugation, washed repeatedly with 5% HCl solution, and then dialyzed for a week.

### 6.2.2 Synthesis of 2D holey MTMO nanosheets

The 2D holey MTMO nanosheets were prepared via a facile two-step approach. In a typical synthesis of 2D holey ZMO nanosheets, 30 mg of GO powder was first dispersed into 75 mL of ethylene glycol with sonication for 120 min. 0.5 mmol of

$Zn(CH_3COO)_2 \cdot 2H_2O$ and 1.0 mmol of $Mn(CH_3COO)_2 \cdot 4H_2O$ were dissolved in 25 mL of ethylene glycol. The above two systems were then mixed together, and stirred at ambient temperature for at least 60 min to obtain a homogenous suspension. The obtained suspension was then transferred into a round bottom flask and heated to 170 °C in an oil bath, and kept at this temperature with stirring for 120 min. After the mixture was cooled down to room temperature naturally, and the as-made precipitate was collected by centrifugation and washed with ethanol for several times. The product (donated as ZMO precursors/GO) was then dried in vacuum at 80 °C overnight. In the second step of synthesis, the as-made ZMO precursors/GO from the first step was annealed at 400 °C in air for 120 min with a slow heating rate of 0.5 °C $min^{-1}$ to get the 2D holey ZMO nanosheets. To prepare control ZMO sample, 0.5 mmol of $Zn(CH_3COO)_2 \cdot 2H_2O$, 1.0 mmol of $Mn(CH_3COO)_2 \cdot 4H_2O$ and 100 mL of ethylene glycol were used for the reaction without any GO added as the typical synthesis mentioned above. The reduced graphene oxide (rGO) was prepared via the first step of the synthesis without $Zn(CH_3COO)_2 \cdot 2H_2O$ and $Mn(CH_3COO)_2 \cdot 4H_2O$. To evaluate the influence of calcination temperature, the as-made ZMO precursors/GO was annealed at 400 °C, 500 °C, and 600 °C in air for 120 min with same heating rate (0.5 °C $min^{-1}$), donated as 2D holey ZMO-400, 2D holey ZMO-500, 2D holey ZMO-600, respectively. 2D holey ZCO nanosheets were prepared with $Zn(CH_3COO)_2 \cdot 2H_2O$ and $Co(CH_3COO)_2 \cdot 2H_2O$ in the presence of GO as the same method mentioned above. 2D holey NCO nanosheets were prepared by replacing $Zn(CH_3COO)_2 \cdot 2H_2O$ and $Mn(CH_3COO)_2 \cdot 4H_2O$ with $Ni(CH_3COO)_2 \cdot 4H_2O$ and $Co(CH_3COO)_2 \cdot 4H_2O$ as the same method mentioned above. 2D holey CFO nanosheets were prepared by replacing $Zn(CH_3COO)_2 \cdot 2H_2O$ and $Mn(CH_3COO)_2 \cdot 4H_2O$ with $Co(NO_3)_2 \cdot 6H_2O$ and $Fe(NO_3)_3 \cdot 9H_2O$ as the same method mentioned above.

### 6.2.3 Materials characterization

The structure of the as-synthesized samples was characterized by powder X-ray diffraction (XRD) patterns performed on a Philips Vertical Scanning diffractometer. The morphology of the samples was investigated using scanning electron microscope (SEM), scanning transmission electron microscope (STEM) (Hitachi S5500), and transmission electron microscope (TEM) (JEOL 2010F). The TG analysis was tested by a TGA/SDTA851e thermogravimetric analyzer under an air atmosphere from 25 to 850 °C at a heating rate of 10 °C $min^{-1}$. In-situ TEM was carried out using a Nanofactory holder capable of biasing. At beginning, 2D holey $ZnMn_2O_4$ nanosheets were loaded to one gold tip by conductive glue, and metallic Li was attached to the other Tungsten tip. During the sample transfer into a JEOL 3010 TEM chamber, Li metal was exposed to air for about 30 seconds and was oxidized to $Li_2O$ on the surface, which acts as the solid electrolyte. After the samples were loaded in the TEM, a +3 V bias (on the $Li/Li_2O$ side) was applied to initiate the lithiation process. The mechanical press/release was carried out after $ZnMn_2O_4$ nanosheets is fully lithiated and the bias is off.

### 6.2.4 Electrochemical measurements

The working electrodes were prepared by mixing active materials (2D holey ZMO nanosheets) and polyvinylidene difluoride (PVDF) at a weight ratio of 90:10, in N-methyl-2-pyrrolidinone (NMP). Then the slurries were coated onto a copper foil. The as-prepared electrodes were dried under vacuum at 110 °C for 10 h. The loading of active materials was ~1.0 mg $cm^{-2}$. After being sealed, the electrodes were assembled into coin cells (CR2032) in an argon-filled glovebox using Celgard 2320 as separator, 1 mol $L^{-1}$ $LiPF_6$ in ethylenecarbonate (EC) and diethylenecarbonate (DEC) (1:1, v/v) as the electrolyte and Li metal as the counter electrode. The assembled coin cells were tested on an Arbin battery test system with a voltage range of 0.01~3.0 V. For comparison, the free

ZMO samples are used as the active materials, named as Control ZMO. The free ZMO samples physically mixed with Super P carbon in the weight ratio of 75:25 are also used as the active materials, named as Control ZMO+SP. The 2D holey NCO nanosheets based electrode for sodium-ion batteries were prepared by mixing active materials (2D holey NCO nanosheets), superP, sodium carboxymethyl cellulose (CMC) at a weight ratio of 80:10:10, in water. The electrolyte used for sodium-ion battery tests was 1 M $NaClO_4$ dissolved in propylene carbonate (PC) with 2% FEC (fluoroethylene carbonate) additive.

## 6.3 RESULTS AND DISCUSSION

### 6.3.1 Synthesis and characterization of 2D holey MTMO nanosheets

The key concept for general synthesis of 2D holy TMO nanosheets is illustrated in **Figure 6.1**A. In brief, GO was first employed as a template to grow various TMO precursors on its surfaces, followed by post-thermal treatment to transform TMO precursors to 2D holey TMO nanosheets owing to the synergistic effects of chemical interconnection of TMO nanoparticles and controlled decomposition of GOs. In a typical experiment, TMO precursor/rGO composites were firstly prepared via solution-phase reaction between transition metal ions and GO, which was partially reduced to reduced graphene oxide (rGO).[150] The resulting TMO precursor/rGO were then annealed to induce pyrolysis of rGO templates and formation of crystallized TMO nanoparticles, which interconnected chemically with each other to form the 2D holey nanosheets. Taking 2D holey ZMO nanosheets as an example, GO was firstly dispersed in ethylene glycol solution by ultrasonication. Afterwards, $Zn(CH_3COO)_2$, and $Mn(CH_3COO)_2$ were added into GO suspensions. Then stable and homogenous suspensions were obtained by stirring to ensure the complete adsorption of $Zn^{2+}$ and $Mn^{2+}$ cations onto the surfaces of

GO. After refluxing, the black ZMO precursors/rGO precipitates were washed and collected by centrifugation. Low magnification STEM image (Figure 6.1B) shows a typical sheet-like morphology of the ZMO precursors/rGO, indicating that rGO served as a general template for supporting the ZMO precursors.

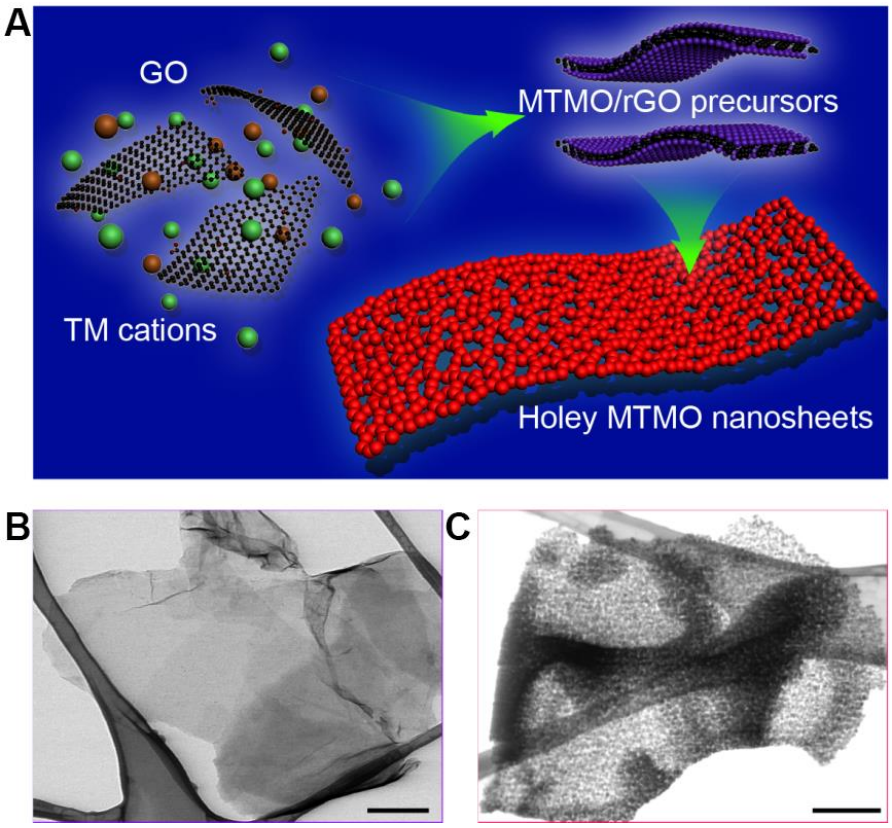


**Figure 6.1. Schematic illustration of the synthesis process of 2D holey TMO nanosheets.** (A) Schematic showing the general strategy to synthesize 2D holey TMO nanosheets. Two transition metal (TM) cations are mixed with graphene oxide (GO) and then anchored on surfaces of reduced graphene oxide (rGO) templates during the solution-phase reaction. 2D holey MTMO nanosheets composed of interconnected MTMO nanocrystals are formed after removing rGO templates during post-calcination. (B) STEM image of ZMO precursor/rGO shows sheets-like morphology. (C) STEM image of 2D holey ZMO nanosheets shows holey nanosheets composed of interconnected ZMO nanocrystals. Scale bar, 200 nm (b, c).

Post-calcination of the as-prepared ZMO precursors/rGO induced the transformation of amorphous precursors into crystalline ZMO nanosheets without altering their 2D morphology, and simultaneous decomposition of rGO (**Figure 6.2**). The typical STEM images (Figure 6.1C and Figure 6.2C) of the samples after calcination confirm that 2D nanosheet structures had been reserved in the final products. However, the nanosheets had been transformed from a dense structure with smooth surfaces (Figure 6.1B) into a highly holey nanosheet (**Figure 6.3**A and B). The as-synthesized holey nanosheets showed good uniformity in lateral size (~500 nm) and thickness (~20 nm) (**Figure 6.4**). HRTEM (Figure 6.3C) image reveals the 2D holey nanosheets consist of interconnected nanocrystallites of ~8 nm in size. Moreover, the crossed two fringes in the overlapped domains (Figure 6.3C) reveal that the ZMO nanoparticles indeed are chemically connected with each other. The clear lattice fringes of ~0.25 nm (Figure 6.3C) correspond well to the (211) plane of the spinel ZMO. The diffused concentric rings shown in selected area electron diffraction (SAED) pattern (inset of Figure 6.3C) indicated the polycrystalline structure. The diameters of the diffraction rings are indexed to spinel ZMO in agreement with the XRD analysis (Figure 6.2A). The STEM (Figure 6.2C) and corresponding elemental mapping (Figure 6.2D) display the uniform distribution of Zn, Mn, O elements with rare C element, which further demonstrates that the 2D holey nanosheets are composed of the ZMO nanoparticles.

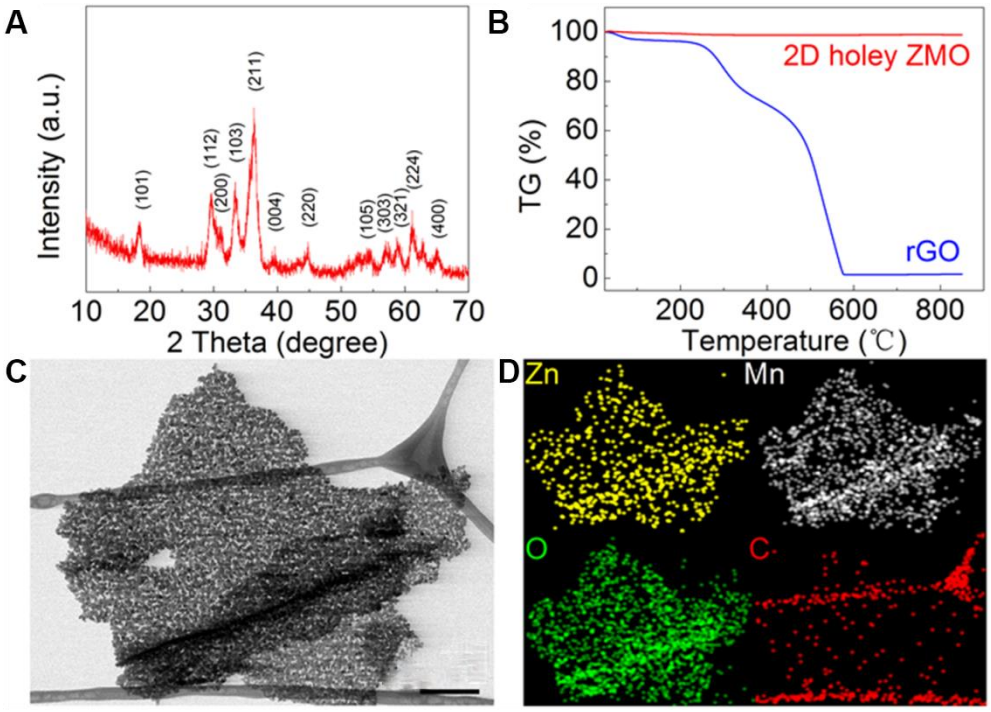


**Figure 6.2. Characterization of 2D holey ZMO nanosheets.** (A) XRD pattern of 2D holey ZMO nanosheets indicating the conversion of the precursor compound into spinel $ZnMn_2O_4$ (JCPDS card No. 24-1133). (B) TG analysis of reduced graphene oxide (rGO) and 2D holey ZMO nanosheets. (C) STEM image and (D) corresponding elemental mapping of 2D holey ZMO nanosheets. Scale bar in C, 200 nm.

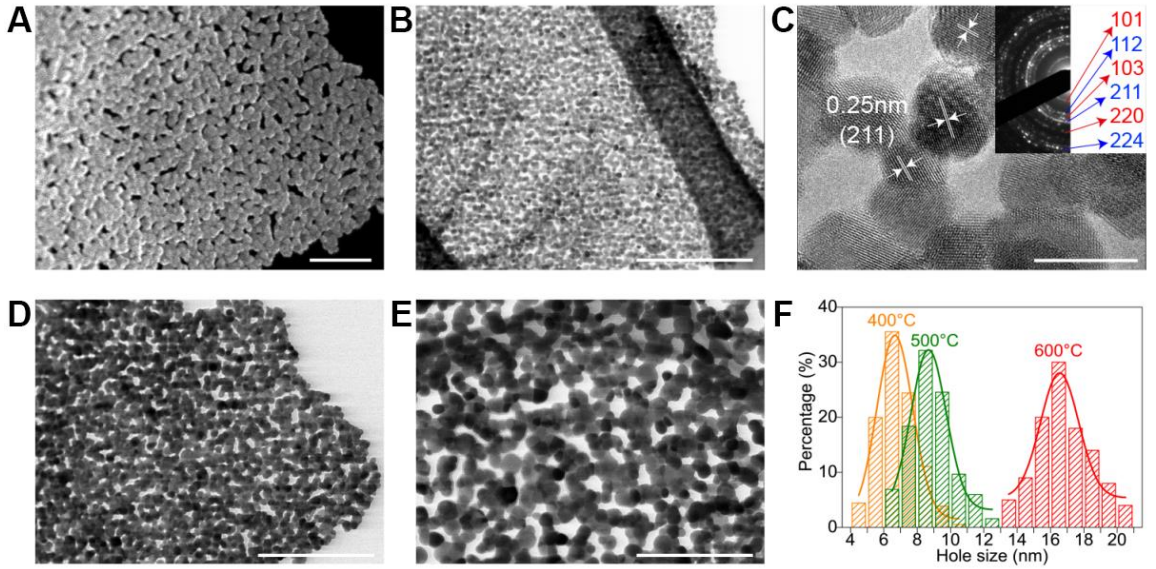


**Figure 6.3. Electron microscopic images of 2D holey ZMO nanosheets.** SEM image (A), STEM image (B) and high-magnification TEM image (C) of 2D holey ZMO nanosheets prepared at post-calcination temperature of 400 °C. Corresponding SAED pattern of 2D holey ZMO nanosheets (Inset of c). STEM image of 2D holey ZMO nanosheets prepared at different post-calcination temperature: (D) 500 °C and (e) 600 °C. Corresponding hole size distribution (F) obtained by statistics analysis of the STEM images shown in B, D, and E. Scale bar, 100 nm (A), 200 nm (B, D, E), 10 nm (C).

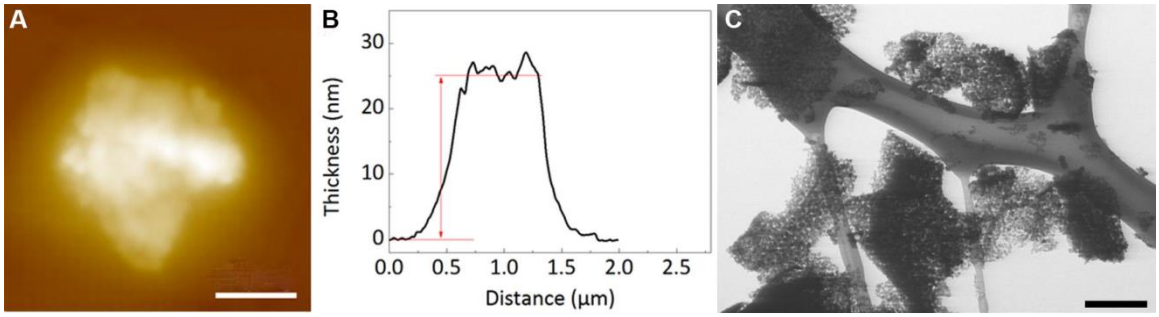


**Figure 6.4. AFM image and the corresponding height profile and the low magnification SEM image of ZMO nanosheets obtained under 400℃.** (A) AFM image of ZMO nanosheets. Scale bar, 500 nm. (B) Height profile of ZMO nanosheets.

GO is playing an important role in the formation of 2D holey ZMO nanosheets. First, GO is a 2D template with sufficient oxygen-contained groups, which ensures the growth of ZMO precursors on its surfaces. This is essential for the formation of 2D

nanostructure. Second, unlike the conventional templating process where little interactions exist between the precursors and templates, the ZMO precursors were anchored covalently on rGOs through residual functional group such as carboxyl, hydroxyl, and epoxy groups (**Figure 6.5**).[151, 152] Owing to the intimate interaction between ZMO and rGO, the ZMO nanoparticles partially agglomerated and chemically linked with each other to form the holey nanosheets during the thermal treatment, as identified as HRTEM of ZMO nanoparticles. Third, rGO template is highly flexible, which may contribute to maintaining the structure stability of 2D holey nanosheets during calcination. Due to the chemically integration between ZMO precursors and GO, the as-synthesized ZMO nanoparticles inherited the strong mechanical properties from the GO nanosheets. Free ZMO was synthesized via the same method without any GO added as a control experiment. Only an aggregated flower-like structure assembled by spinel ZMO discs was obtained (**Figure 6.6**A and B). No holey nanosheet structures were formed (Figure 6.6C and D).

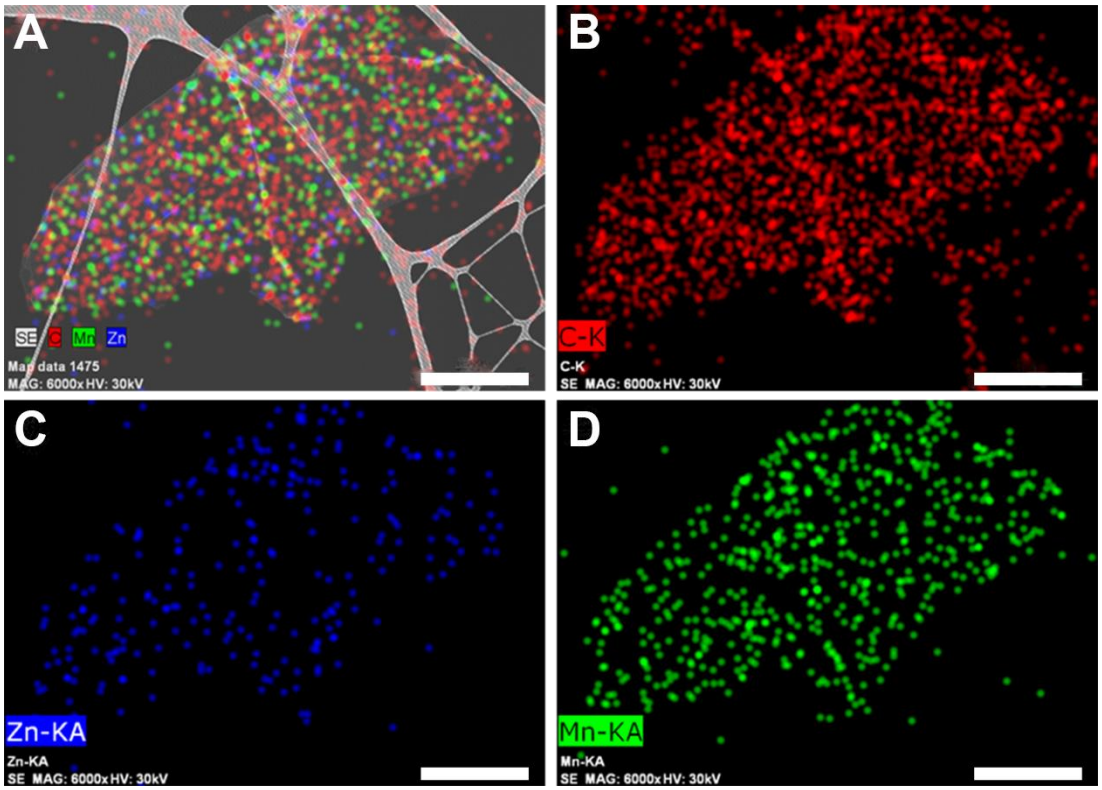


**Figure 6.5. EDX mapping of GO nanosheets after stirring for enough time with $Zn^{2+}$ and $Mn^{2+}$ cations, showing the good adsorption of $Zn^{2+}$ and $Mn^{2+}$ cations onto GO nanosheets.** (A) STEM image of GO nanosheets adsorbed with $Zn^{2+}$ and $Mn^{2+}$ cations. (B) C element distribution in the precursor nanosheets. (C) Zn element distribution in the precursor nanosheets. (D) Mn element distribution in the precursor nanosheets. Scale bar in all images, 5 mm.

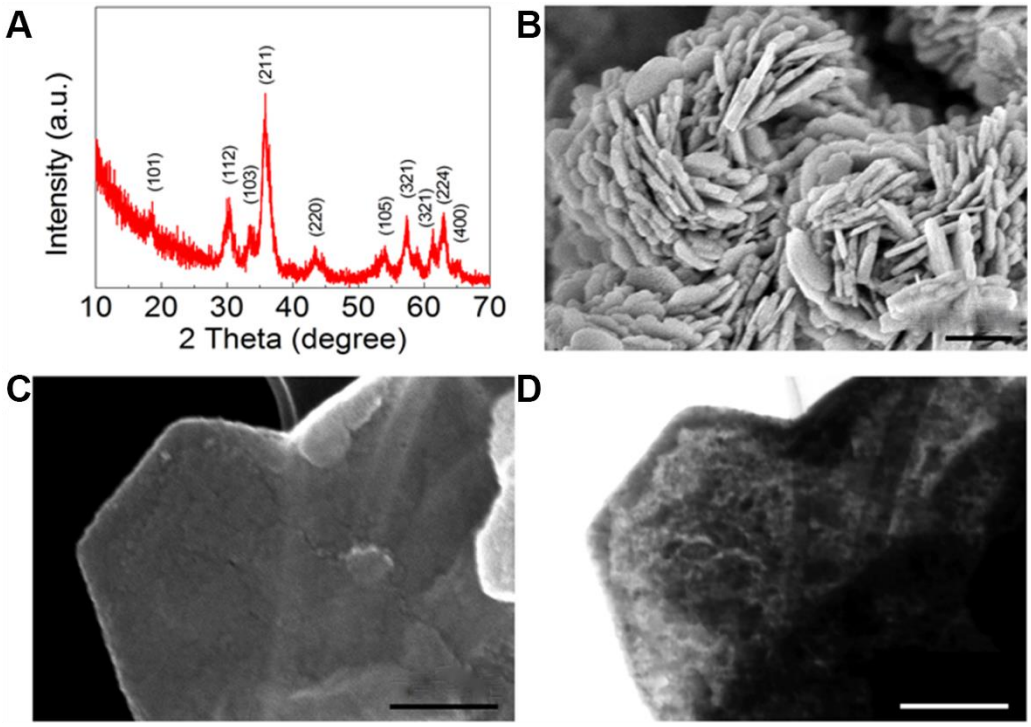


**Figure 6.6. Characterization of free ZMO particles synthesized without addition of GO.** (A) XRD patterns of free ZMO sample. (B) SEM image of free ZMO. Scale bar, 500 nm. (C) Enlarged SEM and (D) corresponding STEM images of free ZMO. Scale bar in C and d, 100 nm.

In many electrochemical energy devices, it is highly desirable to control nanomaterials with tunable pore/hole sizes, since the opening of holes or pores may have a significant effect on their electrochemical performances.[153, 154] This is particularly true for 2D nanomaterials as when processed as electrode materials, restacking of nanosheets often leads to substantially reduced active surfaces for electrochemical reactions and suppressed mass transport. In our work, the hole size of 2D holey ZMO nanosheets prepared by such strategy can be adjustable by readily tuning the annealing temperature during post-calcination process. Figure 6.3B, D and E show STEM images of 2D holey ZMO nanosheets prepared by calcination at 400 °C, 500 °C, and 600 °C, respectively. The 2D holey nanosheets structure was well maintained at all temperatures, while the

ZMO particles grew bigger and showed more agglomerated as the temperature increases. From Figure 6.3F it is evident that the hole size of 2D holey ZMO nanosheets increased with the increasing calcination temperature. The hole sizes of 2D holey ZMO nanosheets obtained at different temperatures were further tested and verified by the BET characterizations (**Figure 6.7**). The BET results gave the average hole sizes of 5~10 nm, 7~17 nm, and ~20 nm for the samples obtained at 400 °C, 500 °C, and 600 °C, respectively, which were consistent with the values obtained from the STEM images.

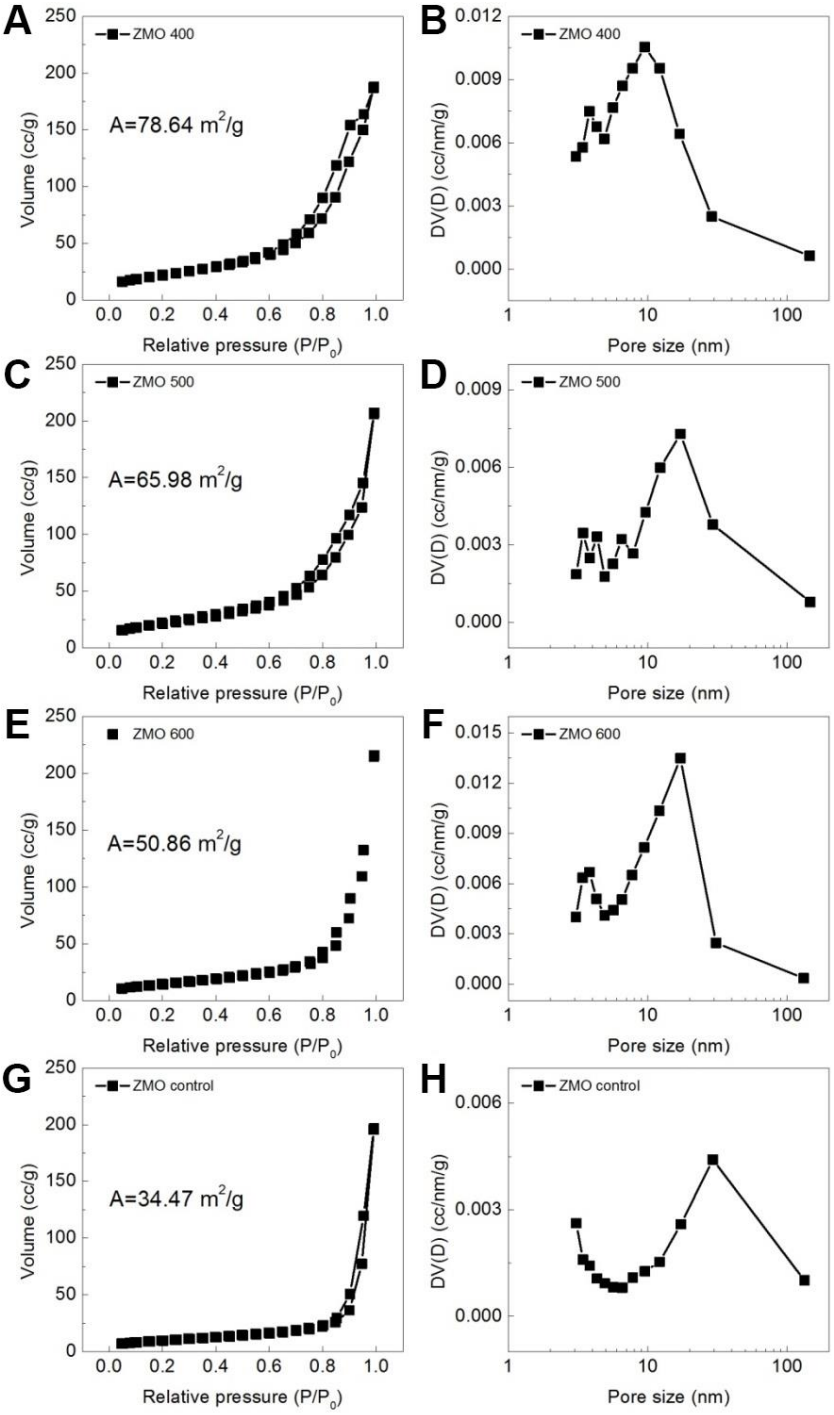


**Figure 6.7. Isotherm results and BJH pore size distribution of ZMO nanosheets prepared at different calcination temperatures.** (A, B) ZMO nanosheets at 400 °C; (C, D) ZMO nanosheets at 500 °C; (E, F) ZMO nanosheets at 600 °C; (G, H) control ZMO nanoplates.

More importantly, such strategy is versatile and can be extended to prepare other 2D holey MTMO nanosheets. **Figure 6.8**A, E and I show SEM images of 2D holey $ZnCo_2O_4$ (ZCO), $NiCo_2O_4$ (NCO) and $CoFe_2O_4$ (CFO) nanosheets prepared by the same approach, respectively. STEM images of 2D holey $ZnCo_2O_4$ (ZCO), $NiCo_2O_4$ (NCO) and $CoFe_2O_4$ (CFO) nanosheets were shown in Figure 6.8B, F, and J, respectively. In comparison with the 2D ZMO nanosheets shown in Figure 6.3A and B, similar 2D holey structures were clearly observed in all these cases. HRTEM (Figure 6.8C, G, and K) images reveal these 2D holey nanosheets all consist of chemically interconnected MTMO nanocrystallites. The lattice fringes (Figure 6.8C, G, and K) and SAED patterns (inset of Figure 6.8C, G, and K) confirm that the 2D ZCO, NCO, and CFO nanosheets were composed of spinel ZCO, NCO, and CFO, respectively, corresponding well to XRD results (Figure 6.8D, H, and L).

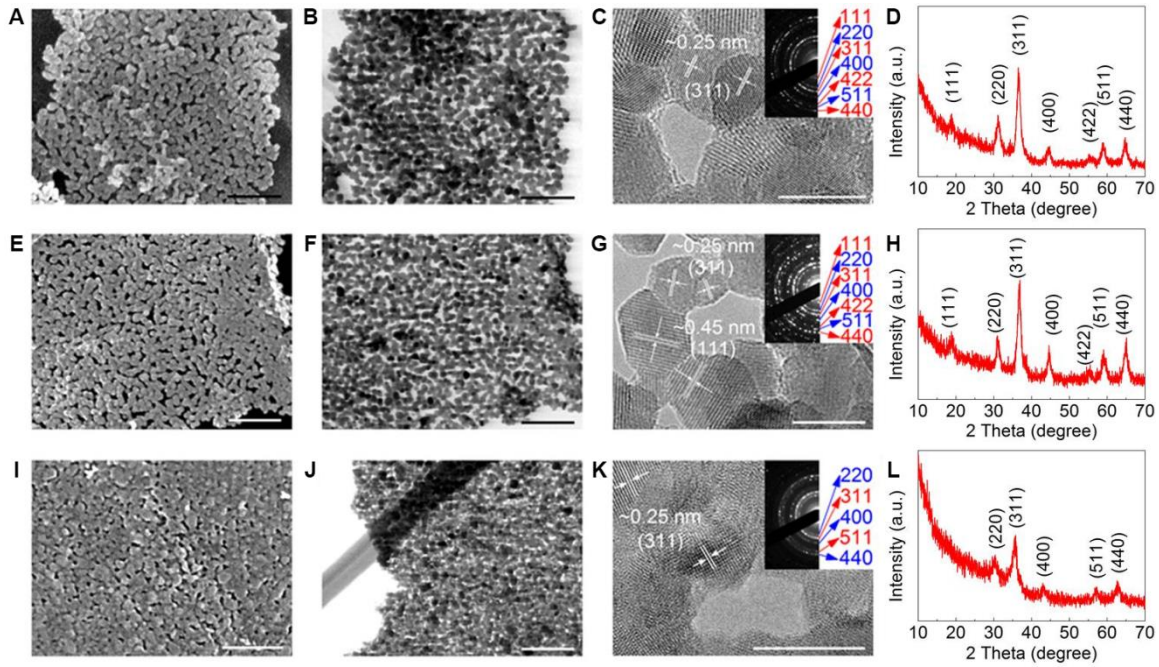


**Figure 6.8. Electron microscopic images of versatile 2D holey MTMO nanosheets.** SEM images (A, E, I), STEM images (B, F, J) and high-magnification TEM images and SAED patterns (C, G, K) of 2D holey nanosheets of ZCO, NCO, and CFO. Scale bar, 100 nm (a, b, d, e, g, h), 10 nm (c, f, i). XRD patterns (D, H, L) of ZCO, NCO, and CFO.

### 6.3.2 Electrochemical properties

#### *6.3.2.1 2D holey MTMO nanosheets as anodes for lithium-ion battery*

Prompted by their unique morphology, these 2D holey MTMO nanosheets are expected to show promising applications in electrochemical energy storage devices. For example, when used as anodes for lithium-ion batteries, these 2D holey nanosheets may afford large surface areas and enable facile transport of the electrolyte, resulting in rapid charge transfer due to the shortened diffusion paths. **Figure 6.9** shows the charge and discharge curves of 2D holey ZMO nanosheets for the first two cycles in range of 0.01 and 3.0 V. The voltage profile of the first charge comprised mainly two regions, a large plateau at 0.5 V associated with the irreversible reaction between Li and ZMO, which

was followed by a slope till 0.01 V. The discharge curve showed no large plateau but only a slope due to oxidation reactions of $Mn^0$ and $Zn^0$ to $Mn^{2+}$ and $Zn^{2+}$. The following charge and discharge slopes reflected the reversible reactions between $Mn^0$, $Zn^0$ and $Mn^{2+}$, $Zn^{2+}$ and Zn−Li alloying/de-alloying reactions. The initial capacity loss is attributed to the formation of solid electrolyte interface (SEI)[43]. After several conditioning cycles, the Coulombic efficiency increased to higher than 98% (**Figure 6.10**A), indicating good reversibility of the above conversion reactions. After initial 2 cycles for activation, 2D holey ZMO nanosheets were cycled at a current density of 800 mA $g^{-1}$ for 50 cycles (Figure 6.10A). A stable specific capacity of ca. 500 mAh $g^{-1}$ (all specific capacities estimated based on the mass of active materials) was observed after 50 cycles. The control ZMO+SP and control ZMO samples (synthesized without GO template) were also cycled for 50 cycles with the same conditions (Figure 6.10A), while specific capacities of ca. 320 and ca. 100 mAh $g^{-1}$ were obtained, respectively.

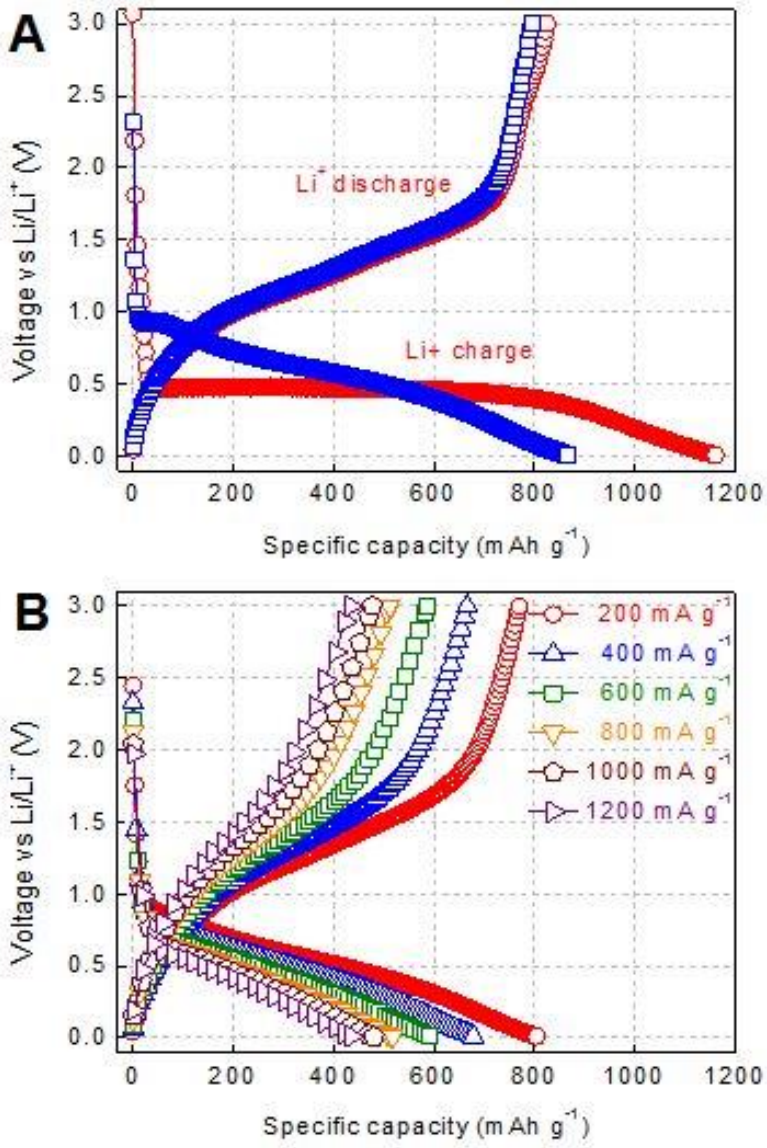


**Figure 6.9. Electrochemical performances of 2D holey ZMO nanosheets.** (A) Charge and discharge curves of 2D holey ZMO nanosheets for the first two cycles at a current density of 200 mA $g^{-1}$. (B) Representative charge and discharge curves of 2D holey ZMO nanosheets at various current densities.

The rate capability of the as-prepared 2D holey ZMO nanosheets was compared with control ZMO+SP and control ZMO as well (Figure 6.10B). For the first few cycles at a low current density of 200 mA $g^{-1}$, the 2D holey ZMO nanosheets showed an

average specific capacity of ca. 770 mAh $g^{-1}$ (Figure 6.9B). Even at a high current density of 1200 mA $g^{-1}$, the specific capacity was still as high as ~ 430 mAh $g^{-1}$ (Figure 6.9B) with a ~56% capacity retention. An average specific capacity of ~ 710 mAh $g^{-1}$ at 200 mAh $g^{-1}$ was retained after 110 cycles of charge and discharge at various current densities. However, for control ZMO+SP and control ZMO, only ~32% and ~6% capacity retention were obtained respectively, as current density increased from 200 to 1200 mAh $g^{-1}$. The superior rate performance was also confirmed in the 2D holey ZMO sample prepared at different temperatures. The samples treated at 400 °C and 500 °C showed the comparable electrochemical performance. While a prominent decrease of rate performance was observed when the calcination temperature increased to 600°C (**Figure 6.11**). The more aggregated structure and bigger particle size may be attributed to the decreased performance. Furthermore, cycling stability measurement of 2D holey ZMO nanosheets was shown in Figure 6.10C. After five cycles of electrochemical activation at 100 mA $g^{-1}$, a stable specific capacity of ca. 480 mAh $g^{-1}$ was retained after 1,000 cycles at the current density of 800 mA $g^{-1}$. And the average Coulombic efficiency from the 1st to 1,000th cycle is 99.8%. The excellent Coulombic efficiency can be attributed to the electrochemical activation process, which facilitates the formation of SEI layers.[155] All these 2D holey nanosheets exhibited high cycling stability revealing this strategy is a general route for the synthesis of 2D holey nanomaterials with exceptional lithium storage ability. The cycling stability and rate capability of these 2D holey MTMO nanosheets are compared with the reported MTMO-based anodes. The 2D holey MTMO nanosheets exhibit superior performances.

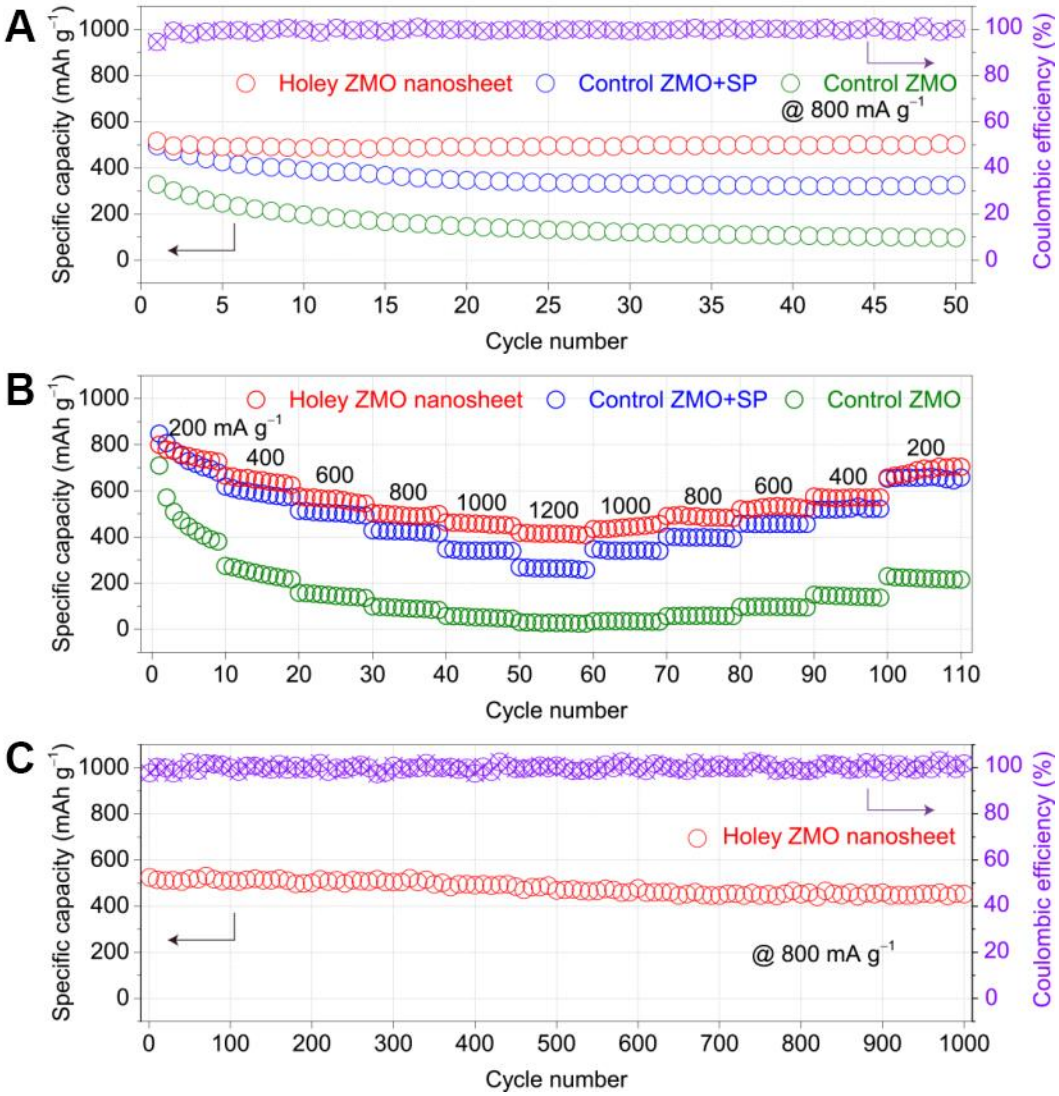


**Figure 6.10. 2D holey ZMO nanosheets as high-performance anodes for lithium-ion batteries.** (A) Cycling performance of 2D holey ZMO nanosheets, control ZMO+SP and control ZMO at current density of 800 mA $g^{-1}$ for 50 cycles. Coulombic efficiency of 2D holey ZMO nanosheets at current density of 800 mA $g^{-1}$ for 50 cycles. (B) Rate performance of 2D holey ZMO nanosheets, control ZMO+SP and control ZMO at different current densities from 200 to 1,200 mA $g^{-1}$. (C) Long-term cycling stability and Coulombic efficiency of 2D holey ZMO nanosheet at current density of 800 mA $g^{-1}$ for over 1,000 cycles.

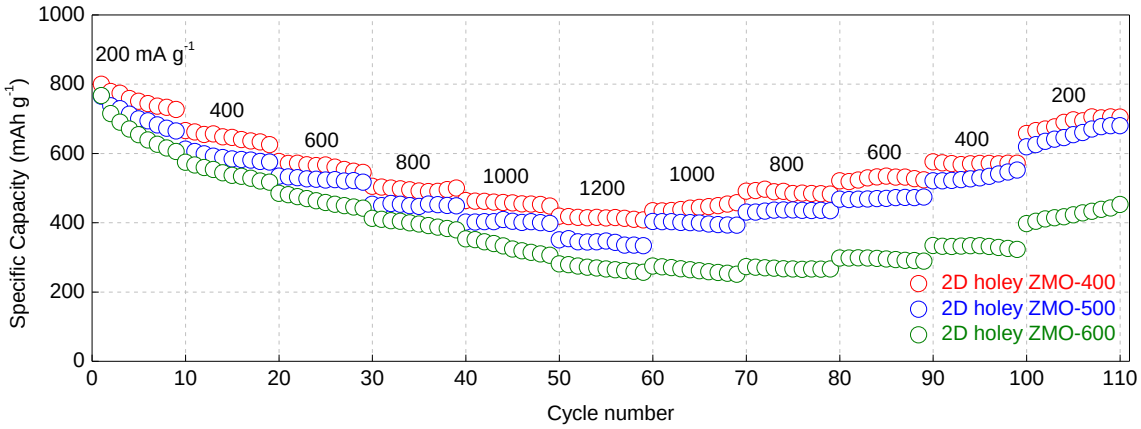


**Figure 6.11. Rate performances of 2D holey ZMO nanosheets prepared at different temperature.** 2D holey ZMO-400, 2D holey ZMO-500, and 2D holey ZMO-600 stand for the 2D holey ZMO nanosheets prepared at 400, 500, and 600 °C, respectively.

Clearly, the high rate capability, excellent cyclic stability, and Coulombic efficiency observed for the 2D holey ZMO nanosheets can be ascribed to the unique features of 2D holey nanostructures with favorable properties. Firstly, the 2D nanosheets with large surface areas and short diffusion length facilitate effective lithium-ion transport. Secondly, the interconnected holes on the surfaces of 2D nanosheets enable facile diffusion of liquid electrolyte into the bulk of the electrode materials and greatly reduce the lithium-ion diffusion length.[156] Even without adding conductive carbon in the electrodes, electrons could be easily transported continuously along well-interconnected nanocrystals. This is particularly helpful when the battery is charged or discharged at high currents. Finally, these interconnected holes can help alleviate the strain generated from volume change, thus improving the cycling stability and coulombic efficiency.[157] As shown in **Figure 6.12**, 2D holey ZMO nanosheets could still preserve the structure integrity and holey structure after 100 cycles. Such 2D holey nanostructures might endow these materials with many intriguing applications including supercapacitors, catalysis, electrochemical sensors, etc.

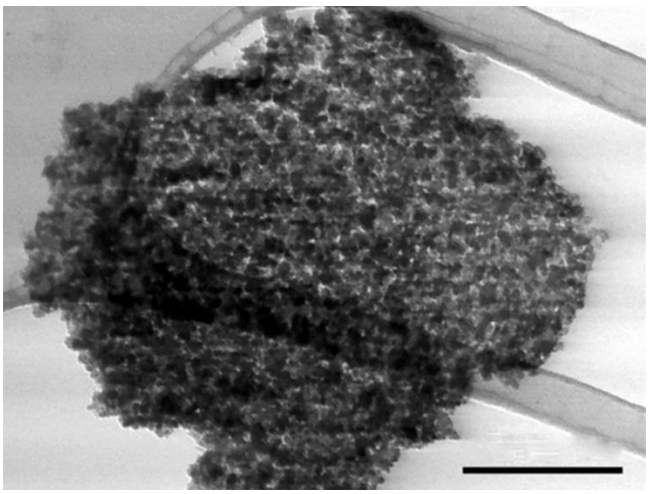

**Figure 6.12. STEM image of 2D holey ZMO nanosheets after 100 cycles.** The 2D holey nanostructures were reserved. To prepare the STEM sample, the cell was opened after several cycling, the 2D holey ZMO nanosheets anode washed with dimethyl carbonate (DMC) and sonicated in ethanol, and then the ethanol suspension was drop dried onto a STEM grid. Scale bar, 200 nm.

#### *6.3.2.2 2D holey MTMO nanosheets as anodes for sodium-ion battery*

As discussed above, 2D holey MTMO nanosheets possess both 2D nanostructure and tunable porosity, which may contribute to greatly improved electrochemical performance compared to conventional nanosheets electrodes with smooth surfaces. To demonstrate the advantageous features for electrochemical energy storage, 2D holey MTMO nanosheets were further explored as anodes for sodium-ion batteries. **Figure 6.13**A shows the galvanostatic charge/discharge profiles of the 2D holey NCO nanosheets for the 1st and 2nd cycles at a current density of 100 mA $g^{-1}$. The first discharge curve presents a sloping curve in the potential range of 1.2~0.2 V and a flat wide plateau at 0.2 V. The flat wide plateau located at 0.2 V and a small plateau at 0.7 V in the first cycle corresponds to the reduction of NCO to metallic cobalt and nickel (Co and Ni) and the electrochemical formation of $Na_2O$ ($NiCo_2O_4 + 8Na^+ + 8e^- \rightarrow Ni + 2Co +$

$4Na_2O$), accompanied by the formation of a SEI film.[158] The initial discharge capacity can reach ~980 mAh $g^{-1}$, while its reversible capacity is ~670 mAh $g^{-1}$ with a coulomb efficiency of ~ 68.4%. In the following cycle, the charge/discharge curves are stabilized gradually, reaching around 96% coulomb efficiency. Figure 6.13B compares the rate performance of the 2D holey NCO nanosheets and control NCO nanoplates without porosity for SIBs. At current densities of 200, 400, 800, 1,600 and 3,200 mA $g^{-1}$, the 2D holey NCO nanosheets deliver the capacities of ca. 550, 420, 300, 230 and 170 mAh $g^{-1}$, respectively. When the current density is reverted gradually to 200 mA $g^{-1}$, the average discharge capacity can be increased reversibly back to 420 mAh $g^{-1}$. While the control NCO nanosheets without porosity only deliver a low capacity of ~60 mAh $g^{-1}$ at the current density of 1600 mA $g^{-1}$ and can be hardly charged/discharged at higher current density. Figure 6.13C shows the long-term cycling stability and Coulombic efficiency of 2D holey NCO nanosheets and control NCO nanosheets at current density of 1600 mA $g^{-1}$ for 100 cycles. A stable specific capacity of ca. 160 mAh $g^{-1}$ was observed after 100 cycles for the 2D holey NCO nanosheet anodes. For comparison, the control anodes, NCO nanosheet without porous structure, showed the specific capacities of ca. 36 mAh $g^{-1}$ after 100 cycles. These high rate capability and excellent cyclic stability can be attributed to the unique 2D holey structure of the NCO nanosheets. The unique 2D holey structure will enable facile diffusion of liquid electrolyte into the bulk of the electrode materials and greatly reduce the lithium-ion diffusion length, thus improving the rate capability. Also, these interconnected holes can also maintain the holey framework of the nanosheets and accommodate volume change during charging/discharging, thus improving the cycling stability and coulombic efficiency.

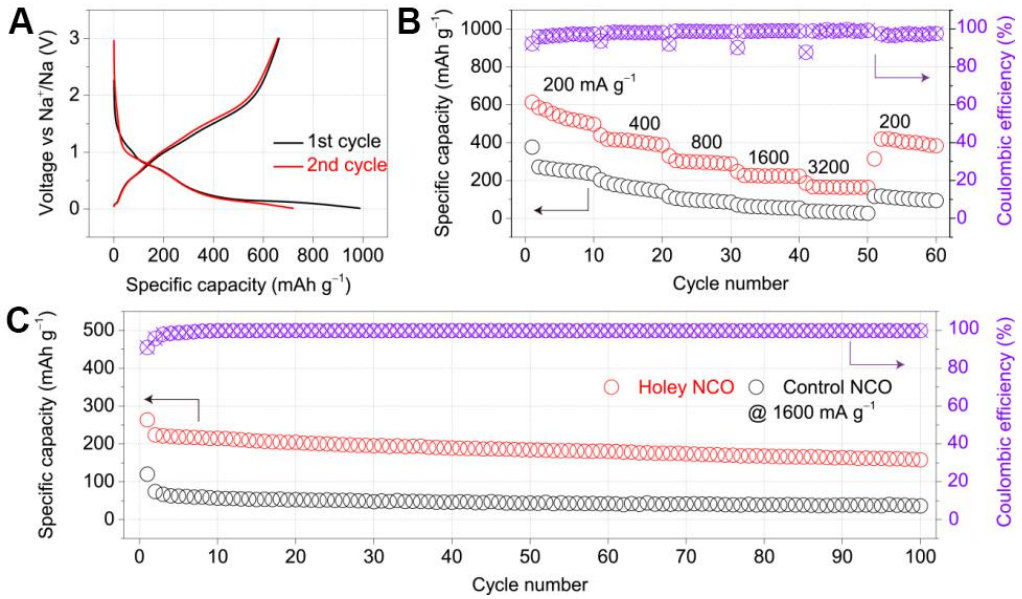


**Figure 6.13. 2D holey NCO nanosheets as anodes for sodium-ion batteries.** (A)Charge/discharge profiles of 2D holey NCO nanosheets for the 1st and 2nd cycles at a current density of 100 mA $g^{-1}$. (B) Rate performances of 2D holey NCO nanosheets (red circle) and control NCO nanosheets (black circle) from 200 to 3,200 mA $g^{-1}$. (C) Long-term cycling stability and Coulombic efficiency of 2D holey NCO nanosheet and control NCO nanosheet at current density of 1,600 mA $g^{-1}$ for 100 cycles.

### *6.3.2.3 In-situ TEM studies of 2D holey MTMO nanosheet anodes*

The high storage capacity for Li/Na, high rate capability and cycling stability of 2D holey nanosheet samples can be ascribed to the two-dimensional interconnected porous framework that provides large active surface areas, bicontinuous $Li^+/Na^+$ and electron pathways and excellent structural stability inherited from the graphene oxide. To further understand the structural stability of 2D holey nanosheets, structural evolution during the lithiation process is carried out by in-situ TEM imaging on ZMO nanosheet, as a model material. The first-cycle lithiation process of 2D holey ZMO nanosheets was examined, as shown in **Figure 6.14**. As discussed before, ZMO was fully reduced by Li into Zn and Mn metallic nanoparticles which were dispersed in a lithia ($Li_2O$) matrix,

with the $Li_2O$ + nanoparticles being surrounded by a solid electrolyte interface[33]. These results can be further identified by selected-area electron diffraction (SAED) of the fresh and lithiated samples, as shown in **Figure 6.15**. The SAED of fresh samples can be indexed to the spinel ZMO structures in agreement with the XRD analysis. This result is different from that of the lithiated samples, which can be indexed to the Zn and Mn metallic phases (Figure 6.15B). It should be noted that the in-situ TEM characterizations during the first lithiation process proved the structural uniqueness and inherently strong mechanical stability of the 2D holey ZMO nanosheets. During the first lithiation (Figure 6.14A-F), 2D holey ZMO nanosheets maintained the holey morphology in different lithiation stages/ times, for example, 3 mins, 9 mins, 12 mins and 15 mins. After fully lithiation, the overall shape of the starting material can be preserved in 2D geometry, and the overall morphology remains as holey/porous structures because the disintegrated metallic nanoparticles would be dispersed in a lithia ($Li_2O$) matrix. The lithiated ZMO nanosheets remained its overall morphology and porous nature when the ZMO nanosheet was under press during in-situ stress tests, as shown in Figure 6.14G-I. These results were consistent with the aforementioned improved electrochemical characteristics for Li/Na ion storage. The 2D holey MTMO nanosheets can maintain the holey framework and accommodate volume change during charging/discharging, thus improving the cycling stability and coulombic efficiency.

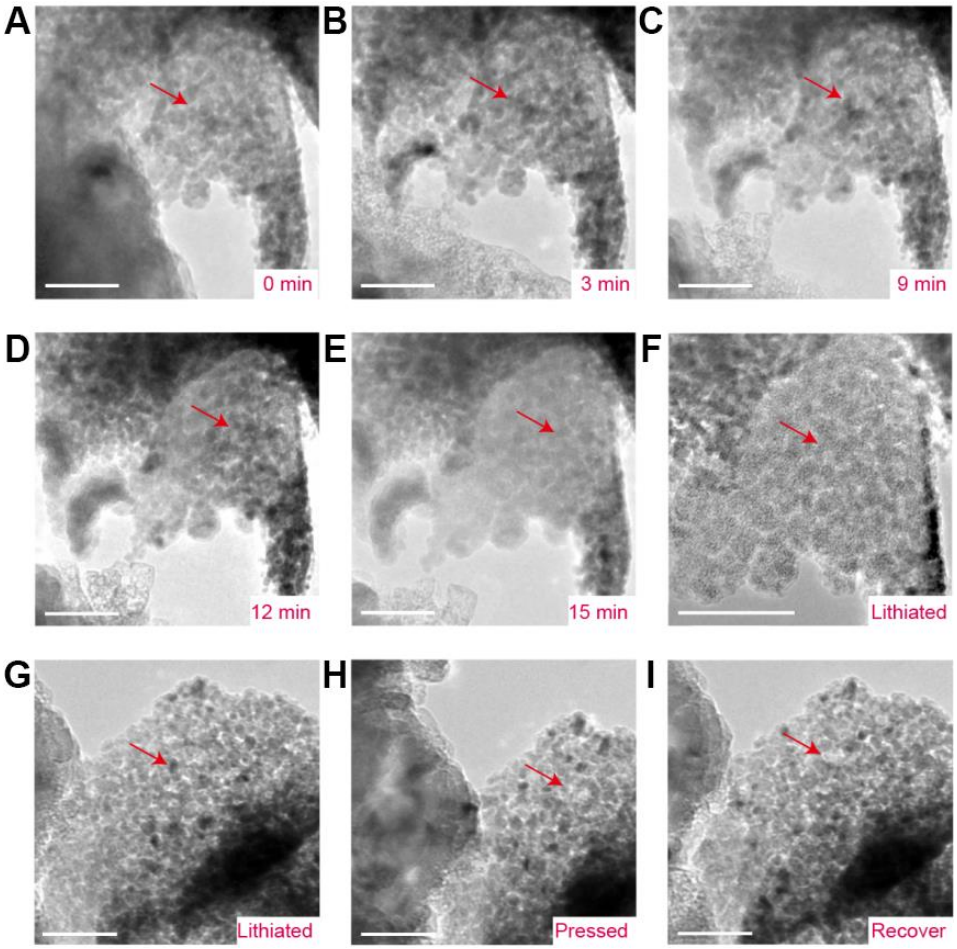


**Figure 6.14. In-situ TEM studies of 2D holey ZMO nanosheets as anodes.** (A-F) TEM images of the 2D holey nanosheets at different lithiation stages/times. (G-I) TEM images of the 2D holey nanosheets under press states. Scale bar, 100 nm. Red arrow points out the holey structures of the 2D ZMO nanosheets.

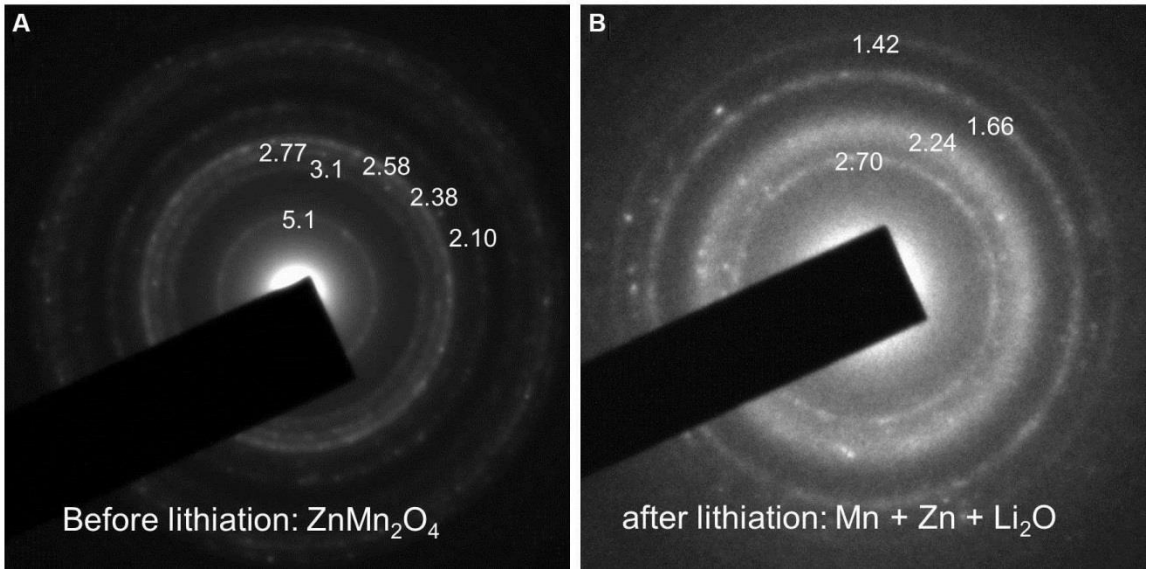


**Figure 6.15. Selected area electron diffraction pattern of the ZMO nanosheets before and after lithiation.** (A) Fresh ZMO nanosheets; (B) ZMO nanosheets after lithiation.

### *6.3.2.4 Operando XAS studies on 2D holey MTMO nanosheets*

As the spinel structure of MTMO is not recovered after the first cycle, operando XAS was further applied as a powerful method to provide detailed information about the oxidation states and the local environment changes of atoms on a short-range scale. The XAS scans of the Zn K-edges and Mn K-edge and their corresponding 1st derivative curves during the charge/discharge processes are shown in **Figure 6.16**. The edge position of the XAS spectra is related to the oxidation state. Initially, the edge energy of the Zn K edge was 9,664 eV, which was a little higher than that of $Zn^{2+}$, indicating that the oxidation state of Zn was a little higher than 2+ (peak A in the 1st derivative plot was at a higher energy than ZnO standard) (Figure 6.16A and B). This is probably due to the formation of the intermediate NaCl-type structure in which the $Zn^{2+}$ has tetrahedral coordination.[159, 160] During formation of the intermediate NaCl-type structure, the intensity of the 1s→4p transition increases for the Zn K-edge. For the discharge

process, the intensity of this spectral feature progressively decreases, which can be explained by the loss of p character of the 1s→4p transition as a consequence of the formation of metallic Zn nanoparticles, which occupied the 4p orbital. Metallic Zn nanoparticles further formed the ZnLi alloy with Li after further discharge (Figure 6.16C). This fact was identified by the peak position, which showed lower energy than Zn foil, as shown in 1st derivative curves. The oxidation state of Mn before the first discharge cycle close to 3+ (peak C in the 1st derivative plot at a similar position as Mn in $Mn_2O_3$). As the Mn K-edge and its 1st derivative curves shown in Figure 6.16D and E, the Mn K-edge shows a continuous shift to lower edge energy, i.e., the electrons are transferred to $Mn^{3+}$ during the first discharge cycle. During the first discharge, the intensity of the pre-edge peak increased and the peak C became weak. The pre-edge peak is associated with transition to empty Mn 3d states. The single pre-edge peak indicates that the Mn is still 3+, but due to the change of the spinel phase, the 1s→3d transition increased. During the charge process, pre-edge structure changed to double-peaked structure, which indicated the transition of $Mn^{3+}$ to $Mn^{2+}$.

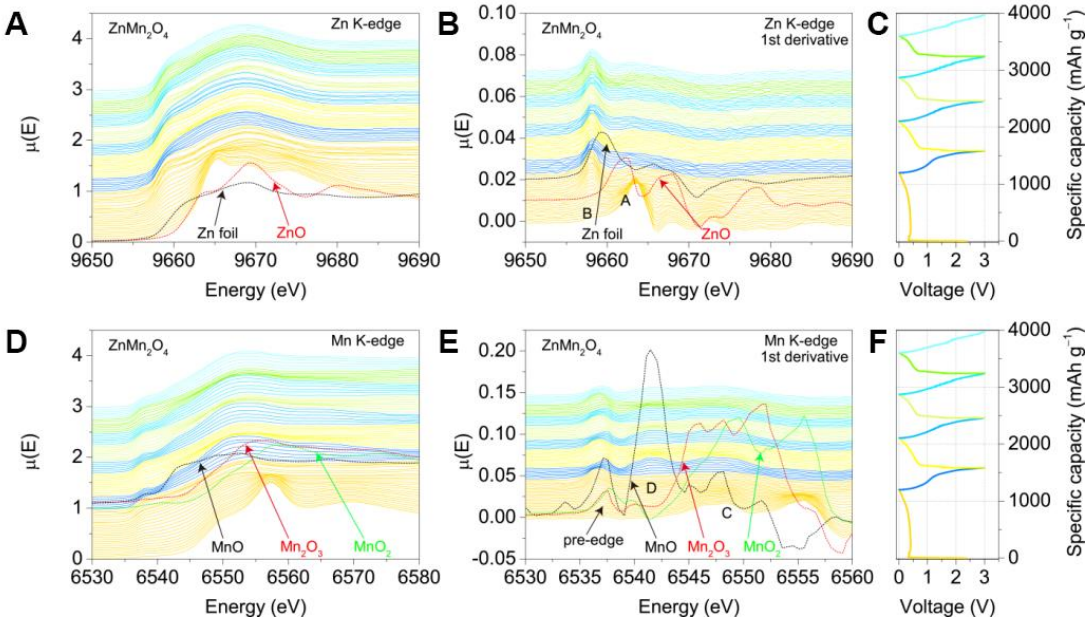


**Figure 6.16. Operando XAS studies on 2D holey MTMO nanosheet.** (A-B) Scan at the Zn K-edge and the corresponding 1st derivative curves during the charge/discharge process. (C) The charge/discharge curves of the 2D holey ZMO nanosheets at 50 mA $g^{-1}$. (D-E) Scan at the Mn K-edge and the corresponding 1st derivative curves during the charge/discharge process. (F) The charge/discharge curves of the 2D holey ZMO nanosheets at 50 mA $g^{-1}$.

These results are consistent with the Operando XRD results shown in **Figure 6.17**. After the first discharge cycle, the oxidation state of Zn slightly increased during charge and decreased during discharge process, indicating the cycling process between ZnLi alloy and metallic Zn nanoparticles. Simultaneously, the oxidation states of Mn change from +3 to +2 in the charge process and go back to +3 at the end of the discharge process, as identified by the reversible shifting of the pre-edge peak positions. The operando XAS studies proved the good chemical stability of the 2D holey ZMO nanosheets during charge/discharge process, showing no unwanted impurities and minimal side reactions occurred in the charge/discharge process.

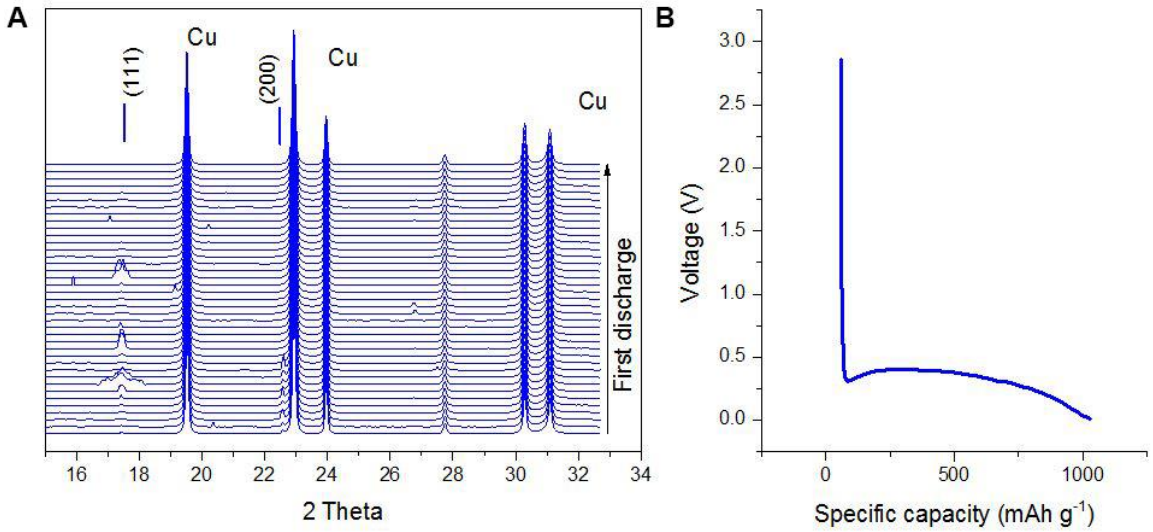


**Figure 6.17. Operando XRD studies of 2D holey $ZnMn_2O_4$ nanosheets during the first discharge process.** (A) XRD patterns of ZMO nanosheets during the first discharge process. (B) The discharge curve of the ZMO nanosheets. ZMO nanosheets deliver high capacity for lithium-ion storage via the conversion reaction along with Zn and Mn. A reversible capacity corresponding to 8.3 mol of Li per mole of $ZnMn_2O_4$ is expected, assuming $x \leqslant 0.5$ for Li intercalation into the spinel lattice ($ZnMn_2O_4 + xLi^+ + xe^- \rightarrow Li_x(ZnMn_2O_4)$), crystal structure destruction, followed by metal particle formation, and alloy formation with Zn ($Li_x(ZnMn_2O_4) + (8\text{-}x)Li^+ + (8\text{-}x)e^- \rightarrow Zn + 2Mn + 4Li_2O$; $Zn + Li^+ + e^- \leftrightarrow ZnLi$). These metallic nanoparticles are dispersed in a lithia ($Li_2O$) matrix, with the $Li_2O$ + nanoparticles being surrounded by a solid electrolyte interface. This makes the mixtures amorphous, as identified by the operando XRD tests.

## 6.4 CONCLUSIONS

In this work, a general synthetic strategy is developed by employing graphene oxide as a sacrificial template to prepare various 2D holey TMO nanosheets, including mixed metal oxides $ZnMn_2O_4$, $ZnCo_2O_4$, $NiCo_2O_4$, $CoFe_2O_4$, and simple metal oxides, such as $Fe_2O_3$, $Co_3O_4$, and $Mn_2O_3$. As potential anode materials for both lithium and sodium-ion storage, the as-obtained 2D holey MTMO nanosheets exhibit superior electrochemical properties including high reversible capacity, excellent rate capability, and cycling stability. This work combined in-situ TEM, X-ray diffraction, with in-situ

XAS measurements, and revealed for the first time the mechanical properties and morphology evolution of the 2D holey MTMO nanosheets during electrochemical processes. Operando XRD and XAS results show that holey ZMO nanosheets deliver high capacity due to the formation of ZnLi alloy as well as the reversible transformation between $Mn^{2+}$ and $Mn^{3+}$. In-situ TEM characterizations show that these 2D holey ZMO nanosheets inherit the strong mechanical properties from graphene oxides, maintaining the holey morphology and displaying minimal structural changes during the lithiation/delithiation processes and even under press states. Due to potential merits of 2D nanostructures, tunable porosity and inherently strong mechanical stability, these 2D holey nanosheets could be promising candidates for emerging applications in energy storage and conversion systems and electrocatalysis. The proposed general strategy would open up a promising avenue for designing 2D nanostructures for versatile materials, especially those with intrinsically non-layered structures, for broad applications in nanoscience and nanotechnology.

# Chapter 7: Summary

This dissertation focused on the rational synthesis and structural engineering of 2D inorganic nanomaterials for electrochemical energy storage. As an emerging class of nanoscale materials, 2D nanomaterials show unprecedented physical and chemical properties that differ from their bulk lamellar systems, which can be attributed to their confined thinness within a nanoscale range versus a lateral dimension up to tens of micrometers and quantum confinement of electrons in 2D plane. Charge transport and storage property is considered as one of the most critical when 2D nanomaterials are applied as electrodes for electrochemical energy storage devices. The goals of this dissertation were to explore the material chemistry of 2D nanomaterials and their charge transport and storage properties for electrochemical energy storage. Several persistent problems and limitations of 2D nanomaterials for energy storage have been identified. This dissertation also presented several promising strategies through structural engineering of the 2D nanomaterials to address these limitations and to improve significantly the power density, energy density and cycle life of state-of-the-art sodium-ion batteries. The following achievements developed in this dissertation will be of great value to the research of 2D nanomaterials for electrochemical energy storage.

- *Rational synthesis of 2D nanomaterials:* 2D nanomaterials were mainly synthesized through mechanically and chemically exfoliating the intrinsically layered structures. In this dissertation, ultrathin $MnO_2$ and $VOPO_4$ nanosheets were synthesized through the liquid-phase exfoliation of the bulk lamellar compounds. 2D nanomaterials can also be obtained via the confined growth under specific surfactant. 2D $LiFePO_4$ nanosheets were obtained in a solvothermal

method by using DEG as solvents and surfactants. A general synthesis of 2D holey transition metal oxide nanosheets was also presented.

- *Exploration of various 2D nanomaterials for energy storage applications:* 2D nanomaterials have found promising applications in electrochemical energy storage, such as supercapacitors, lithium-ion, and sodium-ion batteries. In this dissertation, ultrathin $MnO_2$ nanosheets and $VOPO_4$ nanosheets exhibited high electrochemical performance for supercapacitor. 2D $LiFePO_4$ nanosheets showed much improved rate capability and cycling stability in lithium-ion battery applications. Ultrathin $VOPO_4$ nanosheets showed good electrochemical activity for lithium-ion and sodium-ion storage. The charge transport and storage mechanism and properties were studied.
- *Structural engineering of 2D nanomaterials for efficient energy storage:* The irreversible restacking of 2D nanosheets during materials processing or device fabrication may lead to the decrease of active surfaces for ion storage and the sluggish ion transport. To address this issue, two promising strategies through structural engineering of 2D nanomaterials were presented. One strategy is interlayer engineering of $VOPO_4$ nanosheets via organic molecules intercalation. The other strategy is porosity engineering of 2D transition metal oxide nanosheets. The engineered 2D nanomaterials exhibited much improved and more efficient energy storage properties.

## Reference


1. X. Lu, M. Yu, G. Wang, Y. Tong and Y. Li, *Energy Environ. Sci.*, 2014, **7**, 2160-2181.

2. X. Wang, X. Lu, B. Liu, D. Chen, Y. Tong and G. Shen, *Adv. Mater.*, 2014, **26**, 4763-4782.

3. A. Manthiram, *J. Phys. Chem. L*, 2011, **2**, 176-184.

4. C.-X. Zu and H. Li, *Energy Environ. Sci.*, 2011, **4**, 2614-2624.

5. F. Risacher and B. Fritz, *Aquat. Geochem.*, 2009, **15**, 123-157.

6. S.-W. Kim, D.-H. Seo, X. Ma, G. Ceder and K. Kang, *Adv. Energy Mater.*, 2012, **2**, 710-721.

7. V. Palomares, P. Serras, I. Villaluenga, K. B. Hueso, J. Carretero-Gonzalez and T. Rojo, *Energy Environ. Sci.*, 2012, **5**, 5884-5901.

8. B. L. Ellis and L. F. Nazar, *Curr. Opin. Solid State Mater. Sci.*, 2012, **16**, 168-177.

9. K. Kubota and S. Komaba, *J. Electrochem. Soc.*, 2015, **162**, A2538-A2550.

10. R. Ma and T. Sasaki, *Adv. Mater.*, 2010, **22**, 5082-5104.

11. C. Tan and H. Zhang, *Chem. Soc. Rev.*, 2015, **44**, 2713-2731.

12. D. Yang, Z. Lu, X. Rui, X. Huang, H. Li, J. Zhu, W. Zhang, Y. M. Lam, H. H. Hng, H. Zhang and Q. Yan, *Angew. Chem. Int. Ed.*, 2014, **53**, 9352-9355.

13. M. R. Lukatskaya, O. Mashtalir, C. E. Ren, Y. Dall'Agnese, P. Rozier, P. L. Taberna, M. Naguib, P. Simon, M. W. Barsoum and Y. Gogotsi, *Science*, 2013, **341**, 1502.

14. L. Peng, Y. Zhu, D. Chen, R. S. Ruoff and G. Yu, *Adv. Energy Mater.*, 2016, **6**, DOI: 10.1002/aenm.201600025.

15. Y. Tang, Y. Zhang, W. Li, B. Ma and X. Chen, *Chem. Soc. Rev.*, 2015, **44**, 5926-5940.

16. C. H. Sun, X. H. Yang, J. S. Chen, Z. Li, X. W. Lou, C. Li, S. C. Smith, G. Q. Lu and H. G. Yang, *Chem. Commun.*, 2010, **46**, 6129-6131.

17. J. N. Coleman, M. Lotya, A. O'Neill, S. D. Bergin, P. J. King, U. Khan, K. Young, A. Gaucher, S. De, R. J. Smith, I. V. Shvets, S. K. Arora, G. Stanton, H.-Y. Kim, K. Lee, G. T. Kim, G. S. Duesberg, T. Hallam, J. J. Boland, J. J. Wang, J. F. Donegan, J. C. Grunlan, G. Moriarty, A. Shmeliov, R. J. Nicholls, J. M. Perkins, E. M. Grieveson, K. Theuwissen, D. W. McComb, P. D. Nellist and V. Nicolosi, *Science*, 2011, **331**, 568.

18. V. Nicolosi, M. Chhowalla, M. G. Kanatzidis, M. S. Strano and J. N. Coleman, *Science*, 2013, **340**, 1226419.

19. Z. Sun, T. Liao, Y. Dou, S. M. Hwang, M.-S. Park, L. Jiang, J. H. Kim and S. X. Dou, *Nat. Commun.*, 2014, **5**, 3813.

20. X. Chen, Y. Zhou, Q. Liu, Z. Li, J. Liu and Z. Zou, *ACS Appl. Mater. Interfaces*, 2012, **4**, 3372-3377.

21. J. Zhu, L. Bai, Y. Sun, X. Zhang, Q. Li, B. Cao, W. Yan and Y. Xie, *Nanoscale*, 2013, **5**, 5241-5246.

22. J. H. Lee, N. Park, B. G. Kim, D. S. Jung, K. Im, J. Hur and J. W. Choi, *ACS Nano*, 2013, **7**, 9366-9374.

23. J. Ding, H. Wang, Z. Li, A. Kohandehghan, K. Cui, Z. Xu, B. Zahiri, X. Tan, E. M. Lotfabad, B. C. Olsen and D. Mitlin, *ACS Nano*, 2013, **7**, 11004-11015.

24. Y. Xu, Z. Lin, X. Zhong, X. Huang, N. O. Weiss, Y. Huang and X. Duan, *Nat. Commun.*, 2014, **5**, 4554.

25. N. Jung, S. Kwon, D. Lee, D.-M. Yoon, Y. M. Park, A. Benayad, J.-Y. Choi and J. S. Park, *Adv. Mater.*, 2013, **25**, 6854-6858.

26. M. Li, Z. Tang, M. Leng and J. Xue, *Adv. Funct. Mater.*, 2014, **24**, 7495-7502.

27. S.-H. Lee, V. Sridhar, J.-H. Jung, K. Karthikeyan, Y.-S. Lee, R. Mukherjee, N. Koratkar and I.-K. Oh, *ACS Nano*, 2013, **7**, 4242-4251.

28. L. Cong, H. Xie and J. Li, *Adv. Energy Mater.*, 2017, DOI: 10.1002/aenm.201601906.

29. M. F. El-Kady, V. Strong, S. Dubin and R. B. Kaner, *Science*, 2012, **335**, 1326.

30. V. L. Pushparaj, M. M. Shaijumon, A. Kumar, S. Murugesan, L. Ci, R. Vajtai, R. J. Linhardt, O. Nalamasu and P. M. Ajayan, *Proc. Natl. Acad. Sci. U.S.A.*, 2007, **104**, 13574-13577.

31. H. Nishide and K. Oyaizu, *Science*, 2008, **319**, 737.

32. X. Jia, Z. Chen, A. Suwarnasarn, L. Rice, X. Wang, H. Sohn, Q. Zhang, B. M. Wu, F. Wei and Y. Lu, *Energy Environ. Sci.*, 2012, **5**, 6845-6849.

33. G. Eda, G. Fanchini and M. Chhowalla, *Nat. Nanotechnol.*, 2008, **3**, 270-274.

34. D. Pech, M. Brunet, H. Durou, P. Huang, V. Mochalin, Y. Gogotsi, P.-L. Taberna and P. Simon, *Nat. Nanotechnol.*, 2010, **5**, 651-654.

35. J. Bae, M. K. Song, Y. J. Park, J. M. Kim, M. Liu and Z. L. Wang, *Angew. Chem. Int. Ed.*, 2011, **50**, 1683-1687.

36. X. Lang, A. Hirata, T. Fujita and M. Chen, *Nat. Nanotechnol.*, 2011, **6**, 232-236.

37. J. Liu, J. Jiang, C. Cheng, H. Li, J. Zhang, H. Gong and H. J. Fan, *Adv. Mater.*, 2011, **23**, 2076-2081.

38. X. Wang, B. Liu, Q. Wang, W. Song, X. Hou, D. Chen, Y.-b. Cheng and G. Shen, *Adv. Mater.*, 2013, **25**, 1479-1486.

39. T. Brezesinski, J. Wang, S. H. Tolbert and B. Dunn, *Nat. Mater.*, 2010, **9**, 146-151.

40. H. Wang, H. S. Casalongue, Y. Liang and H. Dai, *J. Am. Chem. Soc.*, 2010, **132**, 7472-7477.

41. J. J. Yoo, K. Balakrishnan, J. Huang, V. Meunier, B. G. Sumpter, A. Srivastava, M. Conway, A. L. Mohana Reddy, J. Yu, R. Vajtai and P. M. Ajayan, *Nano Lett.*, 2011, **11**, 1423-1427.

42. J. Feng, X. Sun, C. Wu, L. Peng, C. Lin, S. Hu, J. Yang and Y. Xie, *J. Am. Chem. Soc.*, 2011, **133**, 17832-17838.

43. J. Xie, X. Sun, N. Zhang, K. Xu, M. Zhou and Y. Xie, *Nano Energy*, 2013, **2**, 65-74.

44. C. Wu and Y. Xie, *Energy Environ. Sci.*, 2010, **3**, 1191-1206.

45. B. M. Azmi, T. Ishihara, H. Nishiguchi and Y. Takita, *J. Power Sources*, 2003, **119–121**, 273-277.

46. N.-G. Park, K. M. Kim and S. H. Chang, *Electrochem. Commun.*, 2001, **3**, 553-556.

47. J.-Y. Luo, W.-J. Cui, P. He and Y.-Y. Xia, *Nat. Chem.*, 2010, **2**, 760-765.

48. Z. Fan, J. Yan, T. Wei, L. Zhi, G. Ning, T. Li and F. Wei, *Adv. Funct. Mater.*, 2011, **21**, 2366-2375.

49. D. C. Marcano, D. V. Kosynkin, J. M. Berlin, A. Sinitskii, Z. Sun, A. Slesarev, L. B. Alemany, W. Lu and J. M. Tour, *ACS Nano*, 2010, **4**, 4806-4814.

50. Y. Omomo, T. Sasaki, Wang and M. Watanabe, *J. Am. Chem. Soc.*, 2003, **125**, 3568-3575.

51. N. Yamamoto, N. Hiyoshi and T. Okuhara, *Chem. Mater.*, 2002, **14**, 3882-3888.

52. G. Yu, X. Xie, L. Pan, Z. Bao and Y. Cui, *Nano Energy*, 2013, **2**, 213-234.

53. O. Markovitch and N. Agmon, *J. Phys. Chem. A*, 2007, **111**, 2253-2256.

54. B. Yan, L. Liao, Y. You, X. Xu, Z. Zheng, Z. Shen, J. Ma, L. Tong and T. Yu, *Adv. Mater.*, 2009, **21**, 2436-2440.

55. L. Beneš, K. Melánová, M. Trchová, P. Čapková and P. Matějka, *Eur. J. Inorg. Chem.*, 1999, **1999**, 2289-2294.

56. Z. Yan, Z. Peng, Z. Sun, J. Yao, Y. Zhu, Z. Liu, P. M. Ajayan and J. M. Tour, *ACS Nano*, 2011, **5**, 8187-8192.

57. Y. Zhu, S. Murali, W. Cai, X. Li, J. W. Suk, J. R. Potts and R. S. Ruoff, *Adv. Mater.*, 2010, **22**, 3906-3924.

58. M. D. Stoller, S. Park, Y. Zhu, J. An and R. S. Ruoff, *Nano Lett.*, 2008, **8**, 3498-3502.

59. C. Liu, Z. Yu, D. Neff, A. Zhamu and B. Z. Jang, *Nano Lett.*, 2010, **10**, 4863-4868.

60. C.-Y. Chen, C.-Y. Fan, M.-T. Lee and J.-K. Chang, *J. Mater. Chem.*, 2012, **22**, 7697-7700.

61. J. Yan, Z. Fan, T. Wei, W. Qian, M. Zhang and F. Wei, *Carbon*, 2010, **48**, 3825-3833.

62. M. D. Stoller and R. S. Ruoff, *Energy Environ. Sci.*, 2010, **3**, 1294-1301.

63. G. Wang, X. Lu, Y. Ling, T. Zhai, H. Wang, Y. Tong and Y. Li, *ACS Nano*, 2012, **6**, 10296-10302.

64. L.-Q. Mai, F. Yang, Y.-L. Zhao, X. Xu, L. Xu and Y.-Z. Luo, *Nat. Commun.*, 2011, **2**, 381.

65. Z.-S. Wu, W. Ren, D.-W. Wang, F. Li, B. Liu and H.-M. Cheng, *ACS Nano*, 2010, **4**, 5835-5842.

66. L. Peng, X. Peng, B. Liu, C. Wu, Y. Xie and G. Yu, *Nano Lett.*, 2013, **13**, 2151-2157.

67. Q. Lu, M. W. Lattanzi, Y. Chen, X. Kou, W. Li, X. Fan, K. M. Unruh, J. G. Chen and J. Q. Xiao, *Angew. Chem. Int. Ed.*, 2011, **50**, 6847-6850.

68. N. Dupré, J. Gaubicher, T. Le Mercier, G. Wallez, J. Angenault and M. Quarton, *Solid State Ionics*, 2001, **140**, 209-221.

69. V. Augustyn, J. Come, M. A. Lowe, J. W. Kim, P.-L. Taberna, S. H. Tolbert, H. D. Abruña, P. Simon and B. Dunn, *Nat. Mater.*, 2013, **12**, 518-522.

70. J. Wang, J. Polleux, J. Lim and B. Dunn, *J. Phys. Chem. C*, 2007, **111**, 14925-14931.

71. V. Augustyn, E. R. White, J. Ko, G. Gruner, B. C. Regan and B. Dunn, *Mater. Horiz.*, 2014, **1**, 219-223.

72. K. Saravanan, H. S. Lee, M. Kuezma, J. J. Vittal and P. Balaya, *J. Mater. Chem.*, 2011, **21**, 10042-10050.

73 B. C. Melot and J. M. Tarascon, *Acc. Chem. Res.*, 2013, **46**, 1226-1238.

74. A. K. Padhi, K. S. Nanjundaswamy and J. B. Goodenough, *J. Electrochem. Soc.*, 1997, **144**, 1188-1194.

75. G. He, W. H. Kan and A. Manthiram, *Chem. Mater.*, 2016, **28**, 682-688.

76. N. Dupré, J. Gaubicher, J. Angenault and M. Quarton, *J. Solid State Electrochem.*, 2004, **8**, 322-329.

77. J. M. Tarascon and M. Armand, *Nature*, 2001, **414**, 359-367.

78. P. S. Herle, B. Ellis, N. Coombs and L. F. Nazar, *Nat. Mater.*, 2004, **3**, 147-152.

79. J. Wang and X. Sun, *Energy Environ. Sci.*, 2012, **5**, 5163-5185.

80. D. Lepage, C. Michot, G. Liang, M. Gauthier and S. B. Schougaard, *Angew. Chem. Int. Ed.*, 2011, **50**, 6884-6887.

81. Y. Wang, Y. Wang, E. Hosono, K. Wang and H. Zhou, *Angew. Chem. Int. Ed.*, 2008, **47**, 7461-7465.

82. R. Malik, A. Abdellahi and G. Ceder, *J. Electrochem. Soc.*, 2013, **160**, A3179-A3197.

83. L. Wang, F. Zhou, Y. S. Meng and G. Ceder, *Phys. Rev. B*, 2007, **76**, 165435.

84. K. Saravanan, P. Balaya, M. V. Reddy, B. V. R. Chowdari and J. J. Vittal, *Energy Environ. Sci.*, 2010, **3**, 457-463.

85. C. Nan, J. Lu, C. Chen, Q. Peng and Y. Li, *J. Mater. Chem.*, 2011, **21**, 9994-9996.

86. X. Qin, J. Wang, J. Xie, F. Li, L. Wen and X. Wang, *Phys. Chem. Chem. Phys.*, 2012, **14**, 2669-2677.

87. X. Qin, X. Wang, H. Xiang, J. Xie, J. Li and Y. Zhou, *J. Phys. Chem. C*, 2010, **114**, 16806-16812.

88. P. P. Prosini, M. Lisi, D. Zane and M. Pasquali, *Solid State Ionics*, 2002, **148**, 45-51.

89. P. Gibot, M. Casas-Cabanas, L. Laffont, S. Levasseur, P. Carlach, S. Hamelet, J.-M. Tarascon and C. Masquelier, *Nat. Mater.*, 2008, **7**, 741-747.

90. N. Meethong, Y.-H. Kao, M. Tang, H.-Y. Huang, W. C. Carter and Y.-M. Chiang, *Chem. Mater.*, 2008, **20**, 6189-6198.

91. O. García-Moreno, M. Alvarez-Vega, J. García-Jaca, J. M. Gallardo-Amores, M. L. Sanjuán and U. Amador, *Chem. Mater.*, 2001, **13**, 1570-1576.

92. Y. Bai, Y. Yin, J. Yang, C. Qing and W. Zhang, *J. Raman Spectrosc.*, 2011, **42**, 831-838.

93. C. M. Burba and R. Frech, *J. Electrochem. Soc.*, 2004, **151**, A1032-A1038.

94. J. Chen, S. Wang and M. S. Whittingham, *J. Power Sources*, 2007, **174**, 442-448.

95. H. Pizzala, S. Caldarelli, J.-G. Eon, A. M. Rossi, D. Laurencin and M. E. Smith, *J. Am. Chem. Soc.*, 2009, **131**, 5145-5152.

96. G. Eda, H. Yamaguchi, D. Voiry, T. Fujita, M. Chen and M. Chhowalla, *Nano Lett.*, 2011, **11**, 5111-5116.

97. C. Wu, X. Lu, L. Peng, K. Xu, X. Peng, J. Huang, G. Yu and Y. Xie, *Nat. Commun.*, 2013, **4**, 2431.

98. L. Beneš, K. Melánová, V. Zima, J. Kalousová and J. Votinský, *Inorg. Chem.*, 1997, **36**, 2850-2854.

99. J.-M. Atebamba, J. Moskon, S. Pejovnik and M. Gaberscek, *J. Electrochem. Soc.*, 2010, **157**, A1218-A1228.

100. J. Maier, *Nat. Mater.*, 2005, **4**, 805-815.

101. M. Winter and R. J. Brodd, *Chem. Rev.*, 2004, **104**, 4245-4270.

102. H. Yang, X.-L. Wu, M.-H. Cao and Y.-G. Guo, *J. Phys. Chem. C*, 2009, **113**, 3345-3351.

103. W.-J. Zhang, *J. Electrochem. Soc.*, 2010, **157**, A1040-A1046.

104. J. Lim, D. Kim, V. Mathew, D. Ahn, J. Kang, S.-W. Kang and J. Kim, *J. Alloys Compd.*, 2011, **509**, 8130-8135.

105. N. Li, Z. Chen, W. Ren, F. Li and H.-M. Cheng, *Proc. Natl. Acad. Sci. U.S.A.*, 2012, **109**, 17360-17365.

106. J. Hassoun, F. Bonaccorso, M. Agostini, M. Angelucci, M. G. Betti, R. Cingolani, M. Gemmi, C. Mariani, S. Panero, V. Pellegrini and B. Scrosati, *Nano Lett.*, 2014, **14**, 4901-4906.

107. Y. Wang, Y. Wang, D. Jia, Z. Peng, Y. Xia and G. Zheng, *Nano Lett.*, 2014, **14**, 1080-1084.

108. J. Ni, W. Liu, J. Liu, L. Gao and J. Chen, *Electrochem. Commun.*, 2013, **35**, 1-4.

109. R. Berthelot, D. Carlier and C. Delmas, *Nat. Mater.*, 2011, **10**, 74-80.

110. S. P. Ong, V. L. Chevrier, G. Hautier, A. Jain, C. Moore, S. Kim, X. Ma and G. Ceder, *Energy Environ. Sci.*, 2011, **4**, 3680-3688.

111. D. Kundu, E. Talaie, V. Duffort and L. F. Nazar, *Angew. Chem. Int. Ed.*, 2015, **54**, 3431-3448.

112. N. Yabuuchi, K. Kubota, M. Dahbi and S. Komaba, *Chem. Rev.*, 2014, **114**, 11636-11682.

113. W. Luo, F. Shen, C. Bommier, H. Zhu, X. Ji and L. Hu, *Acc. Chem. Res.*, 2016, **49**, 231-240.

114. J. B. Goodenough and Y. Kim, *Chem. Mater.*, 2010, **22**, 587-603.

115. H. Kim, H. Kim, Z. Ding, M. H. Lee, K. Lim, G. Yoon and K. Kang, *Adv. Energy Mater.*, 2016, **6**, DOI: 10.1002/ aenm.201600943.

116. D. Larcher and J. M. Tarascon, *Nat. Chem.*, 2015, **7**, 19-29.

117. F. Bonaccorso, L. Colombo, G. Yu, M. Stoller, V. Tozzini, A. C. Ferrari, R. S. Ruoff and V. Pellegrini, *Science*, 2015, **347**.

118. H. Wang, H. Yuan, S. Sae Hong, Y. Li and Y. Cui, *Chem. Soc. Rev.*, 2015, **44**, 2664-2680.

119. Z. Chen, Q. Chen, H. Wang, R. Zhang, H. Zhou, L. Chen and M. S. Whittingham, *Electrochem. Commun.*, 2014, **46**, 67-70.

120. Y. Zhu, L. Peng, D. Chen and G. Yu, *Nano Lett.*, 2016, **16**, 742-747.

121. J. W. Johnson, A. J. Jacobson, J. F. Brody and S. M. Rich, *Inorg. Chem.*, 1982, **21**, 3820-3825.

122. A. P. Cohn, K. Share, R. Carter, L. Oakes and C. L. Pint, *Nano Lett.*, 2016, **16**, 543-548.

123. Y. Li, Y. Liang, F. C. Robles Hernandez, H. Deog Yoo, Q. An and Y. Yao, *Nano Energy*, 2015, **15**, 453-461.

124. Y. Liang, H. D. Yoo, Y. Li, J. Shuai, H. A. Calderon, F. C. Robles Hernandez, L. C. Grabow and Y. Yao, *Nano Lett.*, 2015, **15**, 2194-2202.

125. L. Beneš, K. Melánová, J. Svoboda and V. Zima, *J. Incl. Phenom. Macrocycl. Chem.*, 2012, **73**, 33-53.

126. M. Morris, A. Dyer and R. W. McCabe, *J. Mater. Chem.*, 1995, **5**, 1427-1431.

127. R. Gautier, R. Gautier, O. Hernandez, N. Audebrand, T. Bataille, C. Roiland, E. Elkaim, L. Le Polles, E. Furet and E. Le Fur, *Dalton Trans.*, 2013, **42**, 8124-8131.

128. G. Kresse, *J. Non-Cryst. Solids*, 1995, **192**, 222-229.

129. G. Henkelman and H. Jónsson, *J. Chem. Phys.*, 2000, **113**, 9978-9985.

130. X. Huang, C. Tan, Z. Yin and H. Zhang, *Adv. Mater.*, 2014, **26**, 2185-2204.

131. B. Anasori, Y. Xie, M. Beidaghi, J. Lu, B. C. Hosler, L. Hultman, P. R. C. Kent, Y. Gogotsi and M. W. Barsoum, *ACS Nano*, 2015, **9**, 9507-9516.

132. K. S. Novoselov, D. Jiang, F. Schedin, T. J. Booth, V. V. Khotkevich, S. V. Morozov and A. K. Geim, *Proc. Natl. Acad. Sci. U.S.A.*, 2005, **102**, 10451-10453.

133. M. Chhowalla, H. S. Shin, G. Eda, L.-J. Li, K. P. Loh and H. Zhang, *Nat. Chem.*, 2013, **5**, 263-275.

134. Q. H. Wang, K. Kalantar-Zadeh, A. Kis, J. N. Coleman and M. S. Strano, *Nat. Nanotechnol.*, 2012, **7**, 699-712.

135. C. Yuan, H. B. Wu, Y. Xie and X. W. Lou, *Angew. Chem. Int. Ed.*, 2014, **53**, 1488-1504.

136. Y. Liang, H. Wang, J. Zhou, Y. Li, J. Wang, T. Regier and H. Dai, *J. Am. Chem. Soc.*, 2012, **134**, 3517-3523.

137. F. Cheng, J. Shen, B. Peng, Y. Pan, Z. Tao and J. Chen, *Nat. Chem.*, 2011, **3**, 79-84.

138. Q. Song and Z. J. Zhang, *J. Am. Chem. Soc.*, 2012, **134**, 10182-10190.

139. L. Huang, D. Chen, Y. Ding, S. Feng, Z. L. Wang and M. Liu, *Nano Lett.*, 2013, **13**, 3135-3139.

140. L. Hu, H. Zhong, X. Zheng, Y. Huang, P. Zhang and Q. Chen, *Sci. Rep.*, 2012, **2**, 986.

141. Y. Zhu, C. Cao, J. Zhang and X. Xu, *J. Mater. Chem. A*, 2015, **3**, 9556-9564.

142. J. N. Coleman, M. Lotya, A. O'Neill, S. D. Bergin, P. J. King, U. Khan, K. Young, A. Gaucher, S. De, R. J. Smith, I. V. Shvets, S. K. Arora, G. Stanton, H.-Y. Kim, K. Lee, G. T. Kim, G. S. Duesberg, T. Hallam, J. J. Boland, J. J. Wang, J. F. Donegan, J. C. Grunlan, G. Moriarty, A. Shmeliov, R. J. Nicholls, J. M. Perkins, E. M. Grieveson, K. Theuwissen, D. W. McComb, P. D. Nellist and V. Nicolosi, *Science*, 2011, **331**, 568-571.

143. K.-G. Zhou, N.-N. Mao, H.-X. Wang, Y. Peng and H.-L. Zhang, *Angew. Chem. Int. Ed.*, 2011, **50**, 10839-10842.

144. J. Liu and X.-W. Liu, *Adv. Mater.*, 2012, **24**, 4097-4111.

145. Y.-Y. Hu, Z. Liu, K.-W. Nam, O. J. Borkiewicz, J. Cheng, X. Hua, M. T. Dunstan, X. Yu, K. M. Wiaderek, L.-S. Du, K. W. Chapman, P. J. Chupas, X.-Q. Yang and C. P. Grey, *Nat. Mater.*, 2013, **12**, 1130-1136.

146. S.-H. Yu, S. H. Lee, D. J. Lee, Y.-E. Sung and T. Hyeon, *Small*, 2016, **12**, 2146-2172.

147. P. Poizot, S. Laruelle, S. Grugeon, L. Dupont and J. M. Tarascon, *Nature*, 2000, **407**, 496-499.

148. M. V. Reddy, G. V. Subba Rao and B. V. R. Chowdari, *Chem. Rev.*, 2013, **113**, 5364-5457.

149. Y. Zhong, M. Yang, X. Zhou and Z. Zhou, *Mater. Horiz.*, 2015, **2**, 553-566.

150. C. Nethravathi and M. Rajamathi, *Carbon*, 2008, **46**, 1994-1998.

151. Y. Liang, Y. Li, H. Wang, J. Zhou, J. Wang, T. Regier and H. Dai, *Nat. Mater.*, 2011, **10**, 780-786.

152. H. Wang, L.-F. Cui, Y. Yang, H. Sanchez Casalongue, J. T. Robinson, Y. Liang, Y. Cui and H. Dai, *J. Am. Chem. Soc.*, 2010, **132**, 13978-13980.

153. C. Largeot, C. Portet, J. Chmiola, P.-L. Taberna, Y. Gogotsi and P. Simon, *J. Am. Chem. Soc.*, 2008, **130**, 2730-2731.

154. Y. Ren, A. R. Armstrong, F. Jiao and P. G. Bruce, *J. Am. Chem. Soc.*, 2010, **132**, 996-1004.

155. S. Laruelle, S. Grugeon, P. Poizot, M. Dollé, L. Dupont and J.-M. Tarascon, *J. Electrochem. Soc.*, 2002, **149**, A627-A634.

156. Y. Fang, Y. Lv, R. Che, H. Wu, X. Zhang, D. Gu, G. Zheng and D. Zhao, *J. Am. Chem. Soc.*, 2013, **135**, 1524-1530.

157. B. Guo, X. Yu, X.-G. Sun, M. Chi, Z.-A. Qiao, J. Liu, Y.-S. Hu, X.-Q. Yang, J. B. Goodenough and S. Dai, *Energy Environ. Sci.*, 2014, **7**, 2220-2226.

158. R. Alcántara, M. Jaraba, P. Lavela and J. L. Tirado, *Chem. Mater.*, 2002, **14**, 2847-2848.

159. S. Permien, S. Indris, U. Schürmann, L. Kienle, S. Zander, S. Doyle and W. Bensch, *Chem. Mater.*, 2016, **28**, 434-444.

160. S. Permien, S. Indris, A.-L. Hansen, M. Scheuermann, D. Zahn, U. Schürmann, G. Neubüser, L. Kienle, E. Yegudin and W. Bensch, *ACS Appl. Mater. Interfaces*, 2016, **8**, 15320-15332.

# Vita

Lele Peng was born in Jiangxi Province, China. He received his B.S. degree in Materials Science and Engineering from University of Science and Technology of China (USTC) in 2012. After graduation, he worked as the research assistant in Prof. Changzheng Wu and Prof. Yi Xie's group at USTC for one year, focusing on the research of physical and chemical properties of 2D nanomaterials. He then joined Prof. Guihua Yu's group at the University of Texas at Austin in 2013. His research interest at UT Austin includes rational synthesis and structural engineering of 2D nanomaterials for next-generation energy storage devices, especially for high-energy lithium/sodium-ion batteries and supercapacitors

Address: llpeng@utexas.edu

This dissertation was typed by the author.